

Cinvestav

CENTRO DE INVESTIGACIÓN Y DE ESTUDIOS  
AVANZADOS DEL IPN

---

# **Towards New Physics Through Precision Measurements in $B_S^0$ and $\tau$ Decays**

In partial fulfillment of the requirements for the degree of  
Doctor of Science in Physics

Presented by

**Michel Enrique Hernández Villanueva**

Advisors

Dr. Eduard de la Cruz Burelo

Dr. Gabriel López Castro

January, 2019



*A mis padres,  
Ricardo y Marina,  
a quienes debo todo lo que he logrado.*

*A Iris,  
mi mejor amiga y mi esposa.  
Gracias por tu apoyo, amor.*





# Agradecimientos

A mi esposa, Iris Herrera, por su amistad, su paciencia y su amor. Gracias por todo tu apoyo.

A mis padres, Ricardo y Marina. A mis hermanos, Alan y Vanessa. A mi familia, cuyo amor y consejos me han impulsado a seguir adelante y a quienes debo lo que soy.

A mis directores de tesis, Dr. Gabriel López Castro y Dr. Eduard de la Cruz Burelo, por su paciencia al compartir sus conocimientos conmigo, por todo el apoyo que recibí de su parte y por poner su confianza en mí al permitirme ser parte de este proyecto. Mis más sinceros agradecimientos.

A mis sinodales, Dr. Pablo Roig, Dr. Iván Heredia, Dr. David Bermúdez y Dr. Genaro Toledo, por las enriquecedoras charlas durante mi formación académica y por las muy valiosas sugerencias que contribuyeron a mejorar este trabajo.

A los profesores, al personal de apoyo y a toda la comunidad del Cinvestav, cuya labor y dedicación me permitieron concluir satisfactoriamente con esta etapa de mi vida.

To the DØ collaboration. Particularly, to Marjorie Corcoran, Brad Abbott, and Jesus Orduna, for the fruitful collaboration in the measurement of the  $B_s^0$  lifetime.

To the Belle II collaboration. In particular, the doctors Ikuo Ueda, Takanori Hara, Hideki Miyake (KEK), Kiyoshi Hayasaka (Niigata U.) and Armine Rostomyan (DESY), for all your support and the enriching conversations sharing your knowledge with me.

A mis compañeros, colegas y amigos Luis Flores, Jorge Romero, Daniela Magos, Enrique Macías, Jorge Venzor, Gabriel Ramírez, Héctor Villegas y Pamela González, con quienes compartí la gratificante experiencia de cursar el doctorado y cuya amistad fue imprescindible para concluirla.

A mis grandes amigos Jair Trejo, Victor Villeda, Rodolfo Alanís, José Luis Quiroz, Alejandro y Martín Jiménez, Carlos Ridaura, Emiliano Sánchez, Adrián Martínez, Jorge Serrano y Gabriel Barrón. Por su invaluable amistad durante todos estos años y su apoyo incondicional.

Y por último, pero no por ello menos importante, al pueblo de México por el apoyo económico recibido a través del CONACYT durante mis estudios de posgrado (proyectos FOINS 296, CV 236394) y sin el cual este trabajo no hubiera podido realizarse.

# Resumen

A pesar de describir con éxito la interacción de partículas elementales, existe evidencia de que el Modelo Estándar de partículas elementales (SM) es una teoría incompleta. La existencia de nuevas partículas o interacciones que formen parte de una teoría más completa puede manifestarse en los experimentos como desviaciones a las predicciones del SM o bien mediante la observación de procesos prohibidos en el mismo. De particular interés son los mesones  $B_s$  y leptones  $\tau$  producidos en los experimentos DØ y Belle II, respectivamente, en donde la luminosidad proporciona estadística suficiente para realizar mediciones de precisión de parámetros del SM, así como búsquedas de nueva física.

En este trabajo se presenta la medición del tiempo de vida de la componente pesada del mesón  $B_s^0$  a través del decaimiento  $B_s^0 \rightarrow J/\psi f_0(980)$ , utilizando datos acumulados por el experimento DØ durante el Run II de Tevatron, obteniendo  $\tau(B_s^0) = 1.70 \pm 0.14 \text{ (stat)} \pm 0.05 \text{ (syst) ps}$ . Esta medición está directamente relacionada con la determinación de uno de los parámetros involucrados en la mezcla del sistema  $B_s^0 - \bar{B}_s^0$  y a la búsqueda de mecanismos de violación de CP más allá del SM. Adicionalmente, se presenta el programa de física del leptón  $\tau$  en el experimento Belle II, así como el estudio de sensibilidad para este experimento de dos canales de decaimiento con un mesón  $\eta$  involucrado: (i)  $\tau^- \rightarrow \eta \pi^- \pi^0 \nu_\tau$ , el cual en el límite de simetría de isospín SU(2) es un chequeo de consistencia con la sección eficaz de dispersión  $\sigma(e^+e^- \rightarrow \eta \pi^+ \pi^-)$  para regiones de baja energía; (ii)  $\tau^- \rightarrow \eta \pi^- \nu_\tau$ , proceso que nunca ha sido observado y, dada su supresión por G-paridad, permite la búsqueda de corrientes escalares y tensoriales de nueva física, imponiendo límites en los acoplamientos no estándar de las mismas. Se muestran estimaciones de 1 a 20  $\text{ab}^{-1}$ , que corresponden a la luminosidad integrada que se espera durante los primeros años del experimento Belle II.



# Abstract

Despite the correct and consistent description of the elementary particle interactions, there is evidence that the Standard Model (SM) is an incomplete theory. Solving the issues faced by the SM requires the introduction of new interactions and, if such interactions exist, they can be observed as deviations in the SM predictions or forbidden processes. Particularly of interest for this work are the  $B_s^0$  mesons and  $\tau$  leptons produced in the DØ and Belle II experiments, respectively, where the luminosity provides the statistics for high precision SM measurements and searches for new physics.

In this work, the lifetime measurement of the  $B_s^0$  meson in the decay channel  $B_s^0 \rightarrow J/\psi f_0(980)$  is reported, which is a CP-odd final state. Using  $10.4 \text{ fb}^{-1}$  of data collected with the DØ detector in Run II of the Tevatron, the lifetime of the CP-odd component of the  $B_s^0$  meson is measured to be  $\tau(B_s^0) = 1.70 \pm 0.14 \text{ (stat)} \pm 0.05 \text{ (syst) ps}$ . This measurement is closely related to the  $B_s^0 - \bar{B}_s^0$  mixing and searches for new CP violation mechanisms. Additionally, the  $\tau$  lepton physics program of Belle II is reviewed and two sensitivity studies are shown: (i)  $\tau^- \rightarrow \eta \pi^- \pi^0 \nu_\tau$ , which in the isospin symmetry limit SU(2) is a cross-check of consistency with the cross section  $\sigma(e^+e^- \rightarrow \eta \pi^+ \pi^-)$  at low energies; (ii)  $\tau^- \rightarrow \eta \pi^- \nu_\tau$ , which has never been observed and, given the suppression by G-parity, it allows the searches of scalar and tensor interactions. Estimations from 1 to  $20 \text{ ab}^{-1}$  are shown, corresponding to the integrated luminosity expected during the first years of operation of Belle II.



---

# Contents

<b>1</b>	<b>Introduction</b>	<b>1</b>
1.1	The Standard Model of Elementary Particles . . . . .	1
1.2	Beyond Standard Model Interactions . . . . .	3
1.3	Flavor Physics . . . . .	5
1.4	Scope of This Work . . . . .	7
<b>2</b>	<b><math>B_s^0</math> Lifetime Measurement at the DØ Experiment</b>	<b>9</b>
2.1	The $B_s^0$ Mixing Process and CP Eigenstates . . . . .	9
2.2	The $B_s^0$ CP Eigenstates . . . . .	11
2.3	The CP-odd Decay Channel $B_s^0 \rightarrow J/\psi f_0(980)$ . . . . .	11
2.4	The DØ Detector . . . . .	12
2.5	$B_s^0$ Lifetime Measurement in the $J/\psi f_0(980)$ State . . . . .	12
<b>3</b>	<b>Tau Lepton Physics</b>	<b>23</b>
3.1	$\tau$ Lepton Mass . . . . .	23
3.2	$\tau$ Lepton Lifetime . . . . .	25
3.3	Branching Ratios of $\tau$ Decays . . . . .	26
3.4	Semileptonic $\tau$ Decays . . . . .	30
3.5	Standard Model tests in $\tau$ decays . . . . .	31
<b>4</b>	<b>The Belle II Experiment</b>	<b>35</b>
4.1	Integrated Luminosity at SuperKEKB . . . . .	36

4.2	The Belle II Detector . . . . .	37
4.3	Software Framework: Basf2 . . . . .	43
4.4	Detector Commissioning Phases . . . . .	48
<b>5</b>	<b>Prospects for <math>\tau</math> Lepton Physics at Belle II</b>	<b>51</b>
5.1	$\tau^+\tau^-$ Production at Belle II . . . . .	51
5.2	$\tau$ Lepton Mass Measurement . . . . .	56
5.3	Prospects for $\tau$ Lepton Physics . . . . .	58
<b>6</b>	<b>Sensitivity Study of <math>\tau \rightarrow \eta\pi\pi^0\nu_\tau</math> Decays</b>	<b>63</b>
6.1	$\tau$ Decays and CVC . . . . .	64
6.2	The Process $e^+e^- \rightarrow \eta\pi^+\pi^-$ and its Relation to $\tau$ Decays . . . . .	65
6.3	Sensitivity Study at Belle II . . . . .	67
6.4	Concluding Remarks . . . . .	72
<b>7</b>	<b><math>\tau^- \rightarrow \eta\pi^-\nu_\tau</math>: Phenomenological Analysis and Sensitivity Study</b>	<b>75</b>
7.1	The Decay $\tau^- \rightarrow \eta\pi\nu_\tau$ and Second Class Currents . . . . .	76
7.2	Effective-field Theory Study of $\tau^- \rightarrow \eta\pi^-\nu_\tau$ . . . . .	78
7.3	Sensitivity study of $\tau^- \rightarrow \eta\pi^-\nu_\tau$ decays . . . . .	88
7.4	Concluding Remarks . . . . .	93
<b>8</b>	<b>Conclusions and Perspectives</b>	<b>97</b>
<b>A</b>	<b>Systematic Uncertainties in the <math>B_s^0</math> Lifetime Measurement</b>	<b>103</b>
A.1	$f_0(980)$ Mass Window . . . . .	103
A.2	Fit Bias . . . . .	106
A.3	Distribution Models . . . . .	106
<b>B</b>	<b>Reconstruction and selection of <math>\tau^- \rightarrow \eta\pi^-\pi^0\nu_\tau</math> decays</b>	<b>109</b>
B.1	Basf2 analysis steering file . . . . .	109



---

B.2	Kinematic distributions and selection cuts . . . . .	111
<b>C</b>	<b><math>\tau^- \rightarrow \eta \pi^- \nu_\tau</math> reconstruction, BDT training and optimization</b>	<b>117</b>
C.1	Generation . . . . .	117
C.2	Reconstruction . . . . .	119
C.3	Boosted Decision Trees . . . . .	119
<b>D</b>	<b>Publications, Conference Proceedings and Internal Notes</b>	<b>125</b>
	<b>References</b>	<b>127</b>



# Chapter 1

---

## Introduction

The Standard Model (SM) of elementary particle interactions is a very successful quantum field theory, consistent with all the measurements of the elementary particles, their properties and their interactions [1, 2, 3]. There are a few anomalies observed so far in experiments and compelling evidence of new phenomena that indicate that the SM is not the ultimate theory of fundamental interactions. In order to have evidence of new interactions or particles that can solve the problems faced by the SM, new experimental findings are necessary to elucidate the nature of the new theory. In this thesis, we propose the study of some reactions involving heavy flavors,  $B_s$  mesons and  $\tau$  leptons, which can shed light on the nature of the New Physics. Our study is tightly linked to the data that has been (and will be) obtained in experiments at the high-intensity frontier.

### 1.1 The Standard Model of Elementary Particles

The Standard Model of elementary particles is the name given to the local gauge quantum field theory that describes three of the four known fundamental interactions between elementary particles [4]. The strong force arises from a gauge theory based on an unbroken  $SU(3)$  symmetry and the electromagnetic and weak interactions come from a partly broken  $SU(2) \times U(1)$  symmetry. Gravity is not included in the model. There are three fermion gener-

ations, consisting of six quarks and six leptons. Four electroweak gauge bosons, eight gluons and one scalar boson, the Higgs boson [5, 6, 7, 8], which gives mass to the charged fermions and the weak gauge bosons (See Fig. 1.1). As a simplifying assumption, neutrinos remains massless in the SM.

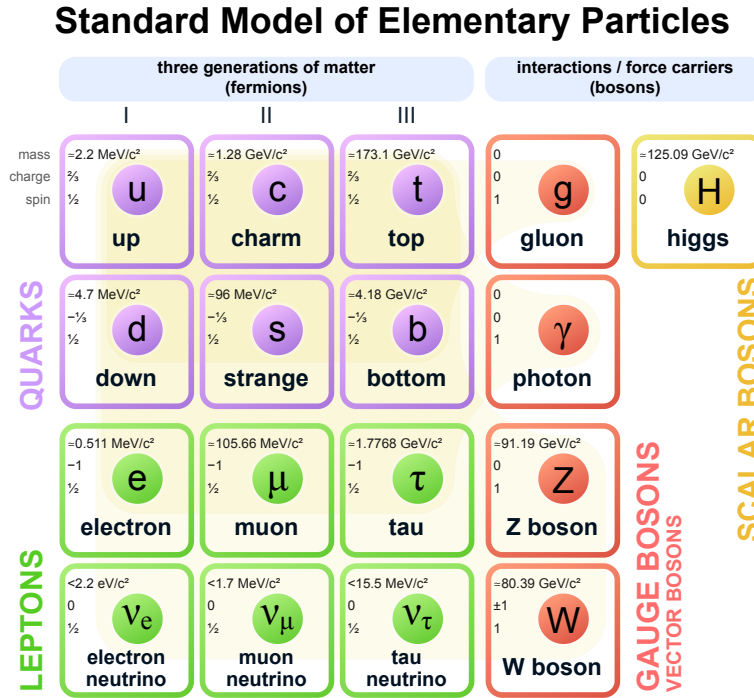


Figure 1.1: The Standard Model of particle physics [12]. It contains 12 fundamental fermions, four electroweak gauge bosons, eight gluons and the Higgs boson.

There are two important bases in the Lagrangian of the SM: a mass basis, where the mass terms are diagonal, and the interaction basis, where the  $W^\pm$  interactions are diagonal. Flavor-changing interactions come from the fact that, in the quark sector, these two bases are not the same. The CKM matrix [9, 10] is the rotation that relates these two bases.

As any causal local Lorentz invariant quantum field theory conserves CPT, the SM does. However, the discrete symmetries C and P are “maximally violated”, in the sense that P

changes the chirality of fermion fields,  $C$  exchanges particle and antiparticle, and the left-handed and right-handed fermion fields have different gauge representations in the SM. CP can be violated but it depends on a physical phase in the Lagrangian. The only place in the SM where a complex phase can be physical, therefore CP is violated, is in the Yukawa sector via the phase contained in the CKM and PMNS matrices [10, 11].

The SM is predictive and testable because there are multiple measurements that depend on the same few parameters. Since almost half-century ago many experiments have confirmed its predictions, comparing the values of the parameters obtained by different measurements, and none has been capable to contradict them.

## 1.2 Beyond Standard Model Interactions

Despite its correct and consistent description of the elementary particle phenomena, there is evidence that the Standard Model is an incomplete theory. Many questions remain unanswered. As a few examples:

- **Neutrino masses.** In the SM, neutrinos are massless particles. However, neutrino oscillations show that neutrinos must have mass [11, 13, 14]. It is not clear which is the mechanism that provides mass to neutrinos.
- **Dark matter and dark energy.** From cosmological observations, it is estimated the SM can explain only  $\sim 5\%$  of the energy contained in the universe. Around 26% should be dark matter and the remaining 69% dark energy [15].
- **Matter-antimatter asymmetry.** Matter and antimatter should have been produced in equal amounts when the Universe was born. CP violation mechanism in the SM is not enough to explain why the universe is made mostly of matter [16, 17].
- **Lepton universality violation.** Several measurements performed in the recent years hint at a possible violation of Lepton Universality [18]. Discrepancies, mainly in  $B$

meson decays [19, 20], respect to the SM predictions would be a clear sign that non-SM virtual particles are contributing in the processes.

- **Anomalous magnetic moment of the muon.** Present SM evaluations of the anomalous magnetic moment of the muon  $a_\mu = (g_\mu - 2)/2$  lie between 2.7 and  $\sim 4$  standard deviations below the experimental result [21].
- **Hierarchy problem.** The mass-squared parameter for the Higgs boson receives quadratically divergent corrections at the quantum level, hence it is very sensitive to ultraviolet physics. In order to have naturally a Higgs mass of  $\sim 125 \text{ GeV}/c^2$ , new physics which couples to the Higgs sector should appear to cut off the quadratically divergent contributions [22].

These anomalies should be studied further to conclude if they require to introduce physics beyond the Standard Model (BSM). It could be introduced as new interactions, particles and/or symmetries. If such kind of SM extensions exist, their effects can be observed mainly in two ways. The first one is the direct production of new particles in the energy frontier colliders, such as the LHC. The second one is the measurement of observables with high precision, in which the effects of new physics should appear as a deviation in the SM predictions or via the observation of forbidden/very suppressed decay channels. Experiments targeting the luminosity frontier provide the proper environment for the second kind of searches.

Motivated by the problems that the SM face, several BSM extensions have been developed. In particular and related with the motivations in this thesis, the two Higgs doublet models and the leptoquarks model are briefly described.

### 1.2.1 Two Higgs doublet models

The observation of a neutral Higgs boson opens the possibility of extended Higgs sectors. One of the simplest extensions are the two Higgs doublet models (2HDM), which introduce one additional electroweak doublet [23]. They aim to provide a mechanism for addressing

issues such as dark matter, the generation of a baryon asymmetry, the gauge hierarchy problem, and the strong CP problem [24]. In general, this kind of extensions has as a signature the existence of a charged scalar state  $H^\pm$ .

### 1.2.2 Leptoquarks

Leptoquarks are hypothetical particles emerging in SM extensions of matter unification that simultaneously couple to a quark and a lepton [25, 26]. In local quantum field theories they can be of either scalar (spin-zero) or vector (spin-one) nature. They can provide an explanation for lepton universality violation and the observed  $B$ -physics anomalies [27, 28, 29], and also a new source of CP violation [30]. The discovery of Leptoquarks would be a tentative signal of matter unification.

Currently, constraints on Leptoquark interactions with matter are derived mostly from precision observables such as electric and magnetic dipole moments of charged leptons, neutral mesons mixing,  $B$  and  $D$  meson decays and lepton number violating decays [31].

## 1.3 Flavor Physics

The flavor physics sector is the part of the Standard Model which arises from the interplay of quarks and leptons with weak currents, and its aim is the search of processes where SM predictions are: (i) clean enough that effects from physics BSM could be recognized if they exist; or (ii) suppressed or forbidden, in that case, any enhancement of such process is a clear signal of physics BSM. Predictions at the quark level are clean since leading-order weak effects are well understood. However, in the experiments what is observed are hadrons, not quarks. It is important to identify processes where the hadronic physics effects, hard to estimate, are well known or under good control.

In the SM, the only source of flavor changing interaction at tree level is the charged currents mediated by the  $W^\pm$  bosons. There is no fundamental reason why there cannot be flavor

changing neutral currents (FCNCs). Yet, experimentally what is observed is that FCNCs are highly suppressed, which is a manifestation that they appear in the SM predominantly at higher orders in perturbation theory. The SM is consistent with the experimental observations in the sense that all neutral current interactions are flavor conserving at tree level and FCNCs are mediated only at the loop level, therefore they are suppressed. BSM theories usually produce an enhancement of the branching ratio of FCNC processes.

Another source of suppression in the SM is symmetries, which may prevent (exact symmetries) or suppress (approximate symmetries) the occurrence of some processes or properties. As example of the later is the  $SU(2)$  isospin symmetry. Since the masses of the light quarks  $m_u$  and  $m_d$  are different and small compared with  $\Lambda_{QCD}$  ( $\sim 200$  MeV), isospin is an approximate good symmetry in the interaction of hadrons and turns out to be useful in the study of flavor physics in the quark sector. SM has also “accidental” symmetries, as a consequence of global gauge invariant symmetries. Examples of such symmetries are baryon and lepton number conservation.

In this thesis work, we use some particular properties of heavy flavor systems and their decays that are sensitive to the effects of new interactions. Through the measurements of a particular  $B_s$  meson decay that follows its time evolution properties at the DØ experiment, we can determine the lifetime of one of its mass states, which is an useful parameter to investigate other sources of CP violation and contributions of BSM particles in the  $B_s$  mixing process. On the other hand,  $\tau$  leptons provide a clean laboratory to study the hadronization properties of the weak currents in the 1-2 GeV regime and, in particular, to study the sensitivity of the several decay channels to the effects of new interactions such as a charged Higgs or leptoquarks. This study is convenient given the data that will be provided in the future by the heavy flavor factories like SuperKEKB and the LHC collider.



## 1.4 Scope of This Work

The work developed in this thesis studies a  $B_s^0$  meson decay and three  $\tau$  lepton decays. The first one analyzed in the DØ experiment, which finished operations in 2011, and the  $\tau$  decays studied as sensitivity analyses in the Belle II experiment, which will start its full physics program by the first months of 2019.

In chapter 2, the lifetime of a CP-odd decay channel of the  $B_s^0$  meson,  $B_s^0 \rightarrow J/\psi f_0(980)$ , is measured in the experiment DØ. It is shown that this lifetime measurement can be translated into a measurement of the width  $\Gamma_H$  of the heavy mass eigenstate of  $B_s^0$ , which is one of the parameters describing the mixing process in the  $B_s^0$ - $\bar{B}_s^0$  system [32]. In the chapter it is also discussed that the difference between light and heavy decay rates are sensitive to new physics effects, particularly to contributions of BSM particles in the mixing process.

Chapter 3 reviews some topics of  $\tau$  lepton physics, useful for the development of the next chapters. A description of the techniques and results for measurements of  $\tau$  lepton properties is provided, such as the mass, the lifetime, and the branching ratio of allowed decays. A general description of semileptonic  $\tau$  decays and the resonance structures involved are also presented.

Chapter 4 is dedicated to the description of the Belle II experiment, which is coupled to the SuperKEKB accelerator, a B-factory of second generation designed to collide electrons and positrons at high luminosity. Belle II provides an ideal environment for the study of hadronic  $\tau$  decays, as discussed in chapter 5 [33]. Using the early data provided by the Belle II detector, a first measurement of the  $\tau$  lepton mass is reported, testing the performance of the Belle II subsystems and tools [34]. In the near future, taking advantage of the large amount of  $\tau$  lepton pairs produced a Belle II, a high-precision  $\tau$  mass measurement will reduce the uncertainty in  $m_\tau$  [35], which is a fundamental parameter in tests of lepton universality.

In chapter 6, a review of the decay  $\tau^- \rightarrow \eta \pi^- \pi^0 \nu_\tau$  is performed. In the limit of SU(2) isospin symmetry, it exists a close relationship between the distributions of these  $\tau$  hadronic decay and the cross section of the process  $e^+e^- \rightarrow \eta \pi^+ \pi^-$  via the CVC hypothesis [36].

The relevance of testing the CVC hypothesis resides in the hadronic contribution to the SM estimation for the muon anomalous magnetic moment, which uncertainty can be reduced using  $\tau$  decays and CVC.

Chapter 7 discusses the phenomenology of the decay  $\tau^- \rightarrow \eta \pi^- \nu_\tau$ , a process that has never been observed and is heavily suppressed in the SM by G-parity violation. This characteristic makes it an excellent candidate in the search for non-standard scalar and tensor interactions. In particular, the contribution of a charged Higgs or leptoquarks may enhance the branching ratio of the decay [37, 38, 39]. A sensitivity study for their detection is also performed at the Belle II experiment.

# Chapter 2

---

## $B_s^0$ Lifetime Measurement at the DØ Experiment

One of the cleanest areas for flavor studies is the  $b$  decay physics, because the mass of the  $b$ -quark is large enough to control the impact of hadronization effects [40]. That explains why  $B$ -physics is a central topic in the program of the most recent experiments [41, 33]. The  $B_d$  and  $B_s$  meson systems provide sensitive probes of the CP violation structure of the SM. While CP violation has been studied extensively in the  $B^0$  system, less information exists for the  $B_s^0$  system. In this work, the  $B_s^0$  mixing is the major focus.

A brief description of the  $B_s$  mixing process and the SM parameters involved are discussed. The flavor, mass and CP eigenstates of the  $B_s$  are introduced, explaining the relationship between them and the importance of measuring the properties of each one. We measure the lifetime of the  $B_s^0$  heavy mass eigenstate through the CP-odd decay channel  $B_s^0 \rightarrow J/\psi f_0(980)$ , using data provided by the DØ experiment during the Run II of Tevatron.

### 2.1 The $B_s^0$ Mixing Process and CP Eigenstates

The  $B_s^0$  (with quark content  $\bar{b}s$ ) and  $\bar{B}_s^0$  (quark content  $b\bar{s}$ ) mesons are produced as flavor eigenstates at colliders. However, neither conservation law prevents  $B_s^0$  and  $\bar{B}_s^0$  from having

transitions (See Fig. 2.1). Therefore, they may oscillate between themselves. In the SM these transitions are suppressed because they are FCNC processes. BSM contributions to mixing could be easily of a similar size as the SM contribution. After the production, the  $B_s^0$  and  $\bar{B}_s^0$  mesons propagate as mass eigenstates

$$|B_L\rangle = p|B_s^0\rangle + q|\bar{B}_s^0\rangle, \quad |B_H\rangle = p|B_s^0\rangle - q|\bar{B}_s^0\rangle, \quad (2.1)$$

being  $p$  and  $q$  complex parameters with the normalization condition  $|p|^2 + |q|^2 = 1$ . The state  $|B_H\rangle$  corresponds to the heavy mass eigenstate and the state  $|B_L\rangle$  to the light one. In the SM, four parameters describe the  $B_q^0 - \bar{B}_q^0$  mixing process: the mass difference  $\Delta m_s$  between the light and heavy mass eigenstates, the width  $\Gamma_H$  and  $\Gamma_L$  of the heavy and light eigenstate, respectively, and the weak mixing angle  $\phi_s$ .

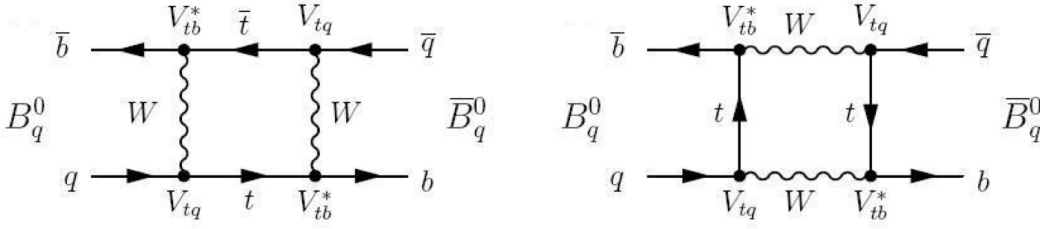


Figure 2.1: Lowest order Feynman diagrams that induce  $B_q^0 - \bar{B}_q^0$  oscillations, where  $q = \{d, s\}$ .

The mass difference of the two mass eigenstates  $\Delta M_s = M_H - M_L$  is given by the off-shell intermediate states of the box diagrams in figure 2.1 [42], thus it is sensitive to heavy internal particles contributions, such as the top quark or the W-boson in the SM, or BSM particles that may contribute. The decay rate difference  $\Delta\Gamma_s = \Gamma_L - \Gamma_H$  is given by on-shell intermediate states, then it is sensitive to light internal particles. In ref. [43] it is shown that new physics effects for  $\Delta\Gamma_s$  can be at most of the order of 30% given other experimental constraints, for this reason a precision measurement of the quantities involved in the  $B_s^0 - \bar{B}_s^0$  mixing, particularly the decay rates  $\Gamma_L$ ,  $\Gamma_H$  and their difference, is fundamental in the search of BSM contributions for the box diagrams.

## 2.2 The $B_s^0$ CP Eigenstates

The CP transformation exchanges the  $B_s^0$  and  $\bar{B}_s^0$  states

$$CP|B_s^0\rangle = e^{i\xi}|\bar{B}_s^0\rangle, \quad CP|\bar{B}_s^0\rangle = e^{-i\xi}|B_s^0\rangle. \quad (2.2)$$

Then, eigenstates of CP can be defined as

$$|B_{\pm}\rangle = \frac{1}{\sqrt{2}}(|B_s^0\rangle \pm e^{i\xi}|\bar{B}_s^0\rangle), \quad (2.3)$$

where  $|B_+\rangle$  and  $|B_-\rangle$  are the even and odd eigenstates, respectively. If CP violation is neglected in mixing, it can be shown that  $q/p = \pm e^{i\xi}$ , giving

$$CP|B_H\rangle = -|B_H\rangle, \quad CP|B_L\rangle = |B_L\rangle. \quad (2.4)$$

That is, the mass eigenstates are also eigenstates of CP [32]. The heavy mass eigenstate coincides with the odd eigenstate of CP, and the light mass eigenstate corresponds to the even eigenstate of CP.

In consequence, a measurement of the  $B_s^0$  lifetime in a pure CP eigenstate gives information about the lifetime of the heavy or light mass eigenstates, which are important parameters to improve the understanding of the mixing process in the  $B_s^0$  system.

## 2.3 The CP-odd Decay Channel $B_s^0 \rightarrow J/\psi f_0(980)$

The  $B_s^0 \rightarrow J/\psi f_0(980)$  channel is a pure CP-odd eigenstate decay. Indeed, the  $B_s^0$  is a spin 0 state with negative parity, the resonance  $f_0(980)$  has  $J^{PC} = 0^{++}$  and the  $J/\psi$  has  $J^{PC} = 1^{--}$ . For this reason, this channel is a very good alternative to the well known golden channel  $B_s^0 \rightarrow J/\psi \phi$  to study the  $B_s^0$  mixing, because the last one requires an angular analysis to obtain the CP-even and CP-odd contributions of the eigenstates [44]. The  $B_s^0 \rightarrow J/\psi f_0(980)$  decay was first discussed in [45] and it has been observed by the LHCb, Belle, CDF, and DØ collaborations [46, 47, 48, 49]. Due to its CP-odd nature, in the absence of CP violation

in mixing, the final state can be produced only by the decay of the  $B_s^0$  heavy mass eigenstate, and the measurement of the  $B_s^0 \rightarrow J/\psi f_0(980)$  lifetime can be translated into a measurement of  $\Gamma_H$ . In 2011, the CDF collaboration reported a first measurement of the lifetime [48], obtaining  $c\tau = (510 \pm 36 \pm 9) \mu\text{m}$ . After that, the LHCb and CMS collaborations reported a lifetime of  $c\tau = (510 \pm 12 \pm 8) \mu\text{m}$  and  $c\tau = (502 \pm 10.2 \pm 3.4) \mu\text{m}$ , respectively [50, 51].

## 2.4 The DØ Detector

The DØ experiment is a multi-purpose detector, with a typical layered design (See Fig. 2.2). The DØ detector is one of the two large particle physics experiments at Fermilab's Tevatron collider. The DØ collaboration began in 1983 and involved hundreds of scientists from 77 institutions. The experiment was upgraded from 1996 to 2001 and ran until the Tevatron ceased operations in 2011.

The most relevant components of the DØ detector to this analysis are the central tracking and the muon systems. Pre-shower detectors, electromagnetic and hadronic calorimeters surround the tracker. The muon system is located outside the calorimeters, and consists of multilayer drift chambers and scintillation counters inside 1.8 T iron toroidal magnets, and two similar layers outside the toroids. The DØ detector is described in detail in Ref. [52].

## 2.5 $B_s^0$ Lifetime Measurement in the $J/\psi f_0(980)$ State

The lifetime of the  $B_s^0$  meson is measured in the decay channel  $B_s^0 \rightarrow J/\psi \pi^+ \pi^-$  with  $|M_{\pi^+ \pi^-} - 980| < 100 \text{ MeV}/c^2$ , which is mainly CP-odd and dominated by the  $f_0(980)$  resonance. The  $J/\psi$  is reconstructed in the  $\mu^+ \mu^-$  decay mode. The data used in this analysis were collected with the DØ detector during the Run II of the Tevatron Collider at a center-of-mass energy of 1.96 TeV, and correspond to an integrated luminosity of  $10.4 \text{ fb}^{-1}$ .

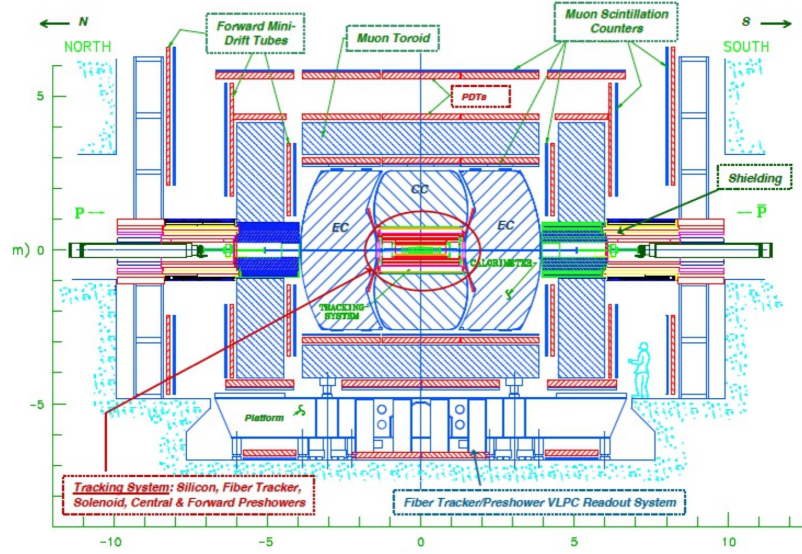


Figure 2.2: Design diagram of the DØ experiment. Pre-shower detectors, electromagnetic and hadronic calorimeters surround the tracking system, and the muon detectors are located outside the calorimeters.

### 2.5.1 Event reconstruction

To reconstruct the  $B_s^0$  candidates, first a reconstruction of  $J/\psi \rightarrow \mu^+\mu^-$  candidates is performed looking for a pair of muon tracks with opposite charge and common vertex. Each  $J/\psi$  candidate must have a transverse momentum greater than  $1.5 \text{ GeV}/c$  and a mass inside the  $2.80 - 3.35 \text{ GeV}/c^2$  window. After that, a search is made for  $\pi^+\pi^-$  tracks forming a common vertex with the  $J/\psi$  candidate. The invariant mass of the two pions is required to be in the region  $880 - 1080 \text{ MeV}/c^2$ , mainly dominated by the  $f_0(980)$  resonance. The  $B_s^0$  candidates are reconstructed by a constrained fit to a common vertex for the four charged tracks, requiring an invariant mass inside the range  $5.1 - 5.8 \text{ GeV}/c^2$  and a  $P_T$  greater than  $6.0 \text{ GeV}/c$ .

Figure 2.3 shows the invariant mass distribution of the  $B_s^0$  candidates after the selection and cuts, in which several background sources are identified.

- Cross-feed contamination: mainly produced by the combination of  $J/\psi$  mesons from

b hadron decays with another particles.

- Combinatorial background: coming from the random combinations of  $J/\psi$  mesons with additional tracks.
- $B^+$  contamination:  $B^+ \rightarrow J/\psi K^+$  decays in which the kaon is misidentified as a pion, and an extra track accidentally forms a vertex with the  $J/\psi K^+$ .

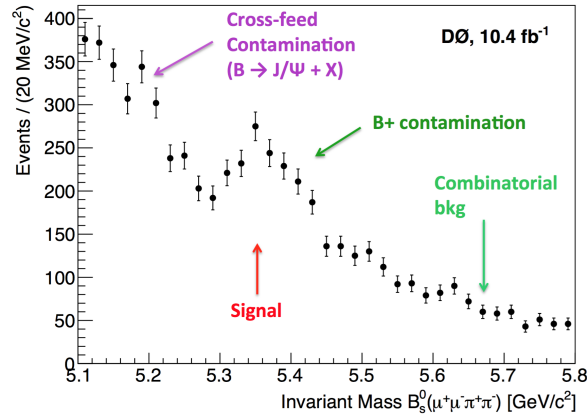


Figure 2.3: Invariant mass distribution of the  $B_s^0$  candidates after the selection and cuts. Several background sources around the  $B_s^0$  peak are identified.

### 2.5.2 Lifetime measurement method

The lifetime measurement is based on the transverse decay length method. The transverse decay length is defined as

$$L_{xy} = \vec{L}_{xy} \cdot \vec{P}_T / P_T, \quad (2.5)$$

where  $\vec{P}_T$  is the transverse momentum vector of the  $B_s^0$ , and  $\vec{L}_{xy}$  is defined as figure 2.4 shows. The proper transverse decay length  $\lambda$  is obtained applying a boost to  $L_{xy}$ . If  $\beta$  is the velocity with respect to  $c$  and  $\gamma$  is the Lorentz factor,

$$\lambda = \frac{L_{xy}}{(\beta\gamma)_T} = L_{xy} \frac{M_B}{P_T}, \quad (2.6)$$



where  $M_B$  is the mass of the  $B_s^0$  taken from the world average reported in the Particle Data Group [35].

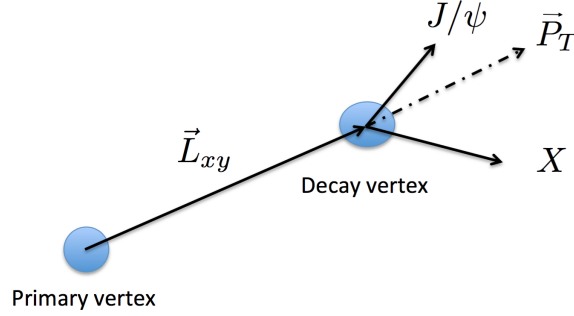


Figure 2.4: The decay vertex is located as the point where the tracks of the final state particles coincide. The vector, transverse to the beam, between the primary vertex (where the candidate is produced) and the decay vertex is labeled as  $\vec{L}_{xy}$ .

To measure the lifetime, a simultaneous unbinned likelihood fit to the mass and proper decay length distributions is performed. The likelihood function  $\mathcal{L}$  is defined by:

$$\mathcal{L} = \prod_{j=1}^N \left[ N_s \mathcal{F}_s^j + N_b \mathcal{F}_b^j + N_p \mathcal{F}_p^j \right], \quad (2.7)$$

where  $N$  is the total number of events and  $N_s$ ,  $N_b$  and  $N_p$  are the expected number of signal, background and misreconstructed  $B^+$  events in the sample, respectively. The last one, due to the kinematics, if the kaon is misidentified as a pion and another pion is added in the search for  $B_s^0 \rightarrow J/\psi \pi^+ \pi^-$  decays, the invariant mass of misreconstructed  $B^\pm \rightarrow J/\psi K^\pm$  decays could be boosted to the region of the real  $B_s^0$  events or even higher.  $\mathcal{F}_s^j$ ,  $\mathcal{F}_b^j$  and  $\mathcal{F}_p^j$  are the product of three probability density functions that model the mass  $m$ , the proper transverse decay length  $\lambda$  and the uncertainty on proper decay length  $\sigma_\lambda$  distributions for the signal, background and misreconstructed  $B^+$  events

$$\mathcal{F}_\alpha^j = M_\alpha(m_j) T_\alpha(\lambda_j) E_\alpha(\sigma_{\lambda_j}); \quad \alpha = \{s, b, p\}, \quad (2.8)$$

where  $m_j$ ,  $\lambda_j$  and  $\sigma_j$  represent the mass,  $\lambda$  and its uncertainty, respectively, for a given decay  $j$ .

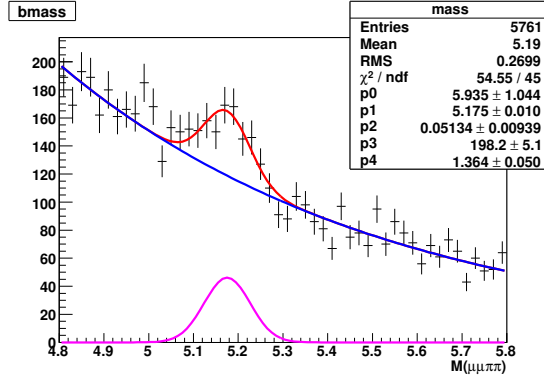


Figure 2.5: Cross-feed background shape from  $B^0 \rightarrow J/\psi + X$  Monte Carlo simulation, fitted with a single gaussian plus exponential.

For the signal, the mass distribution is modeled by a Gaussian function

$$M_s(m_j; \mu, \sigma) = \frac{1}{\sqrt{2\pi}\sigma} e^{-(m_j - \mu)^2 / (2\sigma^2)}, \quad (2.9)$$

where  $\mu$  and  $\sigma$  are the mean and the width of the Gaussian.

The background, divided in combinatorial and cross-feed physics contamination from  $B \rightarrow J/\psi + X$  decays, is:

$$M_b(m_j) = f_b \cdot M_b^{\text{comb}}(m_j) + (1 - f_b) \cdot M_b^{\text{cross-feed}}(m_j), \quad (2.10)$$

where  $f_b$  is a fraction parameter. The physics contamination is mainly produced by the combination of  $J/\psi$  mesons from  $b$  hadron decays with other particles produced in the collision, or from the same  $b$  hadron <sup>1</sup>. Figure 2.5 shows the background shape from  $B^0 \rightarrow J/\psi + X$  Monte Carlo simulation. The cross-feed contamination is described by a Gaussian component

$$M_b^{\text{cross-feed}}(m_j; \mu_b, \sigma_b) = \frac{1}{\sqrt{2\pi}\sigma_b} e^{-(m_j - \mu_b)^2 / (2\sigma_b^2)}, \quad (2.11)$$

<sup>1</sup>Other  $b$  hadron decays with final states such as  $B^0 \rightarrow J/\psi K\pi$ ,  $B^0 \rightarrow J/\psi \pi\pi$  and  $B_s^0 \rightarrow J/\psi KK$  are reconstructed below the signal of the  $B_s^0$ , either due to the lower mass of the  $B^0$  or the missed mass when a kaon is misidentified as a pion.

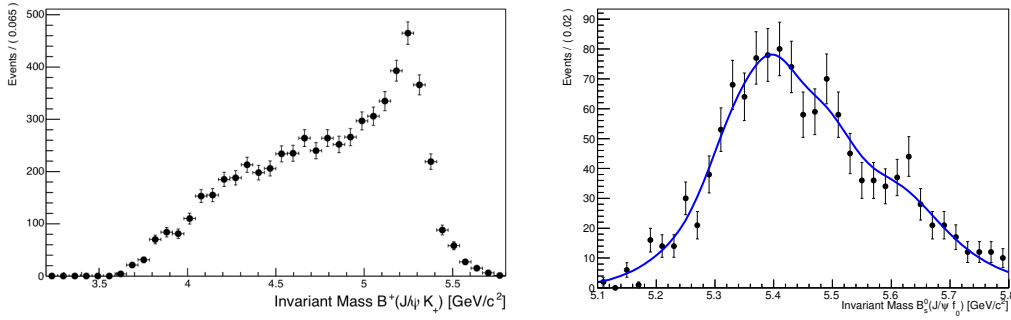


Figure 2.6: Data sample reconstructed as  $B^+ \rightarrow J/\psi K^+$  decays, where a peak related to  $B^+$  physical contamination in the sample is observed (left). Events on the peak, inside the window mass 5.15 GeV - 5.35 GeV, are selected. These events are misreconstructed as  $B_s^0 \rightarrow J/\psi \pi^+ \pi^-$  decays (right). A non-parametric function describes the shape of the misreconstructed  $B^+$  decays [53].

where  $\mu_b$  and  $\sigma_b$  are the mean and the width of the Gaussian. On the other hand, the combinatorial background mass distribution is described by an exponential function

$$M_b^{\text{comb}}(m_j; a_0) = e^{a_0 m_j}, \quad (2.12)$$

being  $a_0$  a constant parameter. The contamination  $M_p(m_j)$  from  $B^\pm \rightarrow J/\psi K^\pm$  decays is modeled by a non-parametric function [53] extracted from data, as figure 2.6 describes.

The  $\lambda$  distribution is parameterized by an exponential decay convoluted with the resolution function  $R$

$$T_s(\lambda_j, \sigma_{\lambda_j}) = \frac{1}{\lambda_B} \int_0^\infty R(x - \lambda_j, \sigma_j) \exp\left(\frac{-x}{\lambda_B}\right) dx, \quad (2.13)$$

with  $\lambda_B = c\tau$  of the  $B_s^0$  to be measured and

$$R(\lambda_j, \sigma_{\lambda_j}) = \frac{1}{\sqrt{2\pi}\sigma_j} \exp\left[\frac{-\lambda_j^2}{2(\sigma_j)^2}\right]. \quad (2.14)$$

The background  $\lambda$  distribution  $T_b(\lambda_j)$  is parametrized by the sum of two exponential decay functions modeling combinatorial background and an exponential decay for the cross-feed contamination. An exponential decay describes  $T_p(\lambda_j)$  that accounts  $B^+$  decays.

The distribution of the  $\lambda$  uncertainty  $E_s(\sigma_{\lambda_j})$  is modeled by an exponential convoluted with a Gaussian with decay constant  $1/\gamma$ , convoluted with a Gaussian function with mean  $\epsilon$  and width  $\delta$ :

$$E_s(\sigma_{\lambda_j}; \gamma, \epsilon, \delta) = \frac{1}{\gamma} e^{-x/\gamma} \otimes G(x - \sigma_{\lambda_j}, \epsilon, \delta) \quad (x \geq 0), \quad (2.15)$$

and by two exponential functions convoluted with a Gaussian for the  $E_b(\sigma_{\lambda_j})$  and  $E_p(\sigma_{\lambda_j})$  background distributions.

The fit yields  $494 \pm 85$  events and a lifetime of  $c\tau = 504 \pm 42 \mu\text{m}$  for the signal component. A summary of the fit parameters is showed in table 2.1. Figures 2.7 and 2.8 show the distributions of data with the fit result superimposed. To confirm the presence of the  $f_0(980)$  resonance, the events within one  $\sigma$  of the  $B_s^0$  mass are selected, and the mass distribution of the  $\pi^+\pi^-$  pairs is fitted with a Flatté model [54], as shown in figure 2.9.

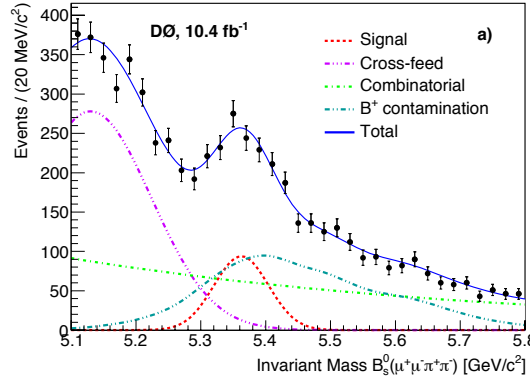


Figure 2.7: Invariant mass distribution for  $B_s^0$  candidates. The model obtained from the fit and each one of its components are superimposed [55].

### 2.5.3 Systematic uncertainties

Several sources of systematic uncertainty are considered. Table 2.2 summarizes the uncertainties with its source and the total uncertainty, determined by combining individual uncertainties in quadrature. The uncertainty related to alignment has been previously determined.

Parameter	Min	Max	Initial Value	Final Value
Mass model:				
Mean of signal Gaussian ( $\text{GeV}/c^2$ )	5.350	5.400	5.350	$5.362 \pm 0.005$
Width of signal Gaussian ( $\text{GeV}/c^2$ )	0.000	0.150	0.004	$0.042 \pm 0.004$
Mean of cross-feed background ( $\text{GeV}/c^2$ )	5.000	5.500	5.000	$5.130 \pm 0.012$
Width of cross-feed background ( $\text{GeV}/c^2$ )	0.000	0.100	0.080	$0.093 \pm 0.011$
Number of signal events	0	10,000	500	$494 \pm 85$
Number of background events	0	10,000	3,000	$4,027 \pm 162$
Number of misreconstructed $B^+$ events	0	10,000	1,000	$1,511 \pm 178$
Cross-feed background fraction	0.000	1.000	0.500	$0.494 \pm 0.040$
Combinatorial background exp. coef.	-10.000	10.000	-1.000	$-1.485 \pm 0.196$
Proper transverse decay length model:				
Long-lived background decay constant	0.000	1.000	0.050	$0.002 \pm 0.004$
Short-lived background decay constant	0.000	1.000	0.050	$0.0097 \pm 0.0024$
Long-lived background fraction	0.000	1.000	0.500	$0.0720 \pm 0.1568$
$B^+$ background decay constant	0.000	1.000	0.050	$0.0267 \pm 0.0014$
Cross-feed background decay	0.000	1.000	0.040	$0.0421 \pm 0.0015$
Signal lifetime $c\tau$ ( $\mu\text{m}$ )	10.0	1,000.0	500.0	$504.0 \pm 42.4$

Table 2.1: Summary of parameters for the fits and results of the  $B_s^0$  lifetime measurement.

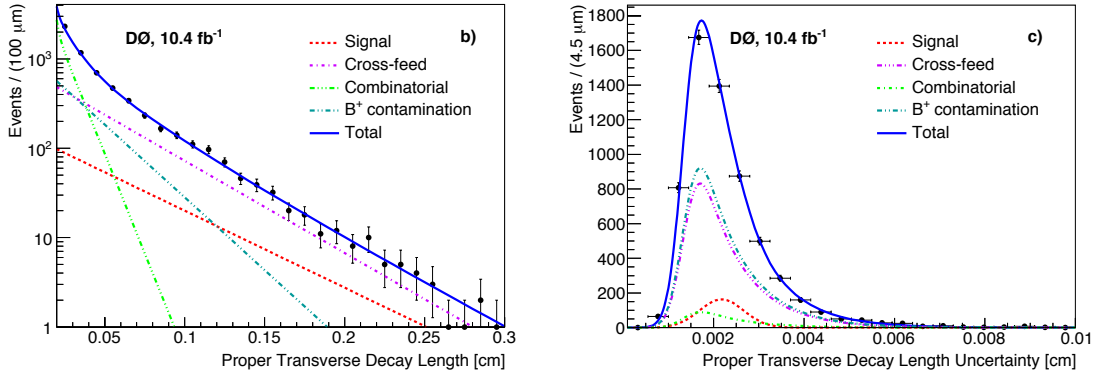


Figure 2.8: Proper transverse decay length distribution (left) and proper transverse decay length uncertainty (right) for  $B_s^0$  candidates. The model obtained from the fit and each one of its components are superimposed [55].

The  $\pi^+\pi^-$  invariant mass window is varied from its nominal width of  $200 \text{ MeV}/c^2$  to between 160 and  $240 \text{ MeV}/c^2$ . The modeling and fitting method is tested with data generated in pseudoexperiments, in which a bias of  $-4.4 \mu\text{m}$  arises for an input lifetime of  $500 \mu\text{m}$  and 500 signal events. This bias is corrected in the nominal result. Finally, the parametrization of the models used to describe the distributions are changed, and the variation with respect to the nominal result is taken as a systematic uncertainty. Appendix A shows further details in the systematic uncertainties estimation.

Source	Variation ( $\mu\text{m}$ )
Alignment	5.4
$\pi^+\pi^-$ invariant mass window	8.0
Fit bias	4.4
Distribution models	12.5
<b>Total (combining in quadrature)</b>	<b>16.4</b>

Table 2.2: Summary of systematic uncertainties.

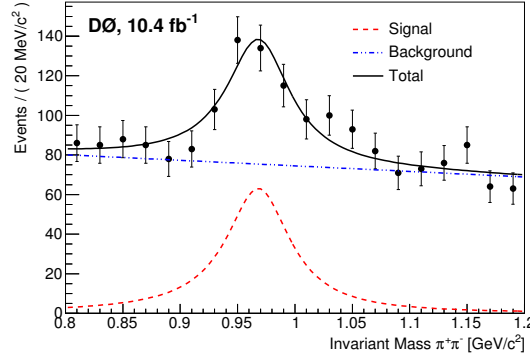


Figure 2.9: Invariant mass distribution of the  $\pi^+\pi^-$  pairs coming from events within  $\pm 1\sigma$  of the  $B_s^0$  mass [55].

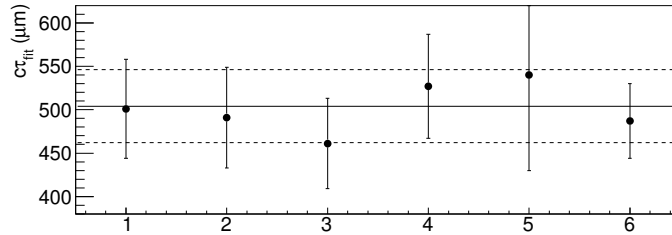


Figure 2.10: Fitted lifetime values in consistency tests selecting  $B_s^0$  mesons with (1)  $\eta > 0$ , (2)  $\eta < 0$ , (3)  $\phi > \pi$ , (4)  $\phi < \pi$ , (5) Run IIa and (6) Run IIb. The lines represent the nominal value.

### 2.5.4 Cross checks

To test the stability of the lifetime measurement of the  $B_s^0$  meson, we split each data sample according to different kinematic and geometric parameters (1)  $\eta > 0$ , (2)  $\eta < 0$ , (3)  $\phi > \pi$ , (4)  $\phi < \pi$ , and compared the fit results for each case. We split the data into DØ Run IIa (5) and Run IIb (6) too. In all cases, we found the lifetimes consistent with the nominal measurement within their uncertainties. Figure 2.10 shows the results of this comparison.

Using the  $B^\pm$  background component extracted from the data, we performed a fit for the lifetime of this component of the background. The result is in good agreement with the values

obtained from the global fit. We have also fit the lifetime of the cross-feed contamination from the simulation and again consistency with the nominal result is observed.

In order to estimate the effect of a small non CP-odd component in the analysis, we performed the fit with two exponential decay components for the signal, with the lifetime of one of them fixed to the world average of the CP-even  $B_s^0$  lifetime [35], and its fraction to be 0.01 as found by the LHCb experiment [50]. The lifetime fit finds a variation of 1  $\mu\text{m}$  with respect to the nominal fit result.

### 2.5.5 Results

In summary, the lifetime of the  $B_s^0$  is measured [55], obtaining:

$$c\tau(B_s^0) = 508 \pm 42 \text{ (stat)} \pm 16 \text{ (syst)} \mu\text{m}, \quad (2.16)$$

from which:

$$\tau(B_s^0) = 1.70 \pm 0.14 \text{ (stat)} \pm 0.05 \text{ (syst)} \text{ ps}, \quad (2.17)$$

in the decay channel  $B_s^0 \rightarrow J/\psi \pi^+ \pi^-$  with  $880 \leq M_{\pi^+ \pi^-} \leq 1080 \text{ MeV}/c^2$ .

Our result is in good agreement with previous measurements from LHCb and CDF collaborations, and the later measurement from CMS (See Fig. 8.1) It also provides an independent confirmation of the longer lifetime for the CP-odd eigenstate of the  $B_s^0/\bar{B}_s^0$  system.



## Chapter 3

---

### Tau Lepton Physics

In 1975 at SLAC, the collaboration later known as MARK I, reported the observation of anomalous lepton production [56]. With a maximum energy of 4.1 GeV in the  $e^+e^-$  collider SPEAR, the collaboration found events in which acollinear electrons and muons of opposite charge were observed, accompanied with missing momentum of the event. Below certain energy threshold, these “lepton flavor violating” effects disappeared (See Fig 3.1). It was latter confirmed that the source of  $e\mu$ +missing momentum events is a pair of leptons heavier than the electron and the muon [57]. They called the new lepton as  $\tau$  [58], for the first letter of the word  $\tau\rho\iota\tau\omicron\varsigma$ , which means the third. The discovery of the  $\tau$  lepton led to the Nobel Prize for physics awarded to Martin Perl in 1995.

In this chapter, the measurement of basic properties of the  $\tau$  lepton are discussed. Mass, lifetime and branching ratio of their decay channels characterize the heavy lepton discovered by Perl. The phenomenology of semileptonic  $\tau$  decays and the structure of resonances is also described.

#### 3.1 $\tau$ Lepton Mass

The  $\tau$  lepton mass,  $m_\tau$ , is one of the fundamental parameters of the Standard Model. Its precise measurement is crucial for tests of the Standard Model such as lepton universality.

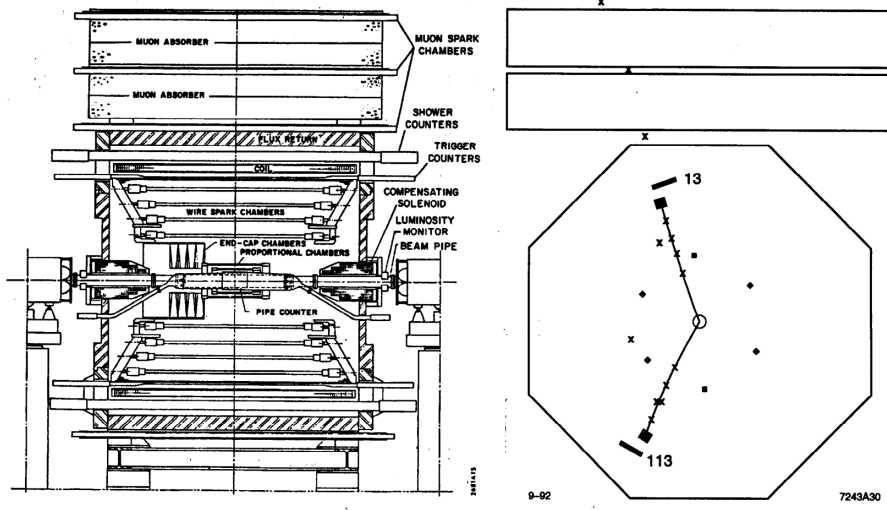


Figure 3.1: The Mark I detector with one of the  $e\mu$  events displayed, as showed at [56]. The  $\mu$  moves upward and the  $e$  moves downward. The numbers 13 and 113 give the relative amount of energy deposited by the  $\mu$  and the  $e$ .

To date, two main techniques are used for the determination of  $m_\tau$ : production threshold and pseudomass technique.

The simplest way to measure the mass of the  $\tau$  lepton is a scan of the production threshold. In 1978, the DELCO collaboration was the first to determine  $m_\tau$  [59], finding the center-of-mass  $e^+e^-$  collision energy at which  $\tau$  production appears. With 692 observed  $\tau$  pair events, DELCO reported a mass of  $1782^{+2}_{-7} \text{ MeV}/c^2$ .

The threshold method is also the most precise to date. After several measurements performed by different experiments along the time, the BES III collaboration has measured the  $\tau$  lepton mass with the highest precision using this technique [60], reporting a measurement of  $m_\tau = (1776.91 \pm 0.12^{+0.13}_{-0.10}) \text{ MeV}/c^2$ .

The method described above can be used only by experiments running near the  $\tau$  production threshold. The ARGUS collaboration was the first one to measure  $m_\tau$  using a different method, called pseudomass technique [61]. Using an integrated luminosity of  $341 \text{ pb}^{-1}$  with an  $e^+e^-$  collision energy between 9.4 and 10.6 GeV, ARGUS performed a mass measurement

using the channel  $\tau \rightarrow 3\pi\nu$ , obtaining  $m_\tau = (1776.3 \pm 2.4 \pm 1.4) \text{ MeV}/c^2$ .

The pseudomass technique also allows to perform a test of CPT violation, measuring independently the mass of  $\tau^+$  and  $\tau^-$ . The Belle and BaBar collaborations performed measurements using the pseudomass technique, getting  $m_\tau = (1776.61 \pm 0.13 \pm 0.35) \text{ MeV}/c^2$  and  $m_\tau = (1776.68 \pm 0.12 \pm 0.41) \text{ MeV}/c^2$ , respectively, and putting also an upper limit in the difference between the  $\tau^+$  and  $\tau^-$  masses, setting upper limits of  $(m_{\tau^+} - m_{\tau^-})/m_\tau < \sim 3 \times 10^{-4}$  at 90% confidence level [62, 63].

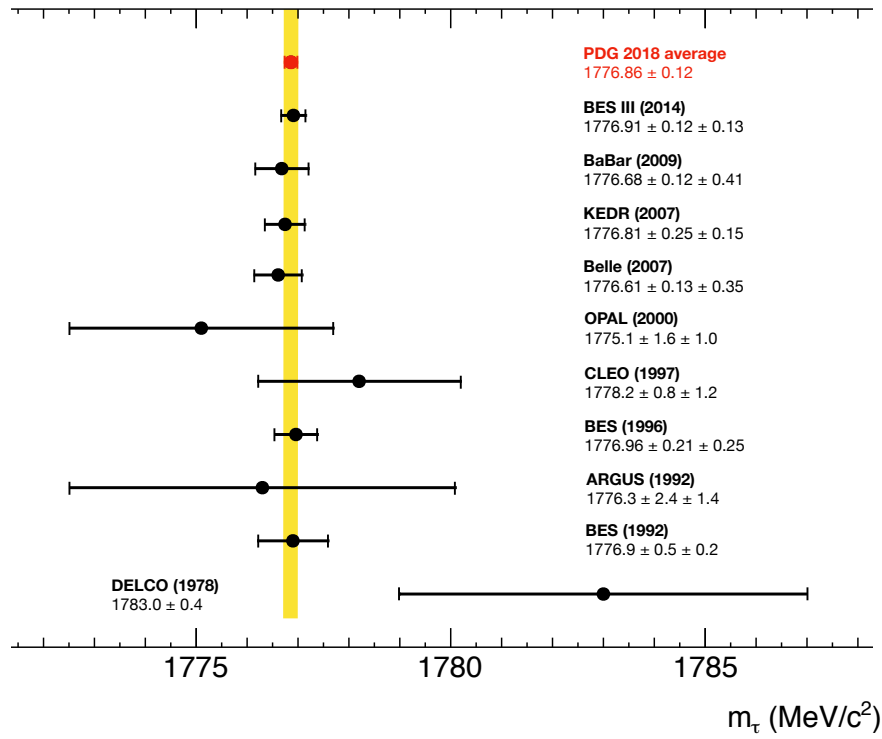


Figure 3.2: Compilation of most recent  $\tau$  mass measurements. The average reported by the PDG 2018 [64] is represented by the yellow line.

## 3.2 $\tau$ Lepton Lifetime

Using a sample of 1500  $\tau^+\tau^-$  pairs, produced at the center of mass energy of 29 GeV, the Mark II collaboration at SLAC performed for the first time a measurement of the  $\tau$

lepton lifetime. They used the vertex projection of 3-prong tau decays to determine the flight distance between the interaction point and the decay vertex, reporting a lifetime of  $\tau_\tau = (4.6 \pm 1.9 \times 10^{-13})$  s [65].

Several methods to measure the  $\tau$  lifetime have been implemented. Each one of them uses different decay topologies and deals with a variety of systematic uncertainties. Figure 3.3 shows the most recent lifetime measurements performed by several collaborations. The latest one, reported by Belle collaboration, reduces significantly the measurement uncertainties. Belle performed the analysis using 3-prong decays in both  $\tau^+\tau^-$  created in the collision of electron and positron. At an asymmetric-energy collider such as KEKB, the one who provides the collisions for Belle, the laboratory frame angle between the  $\tau^+$  and the  $\tau^-$  is not equal to 180 degrees, so the collision point can be found from the intersection of the two  $\tau$  lepton trajectories. Using kinematic constrictions, the direction of each  $\tau$  lepton can be determined with a twofold ambiguity, allowing the high precision measurement reported,  $\tau_\tau = (290.17 \pm 0.53(\text{stat}) \pm 0.33(\text{syst})) \times 10^{-15}$  s [66]. Additionally, a B-factory as Belle has the capacity of measuring the lifetime of  $\tau^+$  and  $\tau^-$  independently, with the result  $(\tau_{\tau^+} - \tau_{\tau^-})/\tau_{\text{average}} < 7.0 \times 10^{-3}$  at 90% C.L. [66]. This provides a test of CPT symmetry using  $\tau$  lifetimes.

### 3.3 Branching Ratios of $\tau$ Decays

The  $\tau$  lepton is massive enough to decay into leptons and hadrons. More than 200 decay channels have been reported so far by experiments [64]. The measurement of branching ratios of exclusive  $\tau$  decays depends on the knowledge of the produced  $\tau$  leptons and the identification of the final state particles for each  $\tau$  decay. The first one can be obtained from the cross section  $\sigma(e^+e^- \rightarrow \tau^+\tau^-)$ , which is well known. The final state identification depends on experimental aspects.

The simplest way to classify the  $\tau$  lepton decays is using the topology of the decay. Following the convention used in  $\tau$  lepton physics, in this work ‘prong’ refers to the number of

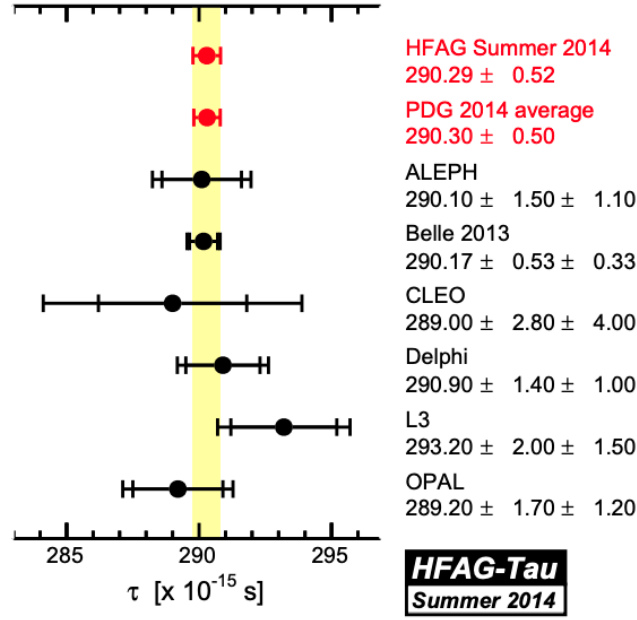


Figure 3.3: Compilation of most recent  $\tau$  lifetime measurements by the HFAG-Tau 2014 [67]. The average is represented by the yellow line.

charged particles in the final state of the decay. The phase space in a  $\tau$  decay is big enough to produce up to 12 pions. However, only one, three and five prong decays have been observed. Current average from measurements of branching ratio, reported by the Particle Data Group (PDG), for 1-prong decays is 85.26% [64]. 3-prong and 5-prong decays have branching ratios of 14.55% and  $9.9 \times 10^{-4}$ , respectively. The current limit for a 7-prong decay is  $\text{BR}(\tau^- \rightarrow 4h^- 3h^+ \geq 0 \text{ neutrals } \nu) < 3.0 \times 10^{-7}$  at 90% C.L. [68].

The other possibility is classifying the decays as leptonic and semileptonic, in function of the final state particles nature. Leptonic decays correspond to the processes  $\tau \rightarrow \nu_\tau e \bar{\nu}_e$  and  $\tau \rightarrow \nu_\tau \mu \bar{\nu}_\mu$ . Figure 3.4 (a) shows the Feynman diagram of a leptonic decay at tree level. The process may be treated as an effective four fermion interaction, adding the non-locality of the  $W^\pm$  propagator as a correction.

1. According to the electroweak theory, the leptonic decay of a lepton  $\ell$  into a lighter one

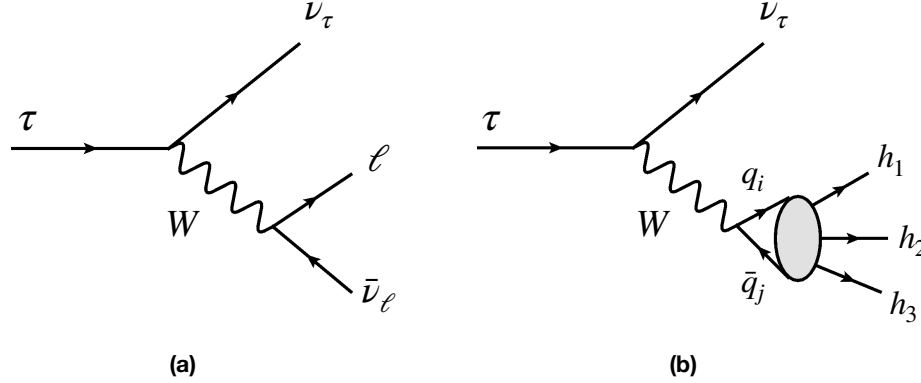


Figure 3.4: Feynman diagrams of  $\tau$  decays at tree level. (a) Leptonic decay and (b) semileptonic decay, with hadronization of the produced quark pair from the charged weak current.

$\ell'$  is described by

$$\Gamma(\ell \rightarrow \ell' \nu_\ell \bar{\nu}_{\ell'}) = \frac{G_{\ell\ell'}^2 m_\ell^5}{192\pi^3} f(m_{\ell'}^2/m_\ell^2)(1 + \Delta_{\ell\ell'}), \quad (3.1)$$

where  $G_{\ell\ell'}$  is an effective coupling introduced to account for electroweak corrections [69, 70],  $f(x) = 1 - 8x + 8x^3 - x^4 - 12x^2 \log x$  and  $\Delta_{\ell\ell'}$  contains QED corrections [71, 72]. The averages reported by PDG [64] for branching ratios of leptonic  $\tau$  decays are

$$\text{BR}(\tau^- \rightarrow \nu_\tau e^- \bar{\nu}_e) = (17.82 \pm 0.05)\%, \quad (3.2)$$

$$\text{BR}(\tau^- \rightarrow \nu_\tau \mu^- \bar{\nu}_\mu) = (17.33 \pm 0.05)\%. \quad (3.3)$$

These are the most precisely determined  $\tau$  decay fractions, mostly because the absence of hadronic contamination in the process. This feature makes decays of  $\tau$  leptons an excellent place to test lepton universality with all three leptons. Together with muon decays, it can test lepton universality in a clean way beyond  $10^{-3}$  accuracy if better measurements of the mass and lifetime of the tau lepton are achieved.

2. In the case of the semileptonic decays, the process is described in form of a current-current interaction. Assuming a  $V - A$  structure

$$\mathcal{M}(\tau^- \rightarrow \text{hadrons}^- \nu_\tau) = \frac{G_F}{\sqrt{2}} \bar{\nu}_\tau \gamma_\mu (1 - \gamma_5) \tau H^\mu, \quad (3.4)$$

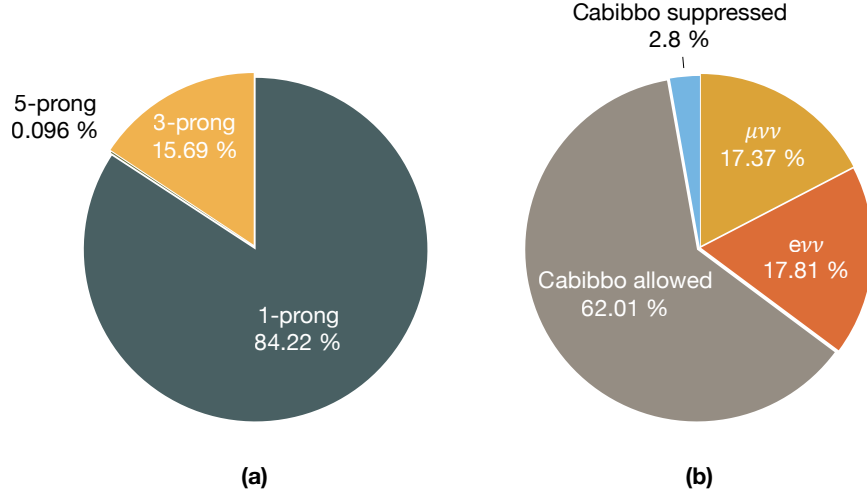


Figure 3.5: Branching ratios of  $\tau$  lepton decays reported in reference [64] classified by (a) topology and (b) leptonic, Cabibbo allowed and Cabibbo suppressed. Values displayed are re-weighted for a sum of 100%.

with

$$H^\mu = \langle \text{hadrons} | (V_{ud}^* \bar{d} + V_{us}^* \bar{s}) \gamma^\mu (1 - \gamma_5) u | 0 \rangle. \quad (3.5)$$

It means, semileptonic decays can be classified into Cabibbo allowed ( $V_{ud}^*$  part) and Cabibbo suppressed ( $V_{us}^*$  part). Figure 3.5 shows the percentage of  $\tau$  decays into leptonic, Cabibbo allowed and suppressed modes. Semileptonic decays will be discussed with more detail in section 3.4.

Given the large amount of semileptonic decays, they can also be classified as exclusive and inclusive channels. Inclusive channels can be predicted in a relatively clean way based on QCD. The measurement of the associated branching fractions or spectral functions play a very important role in the extraction of the  $V_{us}$  CKM matrix element or the determination of the strong coupling constant at the lowest energy scale. On the other hand, exclusive channels are more difficult to predict from the first principles of the SM, given the involved energy scale of the decay processes which requires reliable predictions of non-perturbative form factors.

### 3.4 Semileptonic $\tau$ Decays

As mentioned before, the  $\tau$  lepton is the only lepton massive enough to decay into hadrons. The exhaustive analysis of semileptonic  $\tau$  decays provides a clean environment for tests of theoretical QCD processes with the first and second generation of quarks involved.

Before the discovery of the  $\tau$  lepton, the decay of a heavy lepton into hadrons was studied by Paul Tsai [36]. Ignoring the exchange of an intermediate  $W^\pm$  boson, the amplitude can be described as the interaction between leptonic and hadronic currents. From (3.4)

$$d\Gamma(\tau \rightarrow \text{hadrons}^- \nu_\tau) = \frac{G_F^2}{4M_\tau} |V_{\text{CKM}}|^2 L_{\mu\nu} H^{\mu\nu} d\Phi, \quad (3.6)$$

being  $|V_{\text{CKM}}|$  the CKM matrix element,  $L_{\mu\nu}$  the leptonic tensor and  $H^{\mu\nu}$  the hadronic tensor, with a Lorentz invariant phase space element  $d\Phi$ . The hadronic tensor obeys a Lorentz invariant construction with structure functions embedded [73]. For the simplest semileptonic decay modes  $\tau^- \rightarrow \pi^- \nu_\tau$  and  $\tau^- \rightarrow K^- \nu_\tau$ , the structure functions are reduced to

$$\langle P^-(p) | \bar{d} \gamma^\mu \gamma_5 u | 0 \rangle = -i\sqrt{2} f_P p^\mu, \quad (3.7)$$

where  $P^- = \pi^-, K^-$ . The matrix elements (3.7) are well known from the measured decays  $\pi \rightarrow \mu \bar{\nu}_\mu$  and  $K \rightarrow \mu \bar{\nu}_\mu$ .

Decays into two pseudoscalar mesons  $\tau \rightarrow P^- P^0 \nu_\tau$  are mediated by a vector current. The hadronic matrix element can be parametrized with vector and induced scalar form factors  $F_+^{PP'}$  and  $F_0^{PP'}$ :

$$\langle P^- P^0 | \bar{d}_i \gamma^\mu u | 0 \rangle = C_{PP'} \left[ \left( p_- - p_0 - \frac{\Delta_{PP'}}{s} q \right)^\mu F_+^{PP'}(s) + \frac{\Delta_{PP'}}{s} q^\mu F_0^{PP'}(s) \right], \quad (3.8)$$

where  $p_-^\mu$  and  $p_0^\mu$  are the momenta of charged and neutral pseudoscalar particles, respectively,  $q^\mu = (p_- + p_0)^\mu$  and  $s = q^2$ . Except in the case in which  $PP' = \pi^- \eta^{(\prime)}, K\pi^-$  or  $K^- \eta^{(\prime)}$ , the mass square difference  $\Delta_{PP'} = m_{p_-}^2 - m_{p_0}^2$  suppresses the scalar contribution because the vector current is conserved in the limit of isospin symmetry, in which the quarks have equal mass.  $C_{PP'}$  is a global normalization coefficient, chosen in the way the vector form factor



$F_V(s)$  is 1 at lowest order in chiral perturbation theory [74], then

$$C_{\pi\pi} = \sqrt{2}, \quad C_{K\bar{K}} = -1, \quad C_{K\pi} = \frac{1}{\sqrt{2}}, \quad C_{\pi\bar{K}} = -1, \quad C_{K\eta} = \sqrt{\frac{3}{2}}. \quad (3.9)$$

Higher multiplicity modes contain a richer dynamical structure, but these decay modes are harder to be described.

Semileptonic  $\tau$  decays show a rich structure on resonances, making them a good place for the study of meson dynamics. Several  $\tau$  decay modes have been analyzed for their resonance structure. The intermediate  $W^\pm$  couples only to quarks with a total angular momentum  $J = 0$  or 1, which means states with  $J \geq 2$  will not be observed.

Table 3.1 shows the quantum numbers of the hadronic final states accessible by Cabibbo-allowed  $\tau$  decays and the mechanisms of suppression. Each final state may be reached through intermediate resonances. There are only two channels,  $J^{PG} = 1^{-+}$  and  $J^{PG} = 1^{+-}$ , which are not suppressed by any mechanism. These corresponds to the decay channels  $\tau \rightarrow \rho \nu_\tau$  and  $\tau \rightarrow a_1 \nu_\tau$ , being  $\rho$  preferred by phase space. This is consistent with  $\tau \rightarrow \pi\pi^0 \nu_\tau$  having the largest branching ratio of all the possible  $\tau$  decays,  $\text{BR}(\tau \rightarrow \pi\pi^0 \nu_\tau) = (25.49 \pm 0.09)\%$ , and dominated by the intermediate vector state  $\rho$  [75]. The presence of  $\rho$  excitations, as  $\rho'(1450)$ , has also been clearly identified.

The decay  $\tau^- \rightarrow (3\pi)^- \nu_\tau$  is the cleanest to study axial-vector resonances structure. It is dominated by the  $a_1$  state with  $J^{PG} = 1^{+-}$ . OPAL and DELPHI collaborations have performed a model-independent analysis of the hadronic structure of  $\tau^- \rightarrow (3\pi)^- \nu_\tau$  and no evidence for vector or scalar currents has been found [76, 77].

### 3.5 Standard Model tests in $\tau$ decays

Precise measurements of the lepton properties provide tests of the SM and accurate determinations of its parameters. The large mass of the  $\tau$  lepton opens the possibility to study many kinematically-allowed decay modes and extract relevant dynamical information. A global fit of the available experimental measurements is used to determine the  $\tau$  branching fractions,

$J^{PG}$	Suppression mechanism	Accessible resonance
$0^{++}$	Isospin, exotic	-
$0^{+-}$	Isospin, SCC	$a_0(980)$
$0^{-+}$	Helicity, exotic	-
$0^{--}$	Helicity	$\pi(1300)$
$1^{++}$	SCC	$b_1(1235)$
$1^{+-}$	-	$a_1(1260)$
$1^{-+}$	-	$\rho(770), \rho(1450)$
$1^{--}$	SCC, exotic	-

Table 3.1: Summary of the hadronic final states accessible through Cabibbo-allowed  $\tau$  decays. Suppression mechanisms are also indicated, where SCC means second-class current (discussed in chapter 6) and 'exotic' means a state not produced from a quark-antiquark state.

taking into account uncertainties and statistical correlations [67]. The  $\tau$  branching fractions provide tests for theoretical predictions based on the SM and they can be further elaborated to determine the CKM matrix element  $|V_{us}|$  and the QCD coupling constant  $\alpha_s$  at the  $\tau$  lepton mass.

The separate measurement of the Cabibbo-allowed and Cabibbo-suppressed  $\tau$  decay widths provides a very clean determination of the CKM matrix element  $V_{us}$  [78]

$$|V_{us}| = \sqrt{R_S / \left[ \frac{R_{VA}}{|V_{ud}|^2} - \delta R_{\text{theory}} \right]}, \quad (3.10)$$

where  $R_{VA}$  is the ratio between the sum of the partial width of the non-strange hadronic final states and the electronic partial width,  $R_S$  is the ratio between width of the strange hadronic final states and the partial width, and  $\delta R$  is determined from low energy QCD theory [78, 79, 80].  $|V_{us}|$  can be also determined from the ratio of the branching fractions  $\text{BR}(\tau^- \rightarrow K^- \nu_\tau) / \text{BR}(\tau^- \rightarrow \pi^- \nu_\tau)$  [81]. Figure 3.6 shows the  $|V_{us}|$  determinations using  $\tau$  and kaon

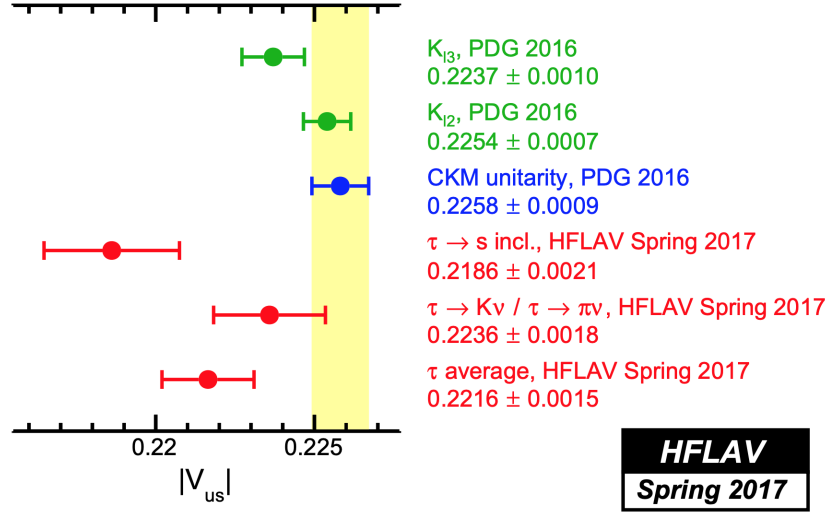


Figure 3.6: HFLAV  $|V_{us}|$  determinations using  $\tau$  branching ratios [81], compared to  $|V_{us}|$  determinations based on kaon data and CKM-unitarity determinations [82].

decays data. It is clear that all  $|V_{us}|$  measurements based on  $\tau$  branching ratios are about  $1\sigma$  lower than the kaon data and CKM-unitarity determinations [82].

The inclusive hadronic decay width of the  $\tau$  lepton is a clean observable to determine the strong coupling  $\alpha_s(m_\tau)$  with high precision. It is a very important measurement in the sense that the  $\alpha_s(m_\tau)$  measurement is the best proof of the predicted QCD running [83]. Figure 3.7 shows the evolution of the strong coupling to higher energies. The  $\alpha_s(m_\tau)$  determination can be improved from future high-precision measurements of the  $\tau$  spectral functions, mainly in the higher kinematically-allowed energy bins. A better estimation of higher-order perturbative corrections will improve the theoretical accuracy [83].

Further SM tests can be performed using  $\tau$  lepton data. The leptonic decays probe the structure of the weak currents and the universality of their couplings to the  $W$  boson. Lepton flavor and number violation decays may constitute a clear indication of physics BSM. New physics interactions such as scalar and tensor currents can be constrained in rare  $\tau$  decays. In the next chapters, several topics involving BSM searches in  $\tau$  lepton decays are described.

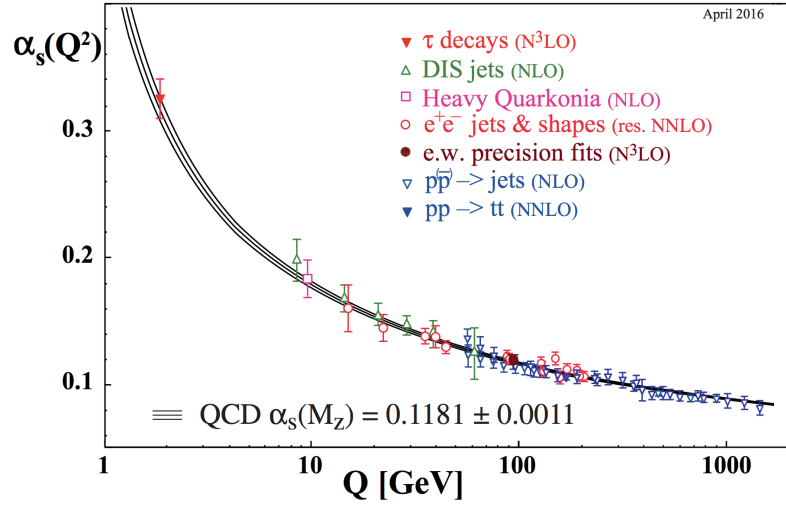


Figure 3.7: Evolution of the strong coupling  $\alpha_s(m_\tau)$  to higher energies and comparison with direct measurements performed by several experiments [82].

# Chapter 4

---

## The Belle II Experiment

A B-factory is a machine that collides electrons and positrons mainly at 10.58 GeV, which corresponds to the  $\Upsilon(4S)$  resonance energy, producing a large amount of B meson pairs. It provides a clean environment for precision measurements and searches of physics beyond the Standard Model. In particular, a B-factory has several advantages in the study of hadronic  $\tau$  decays respect to other experiments. At the  $\Upsilon(4S)$  resonance energy, the cross section of the process  $e^+e^- \rightarrow \tau^+\tau^-$  is of the same order of magnitude as the production of a B pair from the  $e^+e^-$  collision:

$$\sigma(e^+e^- \rightarrow \Upsilon(4S)) = 1.05\text{nb},$$

$$\sigma(e^+e^- \rightarrow \tau^+\tau^-) = 0.92\text{nb}.$$

That is why it is usually said a B-factory is also a  $\tau$  lepton factory.

The B-factory of second generation Belle II, coupled to the SuperKEKB accelerator, expects to provide an integrated luminosity of  $50\text{ ab}^{-1}$  at the end of its operation, a sample 50 times larger than the provided by the first generation of B-factories. The physics program of Belle II will take advantage of the large amount of data in order to perform high precision measurements. In this chapter, the main aspects of the Belle II experiment are described.

## 4.1 Integrated Luminosity at SuperKEKB

The amount of collisions produced in an accelerator are described by the luminosity  $L$ , defined as the collision rate per cross section

$$L = \frac{1}{\sigma} \frac{dN}{dt}, \quad (4.1)$$

where  $N$  is the number of observed events,  $t$  is the time and  $\sigma$  represents the cross section of the observed events. The integrated luminosity  $L_{int}$  is given by

$$L_{int} = \int L dt. \quad (4.2)$$

$L_{int}$  is a parameter describing the number of events produced in collisions. Knowing the integrated luminosity delivered by a collider, it is possible to get the number of collisions

$$N = L_{int} \cdot \sigma. \quad (4.3)$$

Units of  $L_{int}$  in the cgs system are  $\text{cm}^{-2}$ . It is common to use the barn (b) as unit, defined as  $1b = 10^{-24} \text{cm}^2$ .

The first generation of B-factories, Belle coupled to KEKB and Babar coupled to PEP-II, recorded a combined sample of  $1.5 \text{ ab}^{-1}$ , corresponding to about 1 billion of tau pair decays (See Fig. 4.1). In June of 2010, KEKB operations stopped and an upgrade to a Super-B factory called SuperKEKB started.

SuperKEKB uses the same tunnel and many parts of KEKB (See Fig 4.2), setting the beam energies to 7 GeV for the electrons and 4 GeV for the positrons circulating in opposite direction, giving a collision at the energy of the resonance  $\Upsilon(4S)$  in the center-of-mass system. At the interaction region, the nano-beam scheme will be used, increasing the instantaneous luminosity to  $8 \times 10^{35} \text{ 1/cm}^2\text{s}$ , a factor of 40 larger with respect to KEKB (See Fig. 4.3). This represents experimental challenges as higher background coming from radiative Bhabha events, Touschek effect and beam gas scattering, with higher trigger rates expected for the detectors [84].

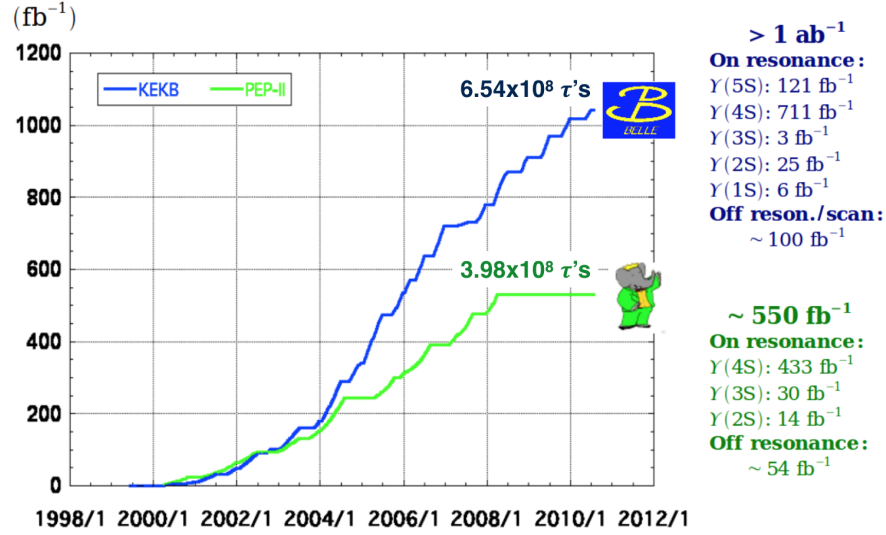


Figure 4.1: Integrated luminosity by year recorded by the colliders PEP-II y KEKB. Estimated number of  $\tau$ -pair events produced is indicated.

	PEP-II	KEKB	SuperKEKB
Detector	BaBar	Belle	Belle-II
Starting year	1999	1999	2018
End of operations	2008	2010	-
Beam energy (GeV)	$e^-$ : 9.0 $e^+$ : 3.1	$e^-$ : 8.0 $e^+$ : 3.5	$e^-$ : 7.0 $e^+$ : 4.0
Luminosity ( $10^{30} \text{ cm}^{-2} \text{ s}^{-1}$ )	12069	21083	$8 \times 10^5$

Table 4.1: Comparison between the B-factories of first generation, PEP-II and KEKB, and SuperKEKB.

## 4.2 The Belle II Detector

Detection of the high-rate collisions produced at SuperKEKB requires also an upgrade of the detector coupled to the accelerator. Belle II is the name of the detector coupled to Su-

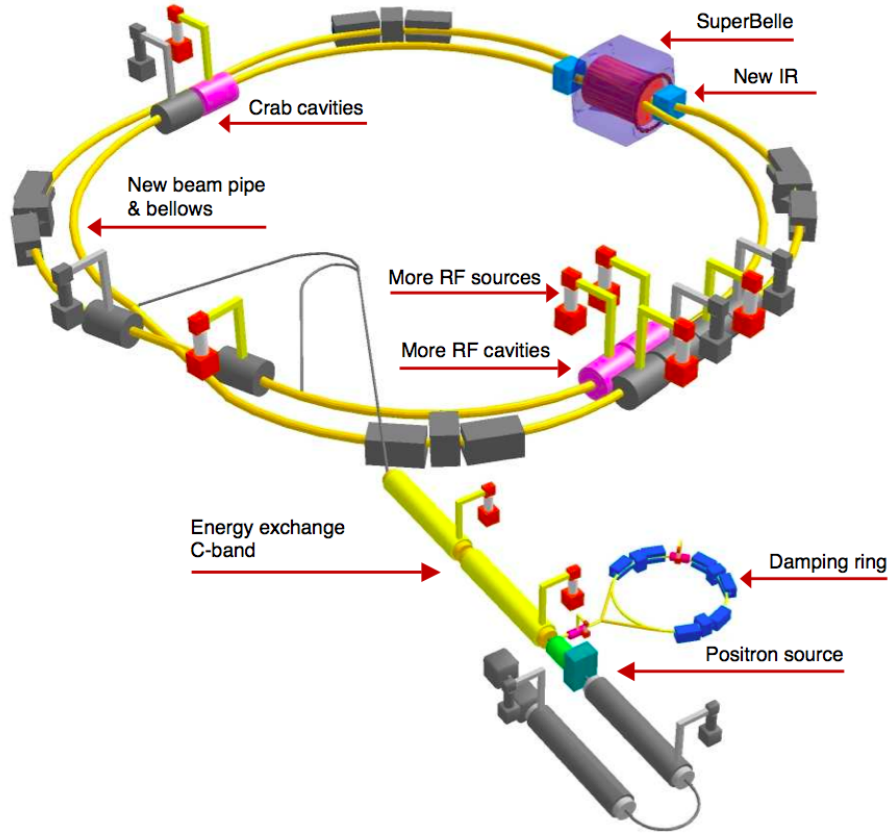


Figure 4.2: The SuperKEKB accelerator with its main parts described [85].

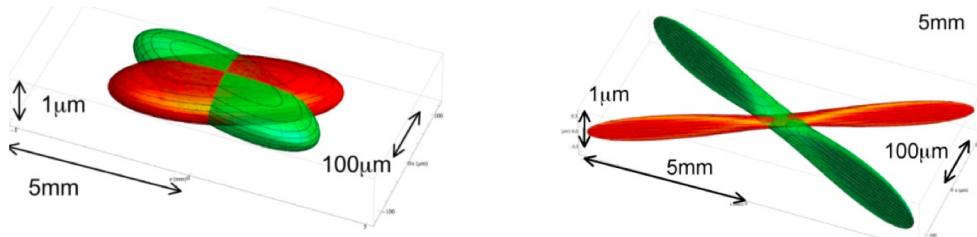


Figure 4.3: Nano-beam scheme used by SuperKEKB (right), compared respect to the size of the beam at KEKB (left). Vertical beam size is 50 nm at the interaction point in SuperKEKB [85].

perKEKB at the interaction point. Belle II keeps the design of the previous detector Belle, with major upgrades in each of their subsystems, being shortly described in this section. A complete description of Belle II can be read at reference [85].



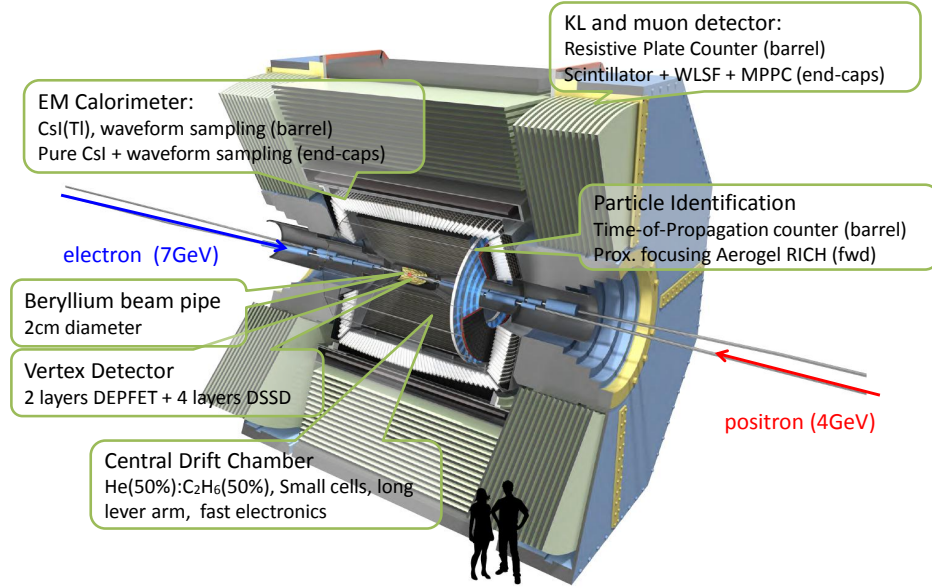


Figure 4.4: Main parts of the Belle II detector [85].

#### 4.2.1 The vertex detector (VXD)

The vertex detector is composed by two subsystems, the silicon pixel detector (PXD) and the silicon vertex detector (SVD). The first one uses two layers of DEPFET sensor type [86], and the second uses four layers of silicon strip sensors (See Fig. 4.5). Compared to the Belle vertex detector, the first two layers are closer to the interaction point and the outer layers have a larger radius. The vertex resolution is expected to be improved as a result of the modifications in the VXD. A significant improvement in the reconstruction efficiency of  $K_S^0 \rightarrow \pi^+ \pi^-$  decays is also expected.

#### 4.2.2 The central drift chamber (CDC)

The CDC is composed by 14,336 small drift cells arranged in 56 layers in axial and stereo orientation, aligned with the solenoidal magnetic field in the first case and skewed with respect to the axial direction in the second. The combination of axial and stereo layers allows for a 3D reconstruction of helix tracks. Each cell contains helium (He) and C<sub>2</sub>H<sub>6</sub> in a 50:50

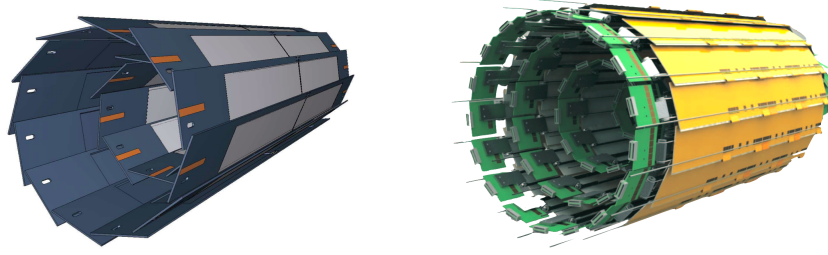


Figure 4.5: Geometric design of the DEPFET layers which compose the PXD detector (left). Silicon layers composing the SVD detector (right) [85].

mixture and the energy loss of the particles passing through the gas provides also a particle identification mechanism.

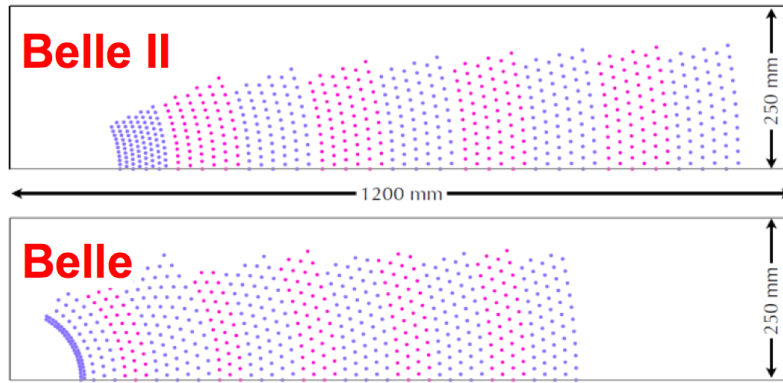


Figure 4.6: Comparison between layers of the CDC in Belle (8,400) and Belle II (14,336) [85].

### 4.2.3 The particle identification system

The particle identification system in the barrel region is a time-of-propagation (TOP) counter [87]. It is composed of 16 modules of 45 x 2 cm of quartz, with an expansion volume at the sensor end of the module (See Fig. 4.7). Two-dimensional information of a Cherenkov ring image is given by the time of arrival and impact position of the Cherenkov photons. At the end of the wedge, two rows of sixteen photon detectors with a time resolution of 100 ps are mounted.

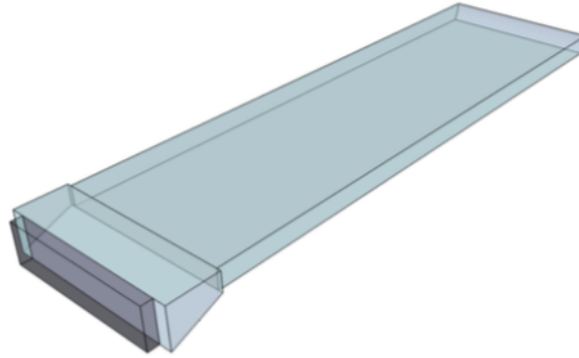


Figure 4.7: One of the modules of the TOP counter [33].

In the forward endcap region, a Cherenkov ring imaging detector (ARICH) with aerogel as Cherenkov radiator is used to identify charged particles [88]. Layers of 2cm of aerogel with different refractive indices are used, and a high granularity photon sensor is located behind each of the layers (See Fig. 4.8). The design allows a good separation of pions and kaons with a momentum from 0.4 GeV/c up to 4 GeV/c.

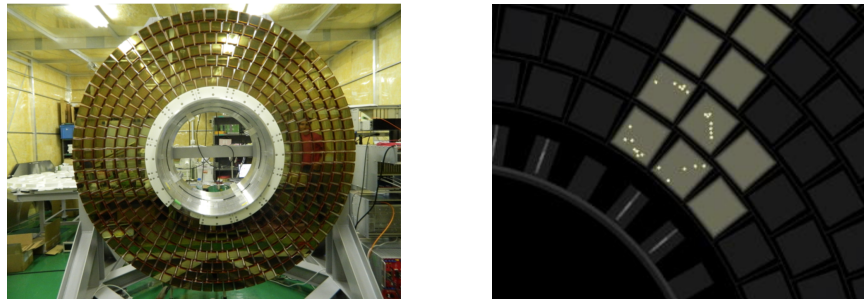


Figure 4.8: Photon detector plane of the ARICH detector (left). Reconstruction of a ring produced by a cosmic muon (right) [33].

#### 4.2.4 The electromagnetic calorimeter (ECL)

The electromagnetic calorimeter is used in the detection of photons and electrons and the determination of their energy. In the case of charged tracks reaching the ECL, it has the

capacity to distinguish electrons from hadrons. It consists of 8736 CsI(Tl) crystals located in the barrel, forward and backward endcaps, covering the 90% of the solid angle in the center-of-mass system. The readout electronics and software have been upgraded with respect to the previous Belle detector. In absence of backgrounds a similar performance as Belle is expected, with an energy resolution of  $\sigma_E/E = 4\%$  at 100 MeV and  $\pi^0$  mass resolution of  $4.5 \text{ MeV}/c^2$  [41].

#### 4.2.5 The $K_L^0$ - muon detector (KLM)

The  $K_L^0$  and muon detector (KLM) is located outside the superconducting solenoid. It consists of alternating thick iron plates and layers of scintillator strips as active detector elements, in which  $K_L^0$  mesons can shower hadronically. If a muon impacts one of the KLM layers, this will produce a photon which is detected by silicon photomultipliers.

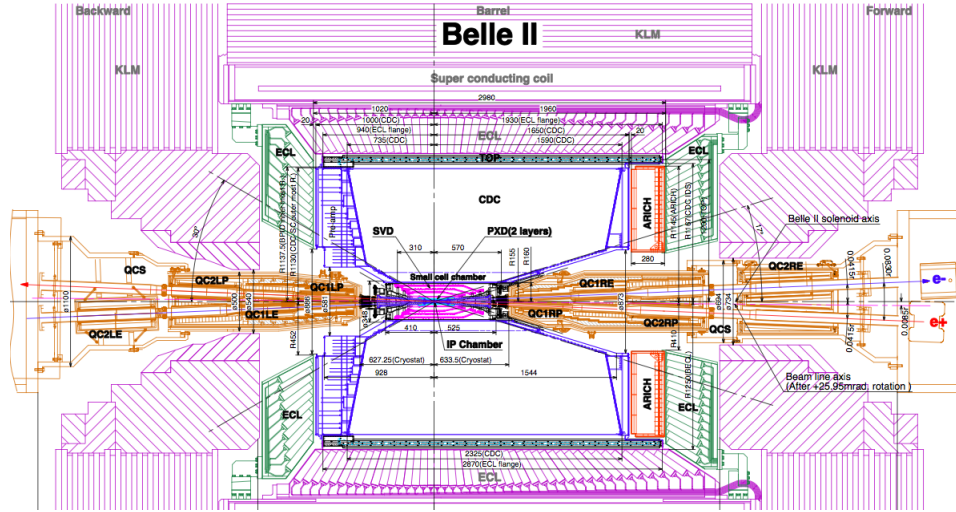


Figure 4.9: Upper view of the Belle II detector, showing where each one of the subsystems are located [33].

### 4.2.6 The trigger system

The trigger system identifies the events of physical interest during the data taking. Triggers must work efficiently in the high collision rate environment of SuperKEKB and must satisfy the limitations of the data acquisition system (DAQ).

In the case of B and D meson decays, the events are identified from the presence of at least 3 tracks in the CDC trigger and a large deposition of energy in the ECL. The efficiency for this kind of events is expected to be close to 100%. However, there is a large list of non-B-physics triggers being developed as low multiplicity, dark sectors, and  $\tau$  pair decays, which represents a challenge for the DAQ system. Additionally, the low-multiplicity topology of these processes is similar to the background coming from the beam and the collisions, leading to low purity in such triggers.

The Belle II trigger system is composed of two levels of processing: the hardware-based low-level trigger (L1) and the software-based high-level trigger (HLT). The first one has a latency of  $5\ \mu\text{s}$  and a maximum output rate of 30 kHz, limited by the read-in rate of the DAQ. The second one suppresses events to a rate of 10 kHz for storage, and it reconstructs the event with offline reconstruction algorithms, allowing access to a full event using all detectors except the PXD.

A robust trigger menu for the HLT is currently in development. Further details of the Belle II trigger system can be found at reference [33].

## 4.3 Software Framework: Basf2

Basf2 (Belle Analysis Framework 2) is the software framework for the Belle II experiment [89]. It is used for online and offline data processing, from the HLT to physics analysis. The basic structure of the processing chain consists of a linear arrange of modules, being executed in a chain. The data processed by the modules stored in a common storage called DataStore (See Fig. 4.10). Module tasks could be reading and writing of data, analysis, etc.

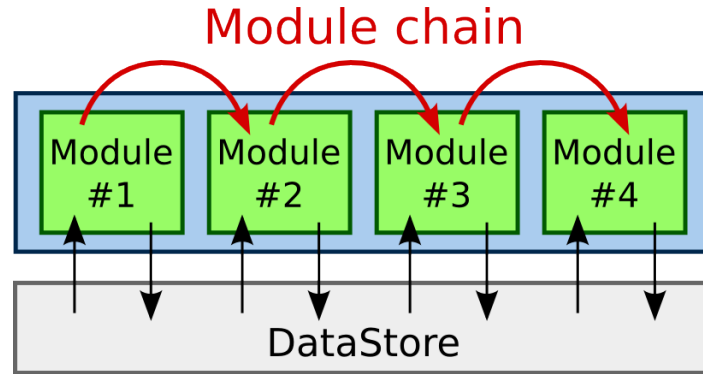


Figure 4.10: Illustration of the Module chain in Basf2 [89]. Each module has communication with a common DataStore.

One of the Basf2 features is the simulation of events in the detector using Monte Carlo (MC) techniques. The simulation starts with at least one event generator that simulates the primary physics process, followed by the simulation of the particles passing each one of the subdetectors. It is possible to include the effects of beam background in the events.

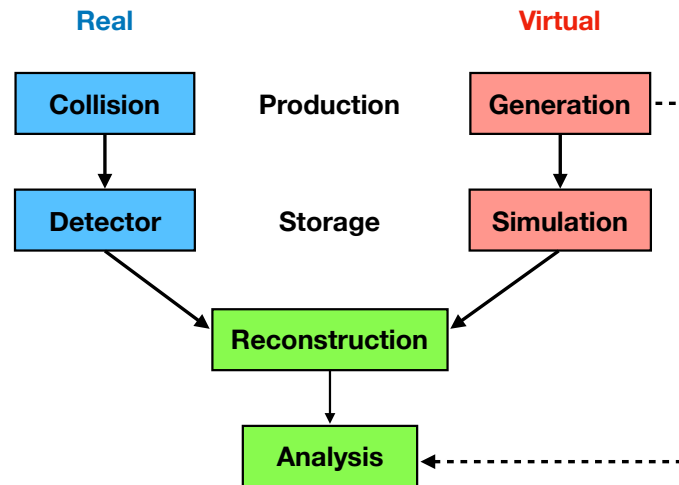


Figure 4.11: Dataflow of events produced in SuperKEKB collisions (left) and simulated using Monte Carlo (right).

Physics process	Cross section [nb]	Generator	Sel. Criteria
$\Upsilon(4S)$	1.11	EvtGen	-
$\tau^+\tau^-$	0.919	KKMC	-
$u\bar{u}$	1.61	KKMC	-
$d\bar{d}$	0.40	KKMC	-
$s\bar{s}$	0.38	KKMC	-
$c\bar{c}$	1.30	KKMC	-
$e^+e^-$	300	BABAYAGA.NLO [94, 95]	$10^\circ < \theta_e < 170^\circ$
$\gamma\gamma$	4.99	BABAYAGA.NLO [94, 95]	$10^\circ < \theta_\gamma < 170^\circ$
$\mu^+\mu^-$	1.148	KKMC	-

Table 4.2: Production cross section of main physics process from collisions of  $e^+e^-$  at  $\sqrt{s} = 10.58$  GeV. The generator of the process at Basf2 is also indicated.

### 4.3.1 Generation

In Basf2, the generation is handled mainly by three groups of generators. To model the decays of B and D mesons, EvtGen [90] simulates exclusive final states and PHYTIA 8 [91] inclusive decays. Production of  $\tau$  pairs is simulated by KKMC [92] and some of the decays are handled by TAUOLA [93]. Continuum production of light quark pairs is managed also by KKMC and PYTHIA. All generators use the same beam energies and vertex position. Cross sections of the main physics processes produced in  $e^+e^-$  collisions at the  $\Upsilon(4S)$  energy are given in table 4.2.

### 4.3.2 Simulation

Geant4 [96] is the software package used by Basf2 to perform a simulation of particles created by the generator passing through materials of the detector. During the simulation, Geant4 transports each primary particle inside the detector, taking into account the trajectory due to

the interaction with the magnetic field (See Fig. 4.12). Secondary particles are also created during the simulation. Digitalization of hit information in the active volume of the subdetectors is handled by separate Basf2 modules. Geant4 uses XML files which contain the geometry of the detector and the materials. Simulation information is stored in the DataStore for the posterior reconstruction of the events.

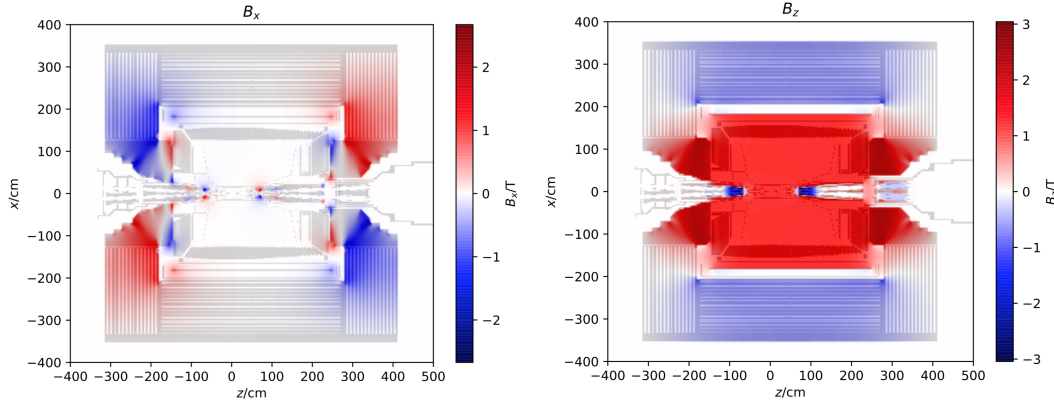


Figure 4.12: The x and z component of the 3D magnetic field map as used in Basf2 release version 02-00-02. Sources of the magnetic field are the 1.5 T detector solenoid and the final focus system (QCS).

In addition to the particles coming from the generator module, the answer of all subdetectors to the presence of beam background can be included. A framework for background overlay has been designed for all detector components, adding measured background events from real collisions to the simulation using digitized hits.

### 4.3.3 Reconstruction and analysis

Given the luminosity provided by SuperKEKB and the high-efficiency triggers, expected data output rate at Belle II is very large. A robust framework for data analysis is required. Data sets will be processed by stage, starting with the raw data being analyzed for the reconstruction of events from information like track hits and calorimeter clusters. MC data obtained from generation and simulation modules can be also reconstructed.



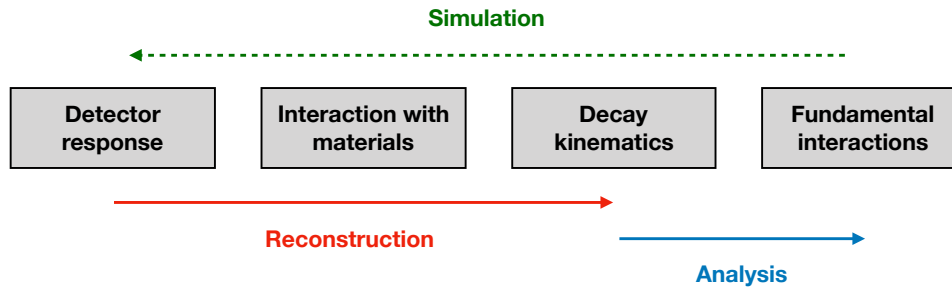


Figure 4.13: Flow of information during reconstruction and analysis. In a simulation, first a decay model is used to determine the kinematics of the primary particles and the detectors response is simulated.

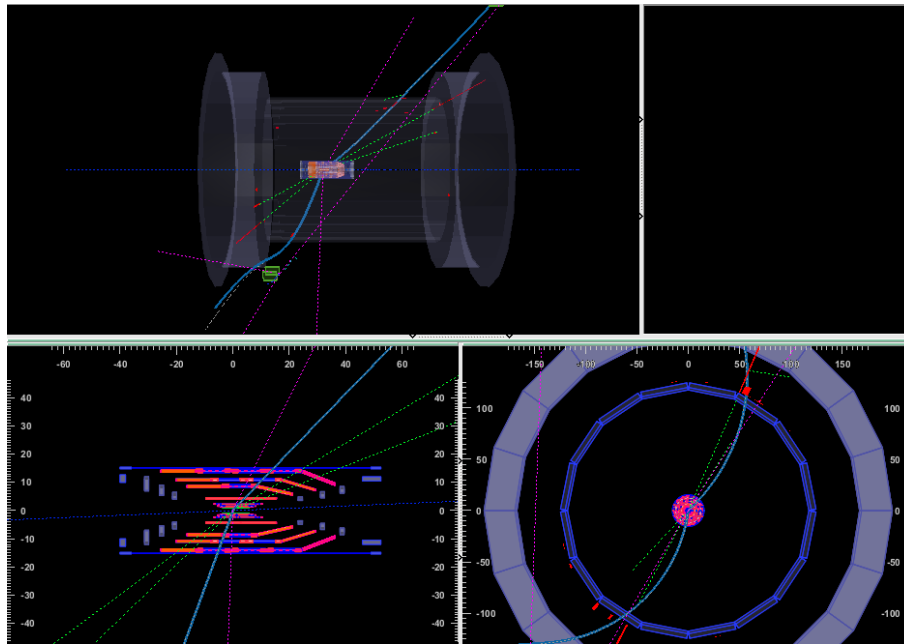


Figure 4.14: Event visualization in ROOT from information obtained in the reconstruction module.

The task of the tracking module is the reconstruction of charged particles. Most of the tracks come from inside the beam pipe, except for the decays of long-lived particles like  $K_S^0$  and  $\Lambda$ . The extrapolation of trajectories allows identification of decay vertices and reconstruction of primary particles using a mass hypothesis in each one of the tracks. Reconstructed

trajectories are also used for the alignment of the detector.

The electromagnetic calorimeter reconstructs the energy and position of depositions from neutral and charged particles. This is basically used for reconstruction of photons and  $\pi^0/\eta$  mesons from the decay  $\pi^0/\eta \rightarrow \gamma\gamma$ , but also aids the electron and charged hadron reconstruction in regions with limited tracking coverage, as the end caps close to the beam pipe. The sum of all reconstructed showers is used to constrain the missing energy in the event.

Particle identification (PID) mechanisms are vital for the reconstruction of events. A proper PID information is required to isolate hadronic final states, reduce backgrounds and allow for flavor identification of primary particles. The TOP and ARICH detectors information, combined with the specific ionization measurements ( $dE/dx$ ) from SVD and CDC are the primary sources of PID for charged particles in Belle II. Likelihood-based selectors are the mechanism provided by PID for analysis. Information from each PID system is analyzed independently, and then a combined likelihood ratio is constructed for each track. Prior probabilities assigned from specific criteria and mass hypothesis, multiplied by the likelihood ratio, allow the construction of a identity probability for a charged track

$$X_{PID} = \frac{\mathcal{L}_X}{\mathcal{L}_e + \mathcal{L}_\mu + \mathcal{L}_\pi + \mathcal{L}_K + \mathcal{L}_p + \mathcal{L}_d}, \quad (4.4)$$

being  $X = (e, \mu, \pi, K, p, d)$ .

## 4.4 Detector Commissioning Phases

The Belle II experiment will start the full physics program in April 2019, recording data during 9 months per year, 20 days per month. The goal of the experiment is getting a full dataset of  $50 \text{ ab}^{-1}$ , which will be used for precision measurements and searches of physics beyond the Standard Model. Given the expected luminosity profile (See Fig. 4.15), it will take until 2020 for Belle II to collect a dataset large enough to equal the one provided by the B-factories of the first generation.

Two previous commissioning periods known as Phase I (Feb - Jun 2016) and Phase II

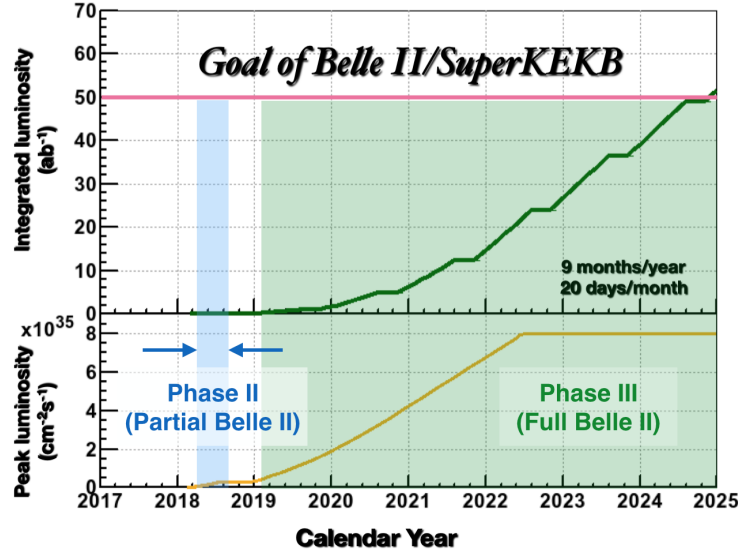


Figure 4.15: Integrated luminosity expected per year for Belle II, provided by SuperKEKB. Phase II, without the vertex system installed, and Phase III with all the sub-detectors are indicated [33].

(Feb - Jul 2018) were performed, where a collection of detectors known as BEAST 2 were deployed for the measurement of background rates and characterization of the environment in which the Belle II inner detectors will operate [84]. During Phase I, the detector solenoid was not active and no collision was performed. In Phase II, all subsystems except the VXD were active and SuperKEKB performed the first collisions on Apr 26. In total,  $500 \text{ pb}^{-1}$  of  $e^+e^-$  collisions at  $\sqrt{s} = 10.58 \text{ GeV}$  were recorded during Phase II.



## Chapter 5

---

# Prospects for $\tau$ Lepton Physics at Belle II

Belle II inherits a successful program of  $\tau$  lepton physics from the previous B-factories. In particular, precision measurements of Standard Model parameters and searches of LFV and LNV decays, benefiting from the large cross-section of the pairwise  $\tau$  lepton production in  $e^+e^-$  collisions are expected. In this chapter, the first results for  $\tau$  lepton physics at Belle II are presented. Additionally, besides the decay channels with an  $\eta$  meson which are the main interest of this work, prospects for  $\tau$  lepton analysis are briefly discussed.

### 5.1 $\tau^+\tau^-$ Production at Belle II

First generation of B-factories, BaBar at SLAC and Belle at KEK, have achieved important results in  $\tau$  lepton physics, taking advantage of the huge amount of  $\tau$  lepton pairs produced in the high luminosity  $e^+e^-$  asymmetric collisions. Recording a combined sample of  $1.5 \text{ ab}^{-1}$ , corresponding to about 1 billion of tau pair decays, precision measurements of the  $\tau$  properties have been performed, such as the mass, lifetime, and branching fractions of leptonic and semileptonic decays. Additionally, limits in electric dipole moment, lepton flavor violation (LFV) and lepton number violation (LNV) decays have been imposed [41]. Figure 5.1 shows some outstanding results obtained in the B-factories, indicating the integrated luminosity and the publication year. Most of these results may be improved in the B-factory

of next generation, Belle II.

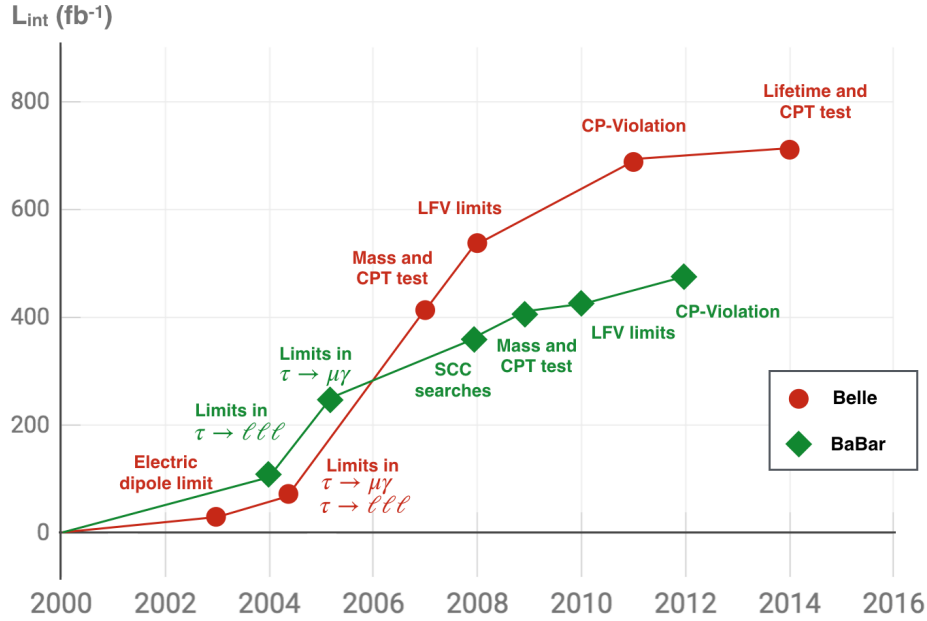


Figure 5.1: Highlights of the  $\tau$  lepton physics results in the first generation of B-factories, indicating the integrated luminosity accumulated.

The data for these first studies was collected with the Belle II detector during the Phase II, in which the inner layers of the silicon-based VXD tracking system were missing. The reprocessed prod5 data from Experiment 3 was used with bad runs excluded in accordance with the official selection, yielding an integrated luminosity of  $492 \text{ pb}^{-1}$ . The analysis is performed using release-02-00-01 and GT425 (data\_reprocessing\_prod5). The official Phase II MC10 productions with beam background simulated were used. Details of MC10 are described at <https://confluence.desy.de/display/BI/Data+Production+MC10>.

The candidate events are selected by requiring only four charged tracks in the event with zero net charge. Each track should have a transverse momentum of  $p_T > 0.1 \text{ GeV}$ , impact parameters of  $|dz| < 5 \text{ cm}$  and  $|dr| < 1.0 \text{ cm}$  and the track should be inside the CDC acceptance region  $-0.8660 < \cos \theta < 0.9565$ . The reconstruction of tau pair production  $e^+e^- \rightarrow \tau^+\tau^-$  is performed searching 3-1 prong events, splitting the decay products in two opposite hemi-

spheres by a plane perpendicular to the thrust axis  $\hat{n}_{thr}$ , defined such that

$$V_{thr} = \sum_i \frac{|\vec{p}_i^{cm} \cdot \hat{n}_{thr}|}{\sum_i |\vec{p}_i^{cm}|}, \quad (5.1)$$

is maximized, with  $\vec{p}_i^{cm}$  being the momentum in the center-of-mass system (CMS) of each charged particle and photon. For  $e^+e^-$  collision data, the thrust magnitude  $V_{thr}$  varies between 0.5 for spherical events and 1 for events with all tracks aligned with  $\hat{n}_{thr}$ . Figure 5.2 represents a  $\tau$  pair reconstruction splitting the event with a plane perpendicular to the thrust axis. Figure 5.3 shows the distribution of the thrust magnitude for Monte Carlo samples of possible contamination sources. In order to suppress the background, a cut of  $V_{thr} > 0.87$  is imposed for event candidates.

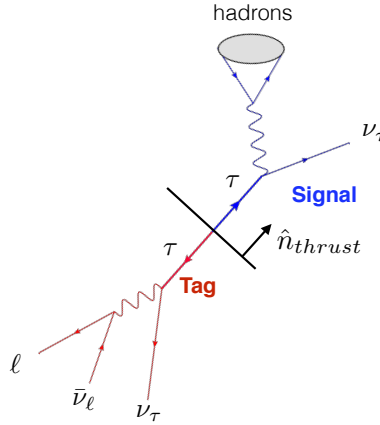


Figure 5.2: Diagram of a  $\tau$  pair event reconstruction in the center-of-mass system. The decay products are divided into two opposite hemispheres, signal and tagging side, by a plane perpendicular to the thrust axis.

Signal side hemisphere is defined as the one containing a 3-prong decay, while the tag side should contain the 1-prong decay. This is achieved using the product between the  $\cos(\theta_{thr})$  of the tag-side track and each of the signal-side tracks. Here,  $\theta_{thr}$  is the angle between the thrust axis and the particle's momentum in CMS. For opposite hemispheres this product should be negative. Figure 5.4 illustrates the separation in hemispheres for the three signal tracks.

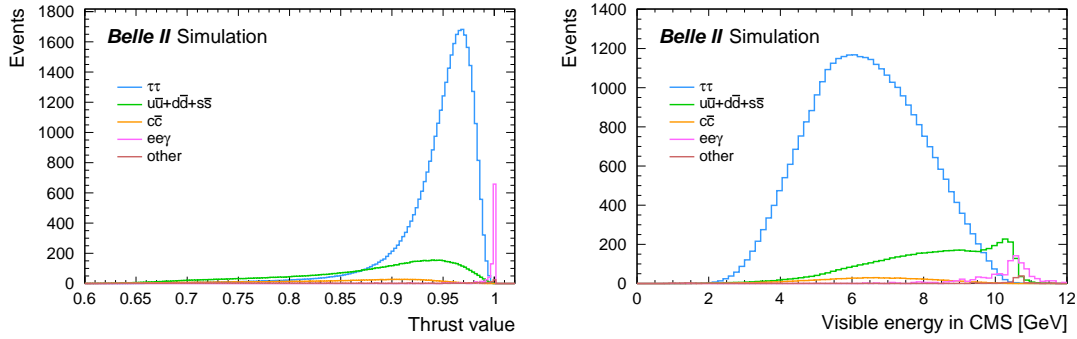


Figure 5.3: The distribution of the thrust value (left) and visible energy (right) in Monte Carlo simulation of Belle II. Monte Carlo samples are rescaled to a luminosity of  $472 \text{ pb}^{-1}$ .

A pion mass hypothesis is used for all charged tracks, looking for  $\tau \rightarrow 3\pi\nu_\tau$  events in the signal side. Due to the deficient PID calibration in prod5, signal side tracks should satisfy the condition  $E/P_{lab} < 0.8$ , where  $E$  is the energy deposit in the ECL and  $P_{lab}$  is the momentum of the particle in laboratory system. This requirement mainly rejects the electrons/positrons from the signal side (See Fig. 5.4).

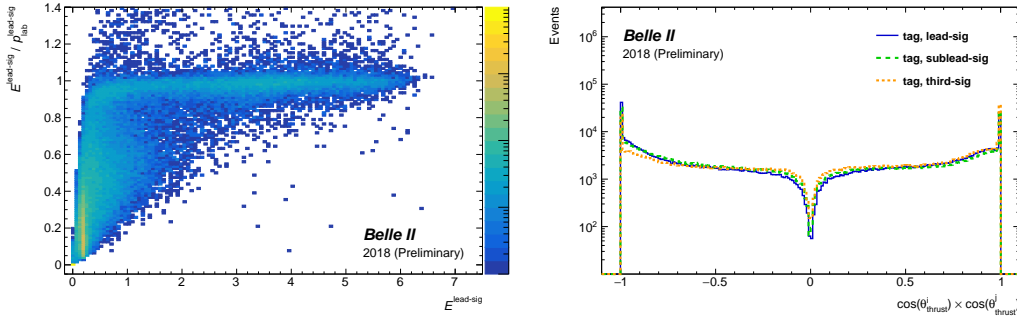


Figure 5.4:  $E/P_{lab}$  vs  $E$  distribution in data for the highest  $p_T$  track on the signal-side (left). Distribution in data of the product between the  $\cos(\theta_{\text{thrust}})$  of the tag-side track and each of the signal-side tracks (right).

The total CMS visible energy of the event can be used to reduce the background contamination using a threshold cut (see Fig. 5.3). The visible energy distribution clearly shows that there are undetected neutrinos in the signal events which shift the distribution towards



smaller values. Further requirements are imposed on the CMS energy of the three hadron system and tag track. Each of these cuts is summarized in Table 5.1. Additionally, a limited number of photons is accepted, allowing at most one (ISR or FSR) photon on the signal side. The following selection applies to them: energy  $E > 200$  MeV, number of weighted crystals in the ECLCluster  $> 1.5$ , energy sums over crystal areas ratio  $E_9/E_{21} > 0.9$  ( $E_9$  means 3x3 crystals area and  $E_{21}$  is 5x5 minus the corners), and the photon should be inside the CDC acceptance region  $-0.8660 < \cos\theta < 0.9565$ .

Kinematic variable	Cut imposed
Thrust value	$> 0.87$
Visible energy in CMS	$< 9.7$ GeV
$E_{\text{signal}}^{\text{CMS}}$	$< 5.29$ GeV
$E_{\text{tag}}^{\text{CMS}}$	$< 5.22$ GeV

Table 5.1: Summary of cuts imposed for for tau-pair event candidates.

So far we have assumed that in data the efficiency for firing at least one L1 trigger is close to 100%. Events in data are required to fire the CDC trigger, with the requirement of at least three two-dimensional tracks at L1. For the prod5 reprocessing, a significant fraction of runs are missing the CDC trigger information. Only  $291 \text{ pb}^{-1}$  of the available  $472 \text{ pb}^{-1}$  remains usable after the trigger requirement.

After selection criteria is applied, 9800 events remains as  $\tau$  pair candidates. Figure 5.5 shows the invariant mass distribution of the three charged pions coming from  $\tau \rightarrow 3\pi\nu_\tau$  candidates, with Monte Carlo (MC) simulated events superimposed. Figure 5.6 presents the event display of the Belle II detector showing one of the event candidates.

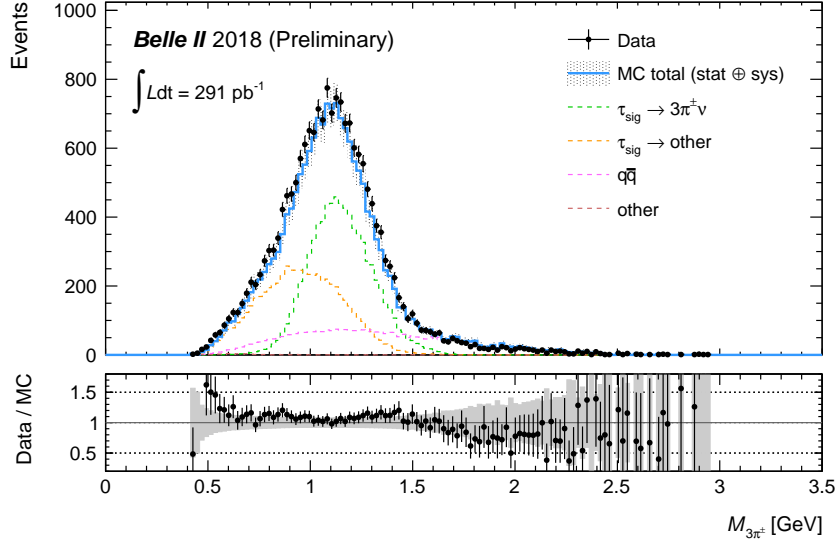


Figure 5.5: Invariant mass distribution of the three pions coming from  $\tau \rightarrow 3\pi\nu_\tau$  candidates reconstructed in Phase II data. Events in data are required to fire the CDC trigger. MC is rescaled to a luminosity of  $291 \text{ pb}^{-1}$  and reweighted according to the trigger efficiency measured in data.

## 5.2 $\tau$ Lepton Mass Measurement

Using the selected events described above, a first  $\tau$  lepton mass measurement at Belle II is performed following the method developed by the ARGUS collaboration with an integrated luminosity of  $341 \text{ pb}^{-1}$  [97]. The pseudomass  $M_{min}$ , defined by

$$M_{min} = \sqrt{M_{3\pi}^2 + 2(E_{beam} - E_{3\pi})(E_{3\pi} - P_{3\pi})}, \quad (5.2)$$

is obtained for each  $\tau \rightarrow 3\pi\nu_\tau$  candidate. Here,  $E_{beam}$  is the energy of one of the beams in CMS and  $M_{3\pi}$ ,  $E_{3\pi}$ ,  $P_{3\pi}$  stand for the invariant mass, the energy and the momentum of the hadronic system of the three pions in CMS, respectively. Figure 5.7 shows the pseudomass distribution with the MC samples superimposed.

An empirical probability density function (p.d.f.) is used to estimate the  $\tau$  lepton mass.

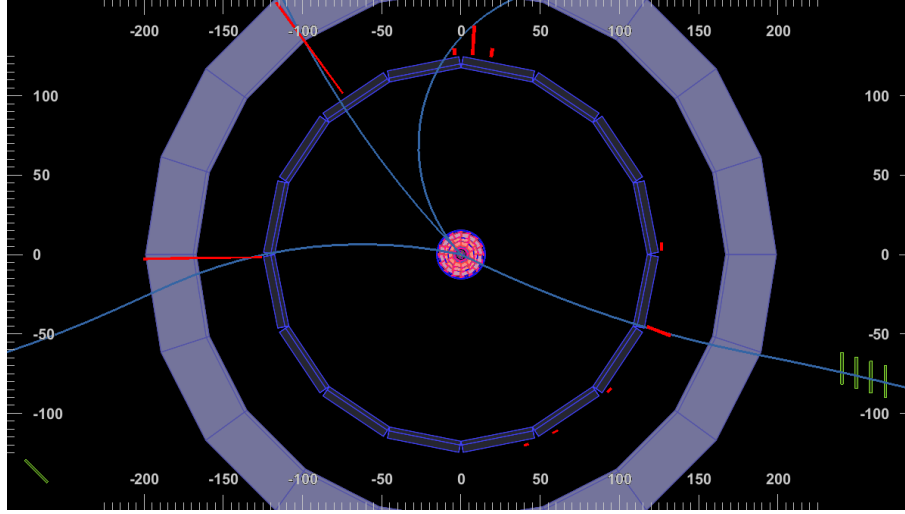


Figure 5.6: Event display of the Belle II detector showing a 3-1 prong event reconstructed in Phase II data. It is likely a  $e^+e^- \rightarrow (\tau_{\text{sig}}^- \rightarrow 3\pi\nu_\tau)(\tau_{\text{tag}}^+ \rightarrow \mu^+\nu_\tau\bar{\nu}_\mu)$  event.

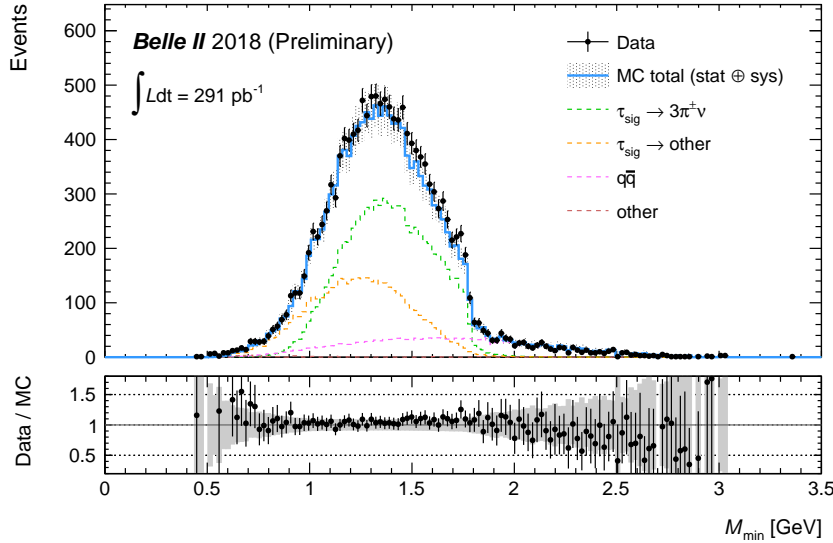


Figure 5.7: Distribution of the pseudomass for the 3-prong decay selected events. Selection criteria is the same as figure 5.5.

The edge p.d.f. used is described by

$$F(M_{\min}; a, b, c, m^*) = (a * M_{\min} + b) \cdot \arctan[(m^* - M_{\min})/c] + P_1(M_{\min}) \quad (5.3)$$

in which  $a, b$  and  $c$  are real values and the parameter  $m^*$  is an estimator of the  $\tau$  lepton mass.

A fit of the p.d.f. (5.3) in the pseudomass region from 1.70 to 1.85 GeV/c<sup>2</sup>, yields  $m^* = (1777.8 \pm 4.8(\text{stat})) \text{ MeV/c}^2$ . To recover the mass  $m_\tau$  from the estimator  $m^*$ , a fit to  $\tau_{\text{sig}}^- \rightarrow 3\pi\nu_\tau$  simulated MC events is performed, in order to take into account effects of reconstruction and selection cuts. The result of the fit to generated events with KKMC/Tauola and simulated using Phase II geometry is  $m^* = 1778.4 \text{ MeV/c}^2$ . In the generator,  $m_\tau$  is set to 1777 MeV/c<sup>2</sup>, which shows a bias in the  $m^*$  estimator of 1.4 MeV/c<sup>2</sup>.

After applying the correction for the estimator, the mass measurement yields [34]

$$m_\tau = (1776.4 \pm 4.8) \text{ MeV/c}^2. \quad (5.4)$$

Figure 5.8 shows the pseudomass distribution of the  $\tau \rightarrow 3\pi\nu$  candidates, with the p.d.f. fitted superimposed.

## 5.3 Prospects for $\tau$ Lepton Physics

As it was mentioned before, Belle II will store 45 billions of  $e^+e^- \rightarrow \tau^+\tau^-$  events, which allows for the study of  $\tau$  physics with high precision measurements. Prospects for the first studies of  $\tau$  lepton physics at the Belle II experiment are briefly described. Further details and a more complete description may be found in the Belle II Physics Book [33].

### 5.3.1 Lepton universality

The Standard Model predicts lepton universality, which means the same value of the coupling  $g_\ell$  between all the leptons and the charged current:  $g_\tau = g_\mu = g_e$ . In principle, there is no reason a priori to expect this. Given (3.1), it is possible to test lepton universality looking at the ratio

$$\frac{\Gamma(\tau \rightarrow e\nu_\tau\bar{\nu}_e(\gamma))}{\Gamma(\mu \rightarrow e\nu_\mu\bar{\nu}_e(\gamma))} = \left(\frac{g_\tau}{g_\mu}\right)^2 \left(\frac{m_\tau}{m_\mu}\right)^5 \frac{f(m_e^2/m_\tau^2)}{f(m_e^2/m_\mu^2)}, \quad (5.5)$$

which constrains  $|g_\tau/g_\mu|$ . In the same way, the ratio  $\Gamma(\tau \rightarrow \mu\nu_\tau\bar{\nu}_\mu(\gamma))/\Gamma(\tau \rightarrow e\nu_\tau\bar{\nu}_e(\gamma))$  constrains  $|g_\mu/g_e|$  and  $\Gamma(\tau \rightarrow \mu\nu_\tau\bar{\nu}_\mu(\gamma))/\Gamma(\mu \rightarrow e\nu_\mu\bar{\nu}_e(\gamma))$  provides information of  $|g_\tau/g_e|$ . Using

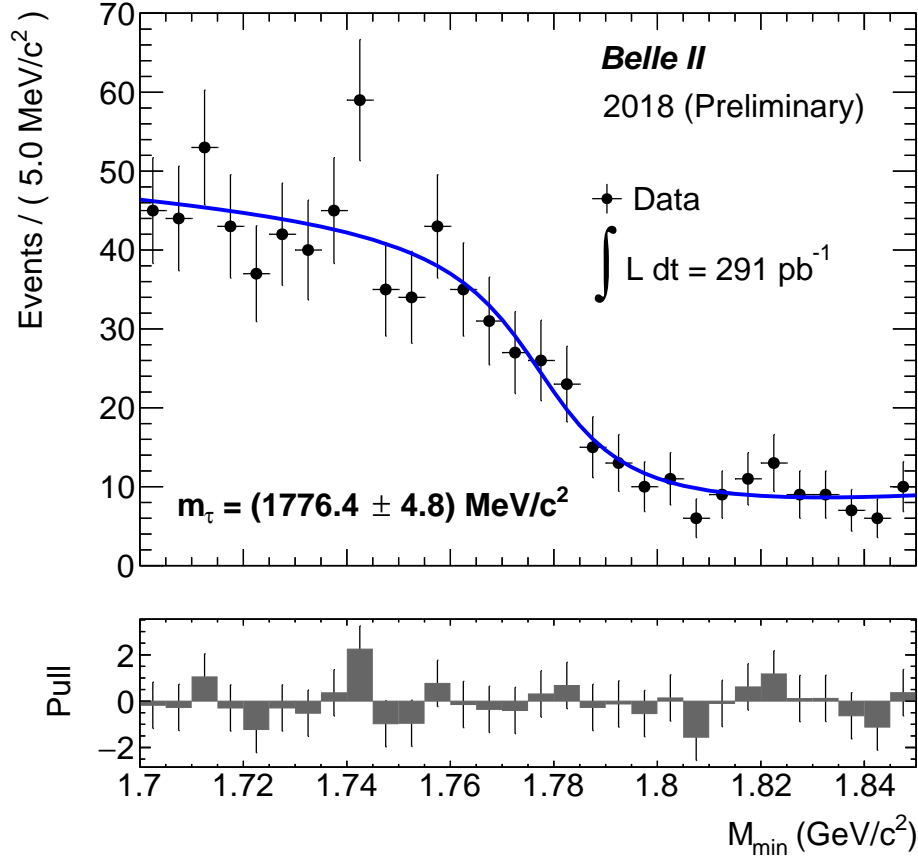


Figure 5.8: Distribution of pseudomass  $M_{\min} = \sqrt{M_{3\pi}^2 + 2(E_{\text{beam}} - E_{3\pi})(E_{3\pi} - P_{3\pi})}$  of  $\tau_{\text{sig}}^- \rightarrow (3\pi)^- \nu_\tau$  candidates reconstructed in Phase II data. Events are required to fire the CDC trigger. The blue line is the result of an unbinned maximum likelihood fit, using an edge function  $(a * M_{\min} + b) \cdot \arctan[(m^* - M_{\min})/c] + P_1(M_{\min})$ , in which  $m^*$  estimates the  $\tau$  lepton mass. A mass of  $m_\tau = (1776.4 \pm 4.8(\text{stat})) \text{ MeV}/c^2$  is measured.

values reported by the PDG [64] and HFLAV [81], the latest experimental results in lepton universality are [98]:

$$\left(\frac{g_\tau}{g_\mu}\right) = 1.0010 \pm 0.0015, \quad \left(\frac{g_\tau}{g_\mu}\right) = 1.0029 \pm 0.0015, \quad \left(\frac{g_\tau}{g_\mu}\right) = 1.0019 \pm 0.0014. \quad (5.6)$$

The precision of the test is limited by the uncertainty of the  $\tau$  lepton mass and leptonic branching fractions. Improvements in the measurement of these quantities will improve directly the

lepton universality tests.

### 5.3.2 Lepton flavor violation (LFV) in $\tau$ decays

The experimental observation of neutrino oscillations teaches two main things: (i) neutrinos are not massless and (ii) lepton flavor is violated. If the Standard Model is extended to include neutrino masses only, the branching ratio of lepton flavor violation (LFV) processes is too small to be observed ( $\sim 10^{-54}$ ) [99, 100]. Therefore, observation of LFV in  $\tau$  decays would be a clear indication of physics beyond Standard Model [101].

At Belle II, the golden channels for studying LFV are  $\tau \rightarrow 3\mu$  and  $\tau \rightarrow \mu\gamma$ . The first one is a purely leptonic state and the background is suppressed in comparison with other channels; the second one has the largest LFV branching fraction in models where the decay is induced by one-loop diagrams with heavy particles [102, 103]. Figure 5.9 shows the prospects for upper limits to be imposed in  $\tau$  LFV decays according to sensitivity studies described at [33] and, for comparison, the limits imposed from previous experiments. With the full dataset expected for the Belle II experiment,  $50 \text{ ab}^{-1}$ , the 90% C.L. upper limit for LFV decays  $\tau$  will be reduced by two orders of magnitude.

### 5.3.3 CP violation in $\tau$ decays

Due to CP violation in the kaon sector, the decay of the  $\tau$  lepton to final states containing a  $K_S^0$  meson will have a nonzero decay-rate asymmetry  $A_\tau$ , defined by

$$A_\tau = \frac{\Gamma(\tau^+ \rightarrow \pi^+ K_S^0 \bar{\nu}_\tau) - \Gamma(\tau^- \rightarrow \pi^- K_S^0 \nu_\tau)}{\Gamma(\tau^+ \rightarrow \pi^+ K_S^0 \bar{\nu}_\tau) + \Gamma(\tau^- \rightarrow \pi^- K_S^0 \nu_\tau)}. \quad (5.7)$$

The SM prediction [104, 105] yields

$$A_\tau^{SM} = (3.6 \pm 0.1) \times 10^{-3}. \quad (5.8)$$

On the other side, BaBar is the only experiment that has measured  $A_\tau$  [106], getting

$$A_\tau^{BaBar} = (-3.6 \pm 2.3 \pm 1.1) \times 10^{-3}, \quad (5.9)$$

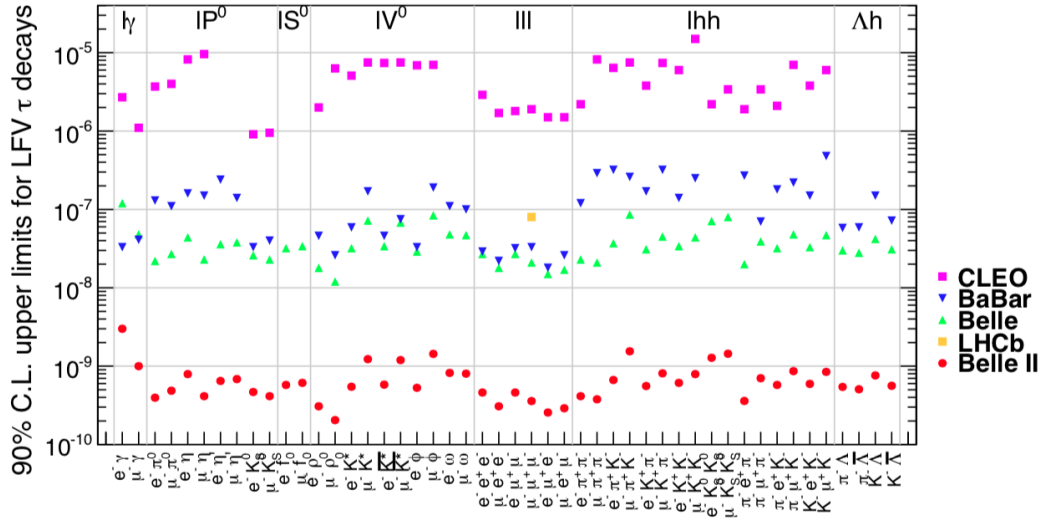


Figure 5.9: Current 90% C.L. upper limits for the branching fraction of LFV  $\tau$  decays imposed by CLEO, BaBar, Belle and LHCb. Prospects for limits to be imposed by Belle II, assuming an integrated luminosity of  $50 \text{ ab}^{-1}$ , are indicated too [33]. Six decay modes also violates lepton number conservation and the last four modes violates baryon number conservation.

which is  $2.8\sigma$  away from the SM prediction (5.8). This result cannot be explained even with models beyond the Standard Model [107]. An improved measurement of  $A_\tau$  will be a priority at Belle II.

CP violation could also arise from a charged scalar boson exchange. It can be detected as a difference in the decay angular distributions. Belle searched for CP violation in angular observables of the decay  $\tau \rightarrow K_S^0 \pi \nu$  [108], in which almost all contributions to systematic uncertainty depend on the control sample statistics. So, it is expected that the uncertainties at Belle II will be improved by a factor of  $\sqrt{70}$ , given the integrated luminosity projected.

### 5.3.4 Michel parameters

Decays such as  $\tau \rightarrow \ell \bar{\nu}_\ell \nu_\tau$  are of especial interest because the absence of strong interactions allows for the precise study of electroweak currents and, in particular, its Lorentz structure. The most general Lorentz invariant Lagrangian, assuming massless and left-handed neutrinos, is [109]

$$\mathcal{L} = \frac{4G_F}{\sqrt{2}} \sum_{\substack{N=S,V,T \\ i,j=L,R}} g_{ij}^N [\bar{\Psi}_i(l) \Gamma^N \Psi_n(\nu_l)] [\bar{\Psi}_m(\nu_\tau) \Gamma_N \Psi_j(\tau)], \quad (5.10)$$

with  $\Gamma^S = 1$ ,  $\Gamma^V = \gamma^\mu$  and  $\Gamma^T = \frac{i}{2\sqrt{2}}(\gamma^\mu \gamma^\nu - \gamma^\nu \gamma^\mu)$ , being  $\gamma^\nu$  the Dirac matrices. The process is then described by ten non-trivial complex coupling constants  $g_{ij}^N$ . In the SM, with a Lorentz structure V-A of the current, the only non-zero coupling is  $g_{LL}^V = 1$ . Additionally, assuming neutrinos are not detected and the spin of the outgoing lepton is unknown, only four bilinear combinations of the coupling constants  $g_{ij}^N$  are experimentally accessible. They are called the Michel parameters  $\rho$ ,  $\eta$ ,  $\xi$  and  $\delta$  [110]. In the SM,  $\rho = 3/4$ ,  $\eta = 0$ ,  $\xi = 1$  and  $\delta = 3/4$ .

The expected statistical uncertainty of Michel parameters at Belle II is of the order of  $10^{-4}$ . Assuming a similar performance as Belle [111], the systematic uncertainties at Belle II will be the dominant ones. Improvements mainly in two-track trigger are needed in order to reduce systematic uncertainties of Michel Parameters. They have also been measured on radiative  $\tau$  decays by Belle [112] and provide complementary information to the non-radiative process.



## Chapter 6

---

### Sensitivity Study of $\tau \rightarrow \eta\pi\pi^0\nu_\tau$ Decays

The decay channel  $\tau^- \rightarrow \eta\pi^-\pi^0\nu_\tau$  is the decay involving  $\eta$  mesons with the highest branching ratio. It is driven by the vector current in the limit of isospin symmetry. Contributions of scalar and pseudoscalar resonances are expected to be negligible by symmetry arguments [113], allowing a precise study of the couplings in the odd-intrinsic parity sector. Additionally, in the limit of the SU(2) isospin symmetry, it is a good cross-check of consistency with the hadronic annihilation  $e^+e^- \rightarrow \eta\pi^+\pi^-$ . Its average branching ratio, reported by the PDG, is  $BR(\tau \rightarrow \eta\pi\pi^0\nu) = (0.138 \pm 0.009)\%$ , obtained from the three available measurements:  $(0.17 \pm 0.02 \pm 0.02)\%$  by CLEO [114],  $(0.18 \pm 0.04 \pm 0.02)\%$  by ALEPH [115] and  $(0.135 \pm 0.003 \pm 0.007)\%$  by Belle [116]. Additionally, Belle is the only experiment that has measured the invariant mass distribution of the  $\pi^-\pi^0$  and  $\eta\pi^-\pi^0$  hadronic systems (See Fig. 6.1). It is important to notice that the  $\eta\pi^-$  distribution has not been measured yet and that the  $\pi^-\pi^0$  disagrees noticeably with the MC simulation.

In this chapter, a sensitivity study of the  $\tau^- \rightarrow \eta\pi^-\pi^0\nu_\tau$  at the Belle II experiment is performed, motivated by the differences observed between the measured branching ratio of the decay, the predicted branching ratio using CVC from the hadronic annihilation  $e^+e^- \rightarrow \eta\pi^+\pi^-$  and their kinematic distributions.

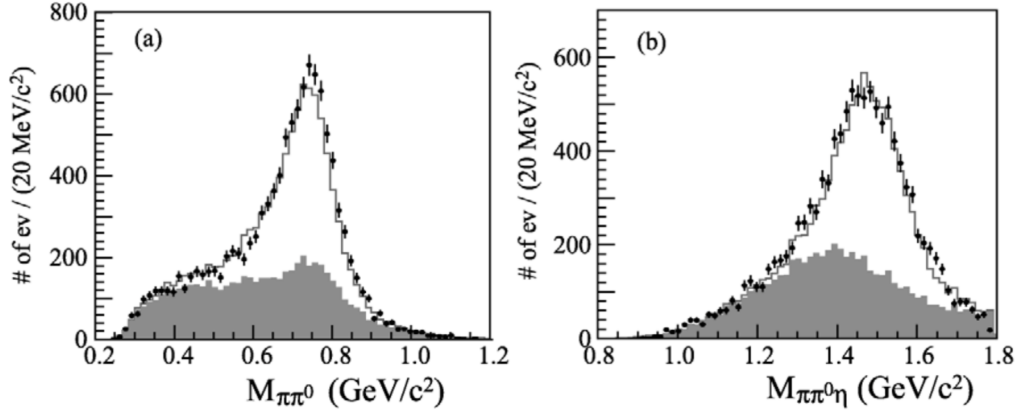


Figure 6.1: Invariant mass distributions of the hadronic systems (a)  $\pi^-\pi^0$  and  $\pi^-\pi^0\eta$  for  $\tau^- \rightarrow \eta\pi^-\pi^0\nu_\tau$  decays reported at [116]. The normal and filled histograms correspond to the signal and background MC distributions, respectively.

## 6.1 $\tau$ Decays and CVC

Given the experimental observation of a universal coupling in all reactions involving the vector part of the charged weak current, the hypothesis of a conserved vector current (CVC) was postulated in the theory of weak interactions [117, 118]. CVC assumes: (i) the isovector part of the electromagnetic current and the vector part of the hadronic weak current are only different components of the same triplet of isospin currents and (ii) the three components of this isospin current are conserved. As a consequence, hadronic currents describing  $\tau$  decays mediated by vector currents and low-energy hadronic  $e^+e^-$  annihilations in  $I = 1$  state are related [119]. Table 6.1 shows the relations between semileptonic  $\tau$  decays and  $e^+e^-$  annihilation via CVC.

CVC does not only relate  $\tau$  branching fractions to the integral over  $e^+e^-$  cross section, but also is possible to obtain distributions and spectral function from both processes and compare them directly. This allows the usage of an independent high-statistics data sample from  $\tau$  decays to increase the accuracy of the spectral functions directly measured in  $e^+e^-$  annihilation. For the vector part of the weak hadronic current in the  $\tau$  decay, the mass distribution

$\Gamma(\tau \rightarrow \text{had } \nu_\tau)$	$\sigma(e^+e^- \rightarrow \text{had})_{I=1}$
$\Gamma(\tau^- \rightarrow \pi^- \pi^0 \nu_\tau)$	$\sigma(e^+e^- \rightarrow \pi^+\pi^-)$
$\Gamma(\tau^- \rightarrow K^- K^0 \nu_\tau)$	$\sigma(e^+e^- \rightarrow K^+K^-)$ and $\sigma(e^+e^- \rightarrow K^0 \bar{K}^0)$
$\Gamma(\tau^- \rightarrow \pi^- \pi^- \pi^+ \pi^0 \nu_\tau)$ and $\Gamma(\tau^- \rightarrow \pi^- 3\pi^0 \nu_\tau)$	$\frac{1}{2}\sigma(e^+e^- \rightarrow \pi^+\pi^-\pi^+\pi^-)$ and $\frac{1}{2}\sigma(e^+e^- \rightarrow \pi^+\pi^-2\pi^0)$
$\Gamma(\tau^- \rightarrow \eta\pi^-\pi^0 \nu_\tau)$	$\sigma(e^+e^- \rightarrow \eta\pi^+\pi^-)$

Table 6.1: Isospin relations between semileptonic  $\tau$  decays and  $e^+e^-$  annihilation into hadrons via CVC.

of the hadronic state is [120]

$$\frac{d\Gamma}{dq^2} = \frac{G_F^2 |V_{ud}|^2 S_{EW}}{32\pi^2 m_\tau^3} (m_\tau^2 - q^2)^2 (m_\tau^2 + 2q^2) v_1(q^2), \quad (6.1)$$

where  $q^2 = s$ ,  $S_{EW}$  is the electroweak correction [72] and the spectral function  $v_1(q^2)$  is given by

$$v_1(q^2) = \frac{q^2}{4\pi\alpha^2} \sigma_{e^+e^-}^{I=1}(q^2). \quad (6.2)$$

The first application of this idea in 1998 was fruitful [121], but the increase of the experimental precision in both  $e^+e^-$  and  $\tau$  data revealed unexpected problems. Generally speaking, spectral functions from  $\tau$  decays to pions are significantly higher than those obtained from  $e^+e^-$  data [122, 123].

## 6.2 The Process $e^+e^- \rightarrow \eta\pi^+\pi^-$ and its Relation to $\tau$ Decays

The production of hadrons in the process  $e^+e^- \rightarrow \eta\pi^+\pi^-$  has a close relation with the decay  $\tau^- \rightarrow \eta\pi^-\pi^0 \nu_\tau$ . Using equation (6.1), the CVC hypothesis and isospin symmetry allow the prediction of the  $\eta\pi^+\pi^-$  mass spectrum and the branching fraction for the  $\tau^- \rightarrow \eta\pi^-\pi^0 \nu_\tau$  decay from data for the  $e^+e^- \rightarrow \eta\pi^+\pi^-$  cross section. A photon radiated from the initial state

allows the study of hadron production over a wide range of  $e^+e^-$  center-of-mass energies in a single experiment. Figure 6.2 shows the measurement of the cross section performed by several collaborations [124, 125, 126, 127], covering the center-of-mass energy range from 1 to 2.5 GeV.

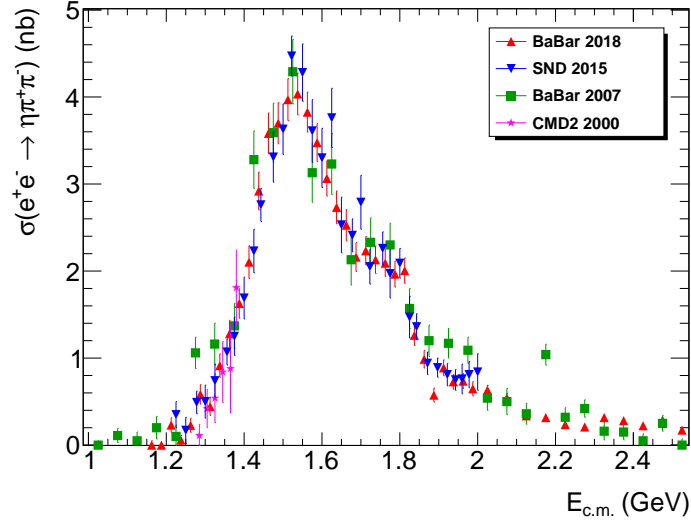


Figure 6.2: The  $e^+e^- \rightarrow \eta\pi^+\pi^-$  cross section measured by the CMD-2, SND and Babar collaborations [124, 125, 126, 127].

Using equation (6.1), cross section distributions of figure 6.2 can be translated to a prediction of the invariant mass distribution in  $\tau^- \rightarrow \eta\pi^-\pi^0\nu_\tau$  decays. Figure 6.3 shows the distribution of  $\sigma(e^+e^- \rightarrow \eta\pi^+\pi^-)$  data translated via CVC to a prediction of the expected shape of the  $\eta\pi^+\pi^0$  invariant mass. For comparison, the distribution measured by Belle (See Fig. 6.1) is overlapped. It is clear there are differences between the  $\eta\pi^-\pi^0$  measured distribution and the predictions from CVC of  $e^+e^-$  data. Distributions of figure 6.3 can be integrated in order to obtain a CVC prediction of the  $\tau^- \rightarrow \eta\pi^-\pi^0\nu_\tau$  branching ratio. Figure 6.4 shows the measured branching ratios and the predictions from  $e^+e^-$  data using CVC. Again, a clear difference between the measurement performed by Belle and the predictions of BaBar and SND is observed. Between the measurement of Belle and the latest Babar's CVC prediction, a difference of  $2.4\sigma$  is observed [116, 127].

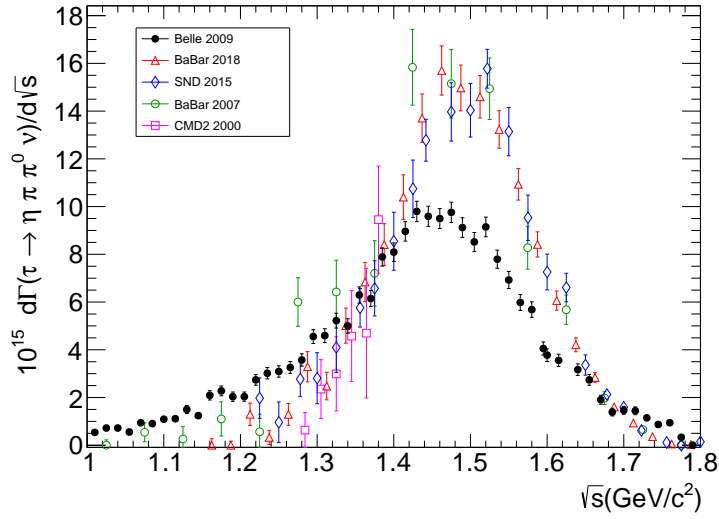


Figure 6.3: Distribution of  $\sigma(e^+e^- \rightarrow \eta\pi^+\pi^-)$  data translated via CVC to a prediction of the expected shape of the  $\eta\pi^+\pi^0$  invariant mass. For comparison, distribution measured by Belle is overlapped.

### 6.3 Sensitivity Study at Belle II

The differences observed in figures 6.3 and 6.4 motivate a high-luminosity measurement of the branching ratio and invariant mass distributions of the decay  $\tau^- \rightarrow \eta\pi^-\pi^0\nu_\tau$ . The Belle II experiment, with its expected high luminosity, will provide the ideal environment for such study. Therefore, a sensitivity study is performed in order to project the capabilities of Belle II in the measurement of  $\tau^- \rightarrow \eta\pi^-\pi^0\nu_\tau$  decays.

The sensitivity analysis is performed using release-02-00-01 of Basf2, with global tag GT\_gen\_prod\_004.10\_release-01-00-00. The MC datasets used for the study were generated and simulated during the official 10th Belle II Monte Carlo campaign (MC10). A simulated data sample equivalent to  $2 \text{ ab}^{-1}$  at Belle II is chosen for the sensitivity analysis. It contains samples of generated  $\tau^+\tau^-$ ,  $q\bar{q}$  and  $B\bar{B}$  pairs with beam background conditions active. Details of MC10 are described at <https://confluence.desy.de/display/BI/Data+Production+MC10>.

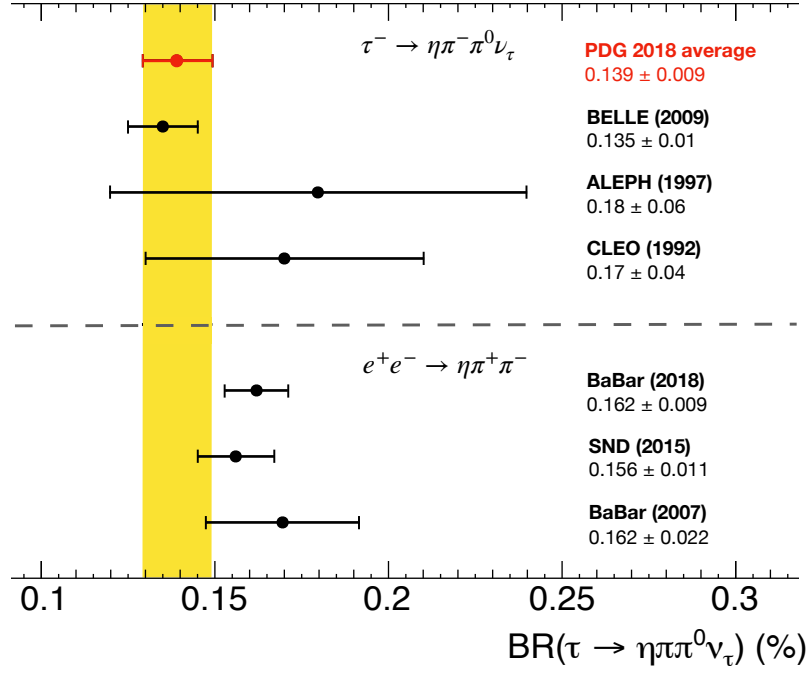


Figure 6.4: On the top, comparison of the branching ratio measurements for the decay  $\tau^- \rightarrow \eta\pi^-\pi^0\nu_\tau$  [114, 115, 116]. On the bottom, predictions for the branching ratio coming from  $e^+e^-$  data, using CVC [125, 126, 127]. The PDG average [35] is represented by the yellow band.

### 6.3.1 Reconstruction of $\tau^- \rightarrow \eta\pi^-\pi^0\nu_\tau$ decays

The selection of events is performed using the 1-1 prong topology. Using the thrust direction the event is divided in two, searching a single track in signal side with a cut in  $\pi_{\text{PID}}$  such that the pion efficiency reconstruction is 95%, and a leptonic decay in tag side (See Fig. 6.5). At this step, an arbitrary number of photons is allowed in signal side. An  $\eta$  and a  $\pi^0$  are reconstructed from  $\gamma\gamma$  candidates, setting an invariant mass of  $(0.4 < M_{\gamma\gamma} < 0.65)\text{GeV}/c^2$  for the  $\eta$  and  $(0.124 < M_{\gamma\gamma} < 0.140)\text{GeV}/c^2$  for  $\pi^0$  candidates. Additionally, a  $\pi^0$ -veto is applied for any photon which comes from an  $\eta$  candidate.

After the initial selection, additional cuts are performed in order to reduce the background. Low-energy photons from both  $\eta \rightarrow \gamma\gamma$  and  $\pi^0 \rightarrow \gamma\gamma$  in endcaps are rejected. It is required

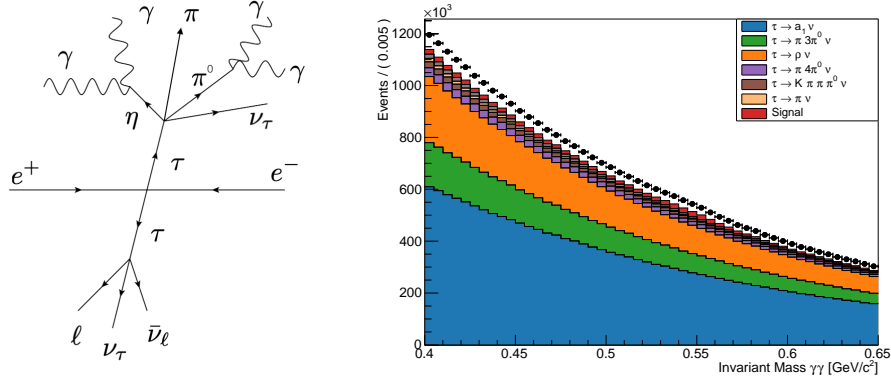


Figure 6.5: Schematic representation of  $e^+e^- \rightarrow (\tau_{sig}^+ \rightarrow \eta\pi^+\nu_\tau)(\tau_{tag}^- \rightarrow \ell\bar{\nu}_\ell\nu_\tau)$  reconstruction, with  $\eta$  and  $\pi^0$  reconstructed from  $\gamma\gamma$  (left). Invariant mass distribution of  $\eta \rightarrow \gamma\gamma$  for MC signal and background events after the 1-1 prong reconstruction (right). In the generation, the branching ratio of the signal reported by the PDG is used.

$E_\gamma > 100$  MeV and  $E_\gamma > 50$  MeV for photons from  $\eta$  and  $\pi^0$ , respectively. Events with low missing momentum,  $P_{miss} < 1$  GeV/c, and missing polar angle  $\theta_{miss}$  close to the endcaps are removed. If the cosine of the angle between  $P_{miss}$  and the thrust direction is larger than 0.7, the event is rejected. The angle between the photons of the  $\eta$  candidates should be lower than 1.5 rad. The transverse momentum of the  $\eta$  and  $\pi^0$  candidates should be larger than 1.2 GeV/c and 0.7 GeV/c, respectively. Finally, a cut in the number of remaining photons is performed, allowing at most 6 photons in the signal side. Details about the kinematic distributions and cuts are located in the Appendix B.

Left side of figure 6.6 shows the invariant mass distribution  $M_{\gamma\gamma}$  for the  $\eta \rightarrow \gamma\gamma$  candidates after the selection cuts described above. The efficiency of the cuts is 99.69% and the remaining number of background events inside the  $\eta$  mass window is 136,308. The signal efficiency has been reduced to 0.72%. In order to count the number of background events below the eta signal peak, a fit is performed in the  $M_{\gamma\gamma}$  distribution using a Crystal Ball (CB) p.d.f. [128], which accounts the energy missed because of the photons escaping of the ECL, plus a second order polynomial to model the signal and background, respectively. Right side

of figure 6.6 shows the fit result, with a CB mean of  $\mu = (545.46 \pm 0.26) \text{ MeV}/c^2$  and a width of  $\sigma = (13.45 \pm 0.27) \text{ MeV}/c^2$ . A mass window of  $\mu \pm 3\sigma$  is defined to count the number of background events below the peak. The result is summarized in table 6.2.

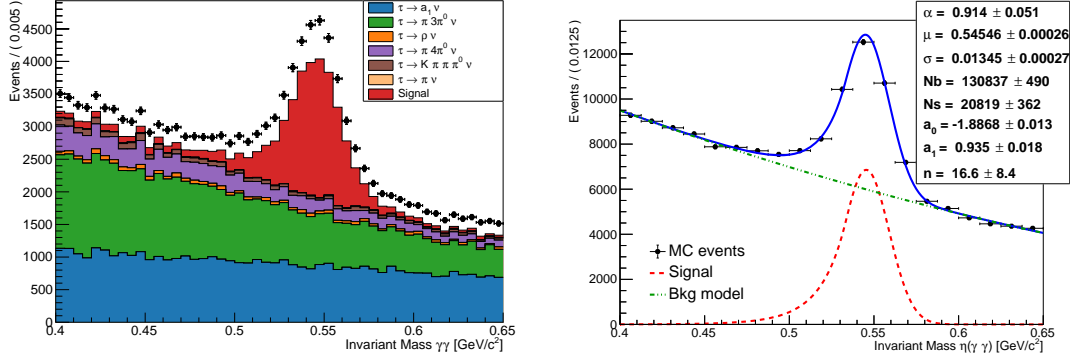


Figure 6.6: Invariant mass distribution  $M_{\gamma\gamma}$  for  $\eta \rightarrow \gamma\gamma$  candidates after the selection cuts described in appendix B (left). Fit performed in the  $M_{\gamma\gamma}$  distribution using a Crystal Ball function [128] plus a second order polynomial to model the signal and background (right).

### 6.3.2 Branching ratio confidence limits

Table 6.2 shows the number of event for each MC sample at  $1 \text{ ab}^{-1}$ . Assuming a linear behavior in the number of events respect to the integrated luminosity and no changes in the signal efficiency, it is possible to estimate the confidence intervals for the branching ratio of the  $\tau^- \rightarrow \eta\pi^-\pi^0\nu_\tau$  decay.

The expected number of signal events is given by

$$N_s = 2 \text{BR}(\tau^- \rightarrow \eta\pi^-\pi^0\nu_\tau) \cdot \mathcal{L}_{\text{int}} \cdot \Lambda, \quad (6.3)$$

where

$$\Lambda = \sigma(e^+e^- \rightarrow \tau^+\tau^-) \cdot \text{BR}(\eta \rightarrow \gamma\gamma) \cdot \varepsilon. \quad (6.4)$$

Using the value reported by the PDG [35],  $\text{BR}(\eta \rightarrow \gamma\gamma) = 39.41\%$ , and from table 6.2 the cross section  $\sigma(e^+e^- \rightarrow \tau^+\tau^-) = 0.919$  and efficiency  $\varepsilon = 0.72\%$ , the maximum and mini-



MC sample	Sig	$\tau^+\tau^-$	$B^+B^-$	$B^0\bar{B}^0$
$\sigma[nb]$	-	0.919	0.565	0.535
Events ( $10^6$ )	1.01	919	565.4	534.6
Efficiency	0.72 %	$2.03 \times 10^{-5}$	$7.07 \times 10^{-9}$	$1.21 \times 10^{-8}$
Evts after cuts	7240	1860	4	6

MC sample	$uu$	$dd$	$ss$	$cc$
$\sigma[nb]$	1.605	0.401	0.383	1.329
Events ( $10^6$ )	1605	401	303	1329
Efficiency	$4.05 \times 10^{-7}$	$8.39 \times 10^{-7}$	$9.41 \times 10^{-7}$	$9.36 \times 10^{-7}$
Evts after cuts	650	336	360	1240

Table 6.2: Estimation of number of events at  $1 \text{ ab}^{-1}$ , based on the cross-section of each process and efficiency for each MC sample. The number of signal events is estimated using equation (6.3).

imum number of expected events,  $N_{max}$  and  $N_{min}$ , can be translated into confidence intervals for the branching ratio

$$\text{BR}(\tau^- \rightarrow \eta \pi^- \pi^0 \nu_\tau)_{(\max, \min)} = \frac{N_{(\max, \min)}}{2\Lambda \cdot \mathcal{L}_{\text{int}}}. \quad (6.5)$$

With the construction of confidence intervals, method developed by Feldman and Cousins [129],  $N_{(\max, \min)} = N_{(\max, \min)}(N_{\text{sig}}, N_{\text{bkg}})$  are obtained, being  $N_{\text{sig}}$  and  $N_{\text{bkg}}$  the number of expected signal and background events according to table 6.2, assuming a linear behavior in the number of events with respect to the integrated luminosity. Figure 6.7 shows the construction of 90% confidence intervals for the branching ratio of  $\tau^- \rightarrow \eta \pi^- \pi^0 \nu_\tau$ , as a function of the integrated luminosity, plus the current average reported by the PDG.

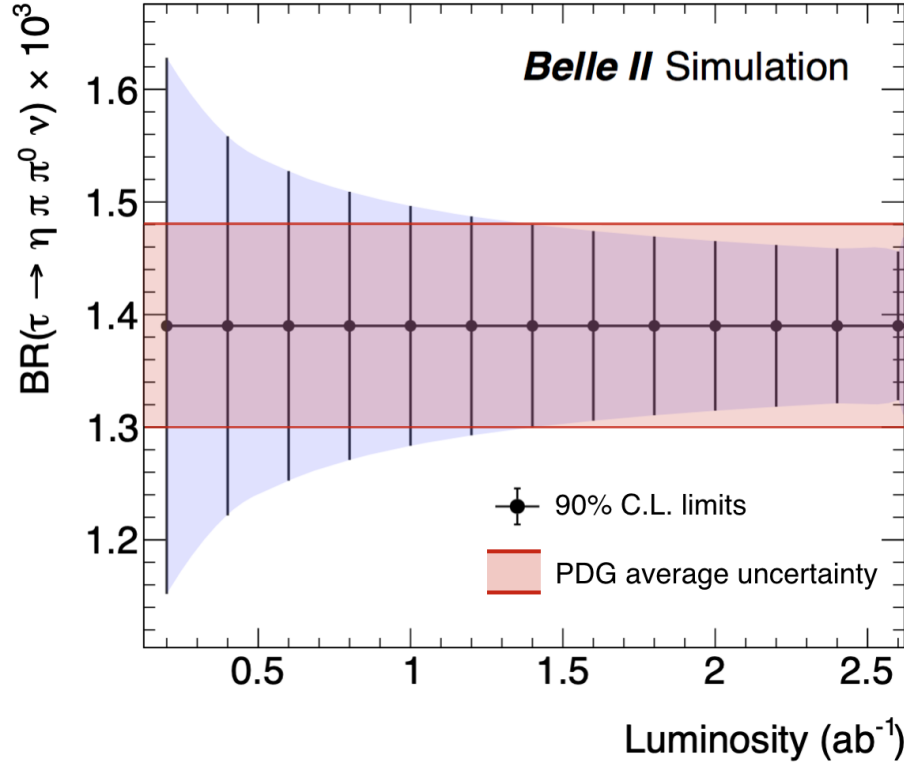


Figure 6.7: 90% confidence intervals for the branching ratio of  $\tau^- \rightarrow \eta \pi \pi^0 \nu_\tau$ , as a function of the integrated luminosity, assuming as central value average reported by PDG. The uncertainty in the PDG average is showed as a red band.

## 6.4 Concluding Remarks

Given the current estimates in the amount of beam background, implemented in the simulations used for this analysis, the experiment Belle II will be capable of reducing the uncertainty in the branching ratio measurement from an integrated luminosity of  $1.3 \text{ ab}^{-1}$  accumulated. However, it is important to mention that the observed beam background amount in Phase II data is higher than the one expected in simulations [84]. For this reason, in the near future, our sensitivity result must be reprocessed using simulated MC samples with twice or more beam background contribution.

---

The measurement will also allow reporting the distribution of the invariant mass of the  $\eta\pi^0\pi$  hadronic system, which is fundamental to confirm or discard the discrepancy with the cross-section distributions of  $e^+e^- \rightarrow \eta\pi^+\pi^-$  measured (See Fig. 6.3).



## Chapter 7

---

# $\tau^- \rightarrow \eta \pi^- \nu_\tau$ : Phenomenological Analysis and Sensitivity Study

In the SM, rare decays are suppressed decay modes originated by approximate symmetries. They provide an ideal environment for new physics searches, mostly because their suppressed amplitudes can be of the same order that effects coming from the contribution of new interactions or particles.

The yet unmeasured  $\tau^- \rightarrow \eta \pi^- \nu_\tau$  decay is predicted in the SM as a suppressed mode, related to isospin-violating processes, with a branching ratio of  $\sim 10^{-5}$ . BSM effects, such as a charged Higgs exchange, can also contribute to the production of the decays. This motivates their study, from a phenomenological point of view, and as sensitivity studies at the Belle II experiment pointing to their discovery and properties measurements. In this chapter, a study of the sensitivity for different observables of these decays, in the framework of an effective field theory, is shown. The potential discovery at the Belle II experiment or constriction of the upper limit on its branching ratio is also presented.

## 7.1 The Decay $\tau \rightarrow \eta \pi \nu_\tau$ and Second Class Currents

The  $G$ -parity [130] is defined by  $G = Ce^{i\pi I_2}$ , with  $C$  the charge conjugation operation and  $I_i$  the components of the isospin rotation operators. Following the classification proposed by Weinberg for strangeness-conserving interaction [131], hadronic weak currents can be classified according to their spin ( $J$ ), parity ( $P$ ) and  $G$ -parity. First class currents must have quantum numbers  $J^{PG} = 0^{++}, 0^{--}, 1^{+-}, 1^{-+}$  and second class currents (SCC) must follow  $J^{PG} = 0^{+-}, 0^{-+}, 1^{++}, 1^{--}$ . The last ones have not been observed yet.

SCC were unsuccessfully searched first in nuclear beta decay processes [132, 133]. Another possibility is their study in  $\tau$  lepton decays, in which the observation of the decay  $\tau^- \rightarrow b_1^- \nu_\tau$  or  $\tau^- \rightarrow a_0^- \nu_\tau$  have been proposed as a clear signature of SCC [134]. The most feasible possibility is the search of SCC via the decay  $\tau \rightarrow \eta \pi \nu$ , containing or not an intermediate  $a_0$  resonance. This proposed decay would be forbidden if  $G$ -parity were an exact symmetry of the SM, because the  $G$ -parity of the  $\pi^- \eta$  system is -1, which is opposed to the vector current that drives the decay in the SM. However, since isospin is only a partial symmetry of strong interactions,  $G$ -parity gets broken by the difference between mass and electric charge of the  $u$  and  $d$  quarks, allowing the decay of the  $\tau$  lepton into a pion, an  $\eta$  meson and the corresponding tau neutrino. The spin-parity  $J^P$  of the  $\pi^- \eta$  system is  $0^+$  or  $1^-$ , depending on whether the system is in  $S$ - or  $P$ -wave respectively, which gives  $J^{PG} = 0^{+-} (1^{--})$ . Therefore, the decay can be realized through a SCC.

Historically,  $\tau^- \rightarrow \eta \pi^- \nu_\tau$  decays attracted a lot of attention at the end of the eighties, when measurements of final states with an  $\eta$  meson hinted abnormally large branching fractions. In 1987 the HRS collaboration reported the observation of  $\tau^- \rightarrow \eta \pi^- \nu_\tau$  with a branching ratio of  $\sim 5\%$ , which is against theoretical expectations [135]. With the time, the situation settled and these decays have remained unobserved.

In the SM,  $\tau \rightarrow \eta \pi \nu_\tau$  is suppressed by isospin violation through the  $\pi^0 - \eta$  mixing (See Fig. 7.1) and a branching ratio of  $\text{BR}(\tau \rightarrow \eta \pi \nu_\tau) \sim 10^{-5}$  is expected [136, 137, 138, 37, 139]. Table 7.1 shows the most recent predictions of the branching ratio for this decay, in which

several models have been used.

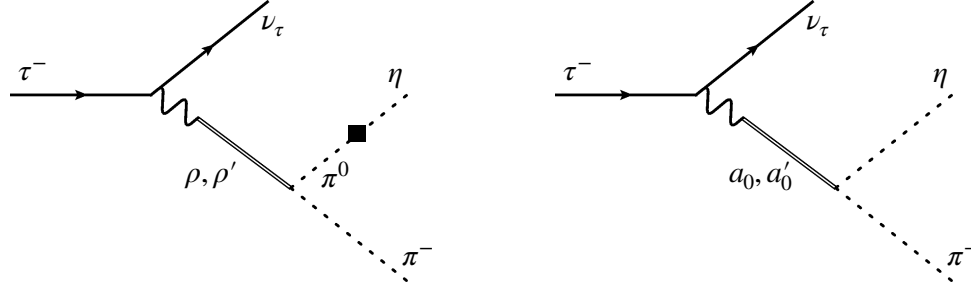


Figure 7.1: Production of  $\tau \rightarrow \eta\pi\nu_\tau$  in the SM through isospin violation, via  $\pi^0 - \eta$  mixing (left) and coupling of the vector current to a scalar  $a_0$  resonance (right).

The current experimental limits for the branching ratio of  $\tau^- \rightarrow \eta\pi^-\nu_\tau$  are:

$$\begin{aligned} \text{BR}(\tau^- \rightarrow \eta\pi^-\nu_\tau) &< 9.9 \times 10^{-5}, \text{ 95\% CL (BaBar [140])}, \\ \text{BR}(\tau^- \rightarrow \eta\pi^-\nu_\tau) &< 7.3 \times 10^{-5}, \text{ 90\% CL (Belle [141])}, \\ \text{BR}(\tau^- \rightarrow \eta\pi^-\nu_\tau) &< 1.4 \times 10^{-4}, \text{ 95\% CL (CLEO [142])}, \end{aligned} \quad (7.1)$$

which lie close to the SM estimates (See Table 7.1). This decay channel has not been observed yet, given the difficulty in controlling the background.

Model	$\text{BR}_V (\times 10^5)$	$\text{BR}_S (\times 10^5)$	$\text{BR}_{V+S} (\times 10^5)$	Reference
MDM, 1 resonance	0.36	1.0	1.36	[136]
MDM, 1 and 2 resonances	[0.2, 0.6]	[0.2, 2.3]	[0.4, 2.9]	[137]
Nambu-Jona-Lasinio	0.44	0.04	0.48	[138]
Anality, Unitarity	0.13	0.2	0.33	[37]
3 coupled channels	0.26	1.41	1.67	[139]

Table 7.1: Most recent SM predictions of the branching ratio for the decay  $\tau \rightarrow \eta\pi\nu_\tau$ . The main difference arises from the predictions used for the scalar form factor contribution.

## 7.2 Effective-field Theory Study of $\tau^- \rightarrow \eta \pi^- \nu_\tau$

The suppression of  $\tau^- \rightarrow \eta \pi^- \nu_\tau$  in the SM makes interesting this decay to study the effects of genuine SCC not induced by isospin breaking effects, such as the ones induced by the exchange of charged Higgs [23, 143] or leptoquark bosons [144] (See Fig. 7.2).

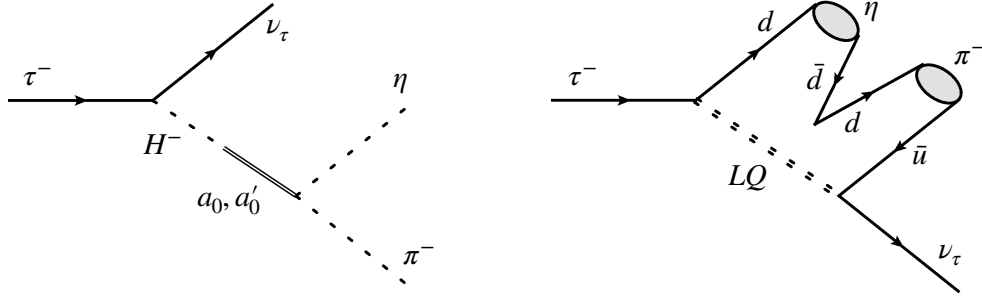


Figure 7.2: Production of  $\tau \rightarrow \eta \pi \nu_\tau$  not induced by isospin breaking within the SM, via the coupling of a charged Higgs to a scalar resonance (left) and the exchange of a leptoquark (right).

The decay  $\tau^- \rightarrow \eta \pi^- \nu_\tau$  can be studied in the framework of an effective Lagrangian, where the effects of physics beyond the SM are encoded in the most general Lagrangian involving dimension-six operators. Our study exhibits different sensitivities to the various effective couplings [38].

The effective Lagrangian with  $SU(2)_L \otimes U(1)$  invariant dimension six operators can be written as [145, 146]

$$\mathcal{L}^{(\text{eff})} = \mathcal{L}_{\text{SM}} + \frac{1}{\Lambda^2} \sum_i \alpha_i O_i \longrightarrow \mathcal{L}_{\text{SM}} + \frac{1}{v^2} \sum_i \hat{\alpha}_i O_i, \quad (7.2)$$

being  $\hat{\alpha}_i = (v^2/\Lambda^2)\alpha_i$  the dimensionless new physics couplings, which are  $O(10^{-3})$  for an scale  $\Lambda \sim 1$  TeV. The low-scale  $O(1 \text{ GeV})$  effective Lagrangian for hadronic Cabibbo-allowed and lepton-flavor conserving transitions involving only left-handed neutrino fields



is given by

$$\begin{aligned} \mathcal{L}_{CC} = & \frac{-4G_F}{\sqrt{2}} V_{ud} \left[ \left( 1 + [v_L]_{\ell\ell} \right) \bar{\ell}_L \gamma_\mu \nu_{\ell L} \bar{u}_L \gamma^\mu d_L + [v_R]_{\ell\ell} \bar{\ell}_L \gamma_\mu \nu_{\ell L} \bar{u}_R \gamma^\mu d_R \right. \\ & + [s_L]_{\ell\ell} \bar{\ell}_R \nu_{\ell L} \bar{u}_R d_L + [s_R]_{\ell\ell} \bar{\ell}_R \nu_{\ell L} \bar{u}_L d_R \\ & \left. + [t_L]_{\ell\ell} \bar{\ell}_R \sigma_{\mu\nu} \nu_{\ell L} \bar{u}_R \sigma^{\mu\nu} d_L \right] + \text{h.c.}, \end{aligned} \quad (7.3)$$

where subscripts  $L$  and  $R$  refer to left-handed and right-handed chiral projections respectively,  $\ell = (e, \mu, \tau)$ ,  $G_F$  is the tree-level definition of the Fermi constant and  $\sigma^{\mu\nu} \equiv i[\gamma^\mu, \gamma^\nu]/2$ . The case  $v_L = v_R = s_L = s_R = t_L = 0$  gives the SM Lagrangian.

In terms of equivalent effective couplings,  $\varepsilon_{L,R} = v_{L,R}$ ,  $\varepsilon_S = s_L + s_R$ ,  $\varepsilon_P = s_L - s_R$  and  $\varepsilon_T = t_L$ , the effective Lagrangian particularized for  $\ell = \tau$  is

$$\begin{aligned} \mathcal{L}_{CC} = & -\frac{G_F V_{ud}}{\sqrt{2}} \left( 1 + \varepsilon_L + \varepsilon_R \right) \left[ \bar{\tau} \gamma_\mu (1 - \gamma_5) \nu_\tau \cdot \bar{u} \left[ \gamma^\mu - (1 - 2\hat{\varepsilon}_R) \gamma^\mu \gamma_5 \right] d \right. \\ & \left. + \bar{\tau} (1 - \gamma_5) \nu_\tau \cdot \bar{u} \left[ \hat{\varepsilon}_S - \hat{\varepsilon}_P \gamma_5 \right] d + 2\hat{\varepsilon}_T \bar{\tau} \sigma_{\mu\nu} (1 - \gamma_5) \nu_\tau \cdot \bar{u} \sigma^{\mu\nu} d \right] + \text{h.c.}, \end{aligned}$$

where  $\hat{\varepsilon}_i \equiv \varepsilon_i / (1 + \varepsilon_L + \varepsilon_R)$  for  $i = R, S, P, T$ .

### 7.2.1 Hadronic $\tau$ decay amplitude

Given the parity of the pseudoscalar mesons, only the vector, scalar and tensor currents can contribute to the amplitude of the decay  $\tau^-(p) \rightarrow \eta(p_\eta) \pi^-(p_\pi) \nu_\tau(p')$ , which reads

$$\mathcal{M} = \frac{G_F V_{ud} \sqrt{S_{EW}}}{\sqrt{2}} (1 + \varepsilon_L + \varepsilon_R) \left[ L_\mu H^\mu + \hat{\varepsilon}_S L H + 2\hat{\varepsilon}_T L_{\mu\nu} H^{\mu\nu} \right], \quad (7.4)$$

where the leptonic currents are given by

$$\begin{aligned} L_\mu &= \bar{u}(p') \gamma_\mu (1 - \gamma_5) u(p), \\ L &= \bar{u}(p') (1 + \gamma_5) u(p), \\ L_{\mu\nu} &= \bar{u}(p') \sigma_{\mu\nu} (1 + \gamma_5) u(p), \end{aligned} \quad (7.5)$$

and the vector, scalar and tensor hadronic matrix elements are defined as

$$H^\mu = \langle \eta\pi^- | \bar{d}\gamma^\mu u | 0 \rangle = c_V Q^\mu F_+(s) + c_S \frac{\Delta_{K^0 K^+}^{QCD}}{s} q^\mu F_0(s), \quad (7.6)$$

$$H = \langle \eta\pi^- | \bar{d}u | 0 \rangle = F_S(s), \quad (7.7)$$

$$H^{\mu\nu} = \langle \eta\pi^- | \bar{d}\sigma^{\mu\nu} u | 0 \rangle = iF_T(s)(p_\eta^\mu p_\pi^\nu - p_\pi^\mu p_\eta^\nu), \quad (7.8)$$

in which,  $q^\mu = (p_\eta + p_\pi)^\mu$ ,  $Q^\mu = (p_\eta - p_\pi)^\mu + (\Delta_{\pi^- \eta}/s)q^\mu$ ,  $s = q^2$  and  $\Delta_{ij} \equiv m_i^2 - m_j^2$ ,  $\Delta_{K^0 K^+}^{QCD} = m_{K^0}^2 - m_{K^+}^2 + m_{\pi^+}^2 - m_{\pi^0}^2$ . The constants  $c_S = \sqrt{\frac{2}{3}}$ ,  $c_V = \sqrt{2}$ , denote Clebsch-Gordan flavor coefficients. The divergence of the vector current relates the  $F_S(s)$  and  $F_0(s)$  form factors [38]

$$F_S(s) = c_S \frac{\Delta_{K^0 K^+}^{QCD}}{(m_d - m_u)} F_0(s). \quad (7.9)$$

Thus,  $F_S(s)$  inherits the strong isospin suppression of  $F_0(s)$ . In consequence, the scalar contribution of (7.7) can be absorbed into the vector current through the Dirac equation  $L = L_\mu q^\mu / M_\tau$  and (7.9) replacing

$$c_S \frac{\Delta_{K^0 K^+}^{QCD}}{s} \longrightarrow c_S \frac{\Delta_{K^0 K^+}^{QCD}}{s} \left[ 1 + \frac{s \hat{\mathcal{E}}_S}{m_\tau(m_d - m_u)} \right], \quad (7.10)$$

in the second term of (7.6). The hadronization of the tensor current is discussed with detail in references [38] and [39], getting a conservative estimate of  $|F_T^{\pi\eta}| \leq 0.094 \text{ GeV}^{-1}$ .

### 7.2.2 Dalitz plots

The characterization of hadronic dynamics and search for new physics in the decay  $\tau^- \rightarrow \eta\pi^- \nu_\tau$  requires the use of detailed observables beyond the branching ratio, as the hadronic spectrum and angular distributions or Dalitz plot analyses.

In the rest frame of the  $\tau$  lepton, the differential width for the  $\tau^- \rightarrow \pi^- \eta \nu_\tau$  decay is given by

$$\frac{d^2\Gamma}{dsdt} = \frac{1}{32(2\pi)^3 M_\tau^3} |\overline{\mathcal{M}}|^2, \quad (7.11)$$

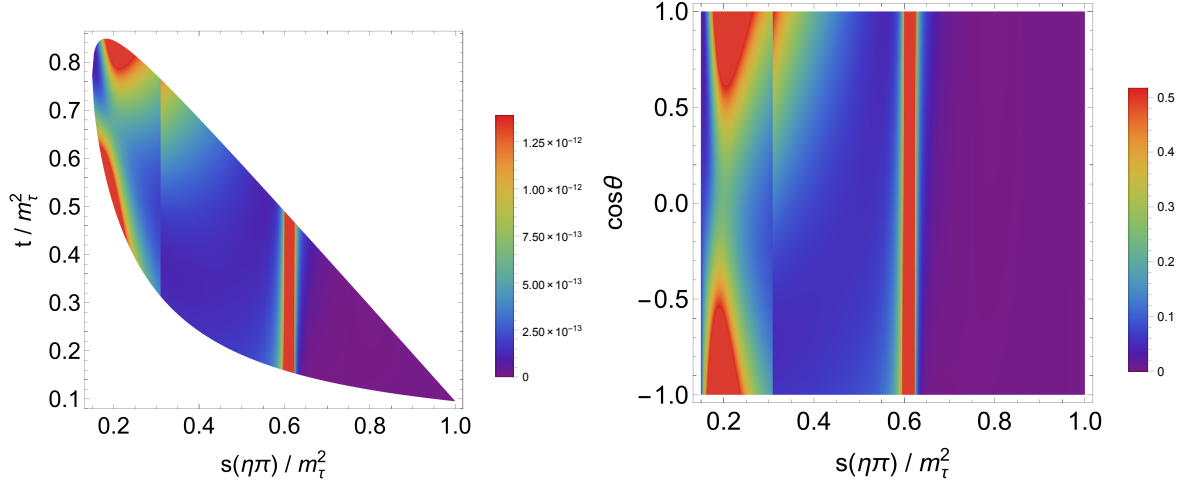


Figure 7.3: Left: Dalitz plot distributions  $|\overline{\mathcal{M}}|^2_{00}$  in the SM, according to eq. (7.13). Right: Double differential decay distribution in the  $(s, \cos\theta)$  variables according to eq. (7.15) normalized to the tau width, for both decay channels. The Mandelstam variables,  $s$  and  $t$ , are normalized to  $M_\tau^2$ .

where  $|\overline{\mathcal{M}}|^2$  is the unpolarized spin-averaged squared matrix element,  $s$  is the invariant mass of the  $\eta\pi^-$  system and  $t = (p' + p_\eta)^2 = (p - p_{\pi^-})^2$ . The kinematic limits for  $s$  are  $(m_\eta + m_\pi)^2 \leq s \leq M_\tau^2$ , meanwhile  $t$  takes the values  $t^-(s) \leq t \leq t^+(s)$ , with

$$t^\pm(s) = \frac{1}{2s} \left[ 2s(M_\tau^2 + m_\eta^2 - s) - (M_\tau^2 - s)(s + m_\pi^2 - m_\eta^2) \pm (M_\tau^2 - s) \sqrt{\lambda(s, m_\pi^2, m_\eta^2)} \right], \quad (7.12)$$

where the Kallen function is defined as  $\lambda(x, y, z) = x^2 + y^2 + z^2 - 2xy - 2xz - 2yz$ .

The unpolarized spin-averaged squared amplitude in the presence of New Physics interactions is given by

$$|\overline{\mathcal{M}}|^2 = \frac{G_F^2 |V_{ud}|^2 S_{EW}}{s^2} (1 + \epsilon_L + \epsilon_R)^2 (M_{0+} + M_{T+} + M_{T0} + M_{00} + M_{++} + M_{TT}) \quad (7.13)$$

where  $M_{00}$ ,  $M_{++}$  and  $M_{TT}$  originate from the scalar, vector and tensor contributions to the amplitude respectively, and  $M_{0+}$ ,  $M_{T+}$ ,  $M_{T0}$  are their corresponding interference terms. Their

expressions are

$$\begin{aligned}
M_{0+} &= 2c_V c_S m_\tau^2 \times \text{Re}[F_+(s)F_0^*(s)]\Delta_{K^0 K^+}^{QCD} \left(1 + \frac{\widehat{\epsilon}_S s}{m_\tau(m_d - m_u)}\right) \\
&\quad \times \left(s(m_\tau^2 - s + \Sigma_{\pi\eta^{(\prime)}}) - 2t\right) + m_\tau^2 \Delta_{\pi\eta^{(\prime)}} \Big, \\
M_{T+} &= -4c_V \widehat{\epsilon}_T m_\tau^3 s \text{Re}[F_T(s)F_+^*(s)] \left(1 - \frac{s}{m_\tau^2}\right) \lambda(s, m_\pi^2, m_{\eta^{(\prime)}}^2), \\
M_{T0} &= -4c_S \Delta_{K^0 K^+}^{QCD} \widehat{\epsilon}_T m_\tau s \text{Re}[F_T(s)F_0^*(s)] \left(1 + \frac{\widehat{\epsilon}_S s}{m_\tau(m_d - m_u)}\right) \\
&\quad \times \left(s(m_\tau^2 - s - 2t + \Sigma_{\pi\eta^{(\prime)}}) + m_\tau^2 \Delta_{\pi\eta^{(\prime)}}\right), \\
M_{00} &= c_S^2 (\Delta_{K^0 K^+}^{QCD})^2 m_\tau^4 \left(1 - \frac{s}{m_\tau^2}\right) |F_0(s)|^2 \left(1 + \frac{\widehat{\epsilon}_S s}{m_\tau(m_d - m_u)}\right)^2, \\
M_{++} &= c_V^2 |F_+(s)|^2 \left[ m_\tau^4 (s + \Delta_{\pi\eta^{(\prime)}})^2 - m_\tau^2 s \left(2\Delta_{\pi\eta^{(\prime)}}(s + 2t - 2m_\pi^2) + \Delta_{\pi\eta^{(\prime)}}^2 + s(s + 4t)\right) \right. \\
&\quad \left. + 4m_{\eta^{(\prime)}}^2 s^2 (m_\pi^2 - t) + 4s^2 t (s + t - m_\pi^2) \right], \\
M_{TT} &= 4\widehat{\epsilon}_T^2 F_T^2(s) s^2 \left[ m_{\eta^{(\prime)}}^4 (m_\tau^2 - s) - 2m_{\eta^{(\prime)}}^2 (m_\tau^2 - s)(s + 2t - m_\pi^2) - m_\pi^4 (3m_\tau^2 + s) \right. \\
&\quad \left. + 2m_\pi^2 ((s + m_\tau^2)(s + 2t) - 2m_\tau^4) - s((s + 2t)^2 - m_\tau^2(s + 4t)) \right], \tag{7.14}
\end{aligned}$$

where  $\Delta_{\pi\eta} = m_{\pi^-}^2 - m_\eta^2$  and  $\Sigma_{\pi\eta} = m_{\pi^-}^2 + m_\eta^2$  are defined. In the distribution of Dalitz plots, new physics effects can be enhanced for large values of the hadronic invariant mass, according to Eq. (7.10). Left side of figure 7.3 shows the square of the matrix element  $|\overline{\mathcal{M}}|_{00}^2$  obtained using the SM prediction for  $\tau^- \rightarrow \pi^- \eta \nu_\tau$  form factors [139, 147]. The dynamics is mainly driven by the dynamically generated scalar resonance with mass  $\sim 1.39$  GeV, followed by two populated spots corresponding to the effects of the vector form factor, around the  $\rho(770)$  peak.

Angular distributions of decay products are also modified by the effects of new physics. In order to analyze these contributions, it becomes convenient to set in the rest frame of the hadronic system, defined by  $\vec{p}_\pi + \vec{p}_\eta = \vec{p}_\tau = \vec{p}_{\nu_\tau} = 0$ . In this frame, the pion and tau lepton energies are given by  $E_\tau = (s + M_\tau^2)/2\sqrt{s}$  and  $E_\pi = (s + m_\pi^2 - m_\eta^2)/2\sqrt{s}$ . The angle  $\theta$  between the three-momenta of the pion and tau lepton is related to the invariant  $t$  variable by  $t = m_\tau^2 + m_\pi^2 - 2E_\tau E_\pi + 2|\vec{p}_\pi||\vec{p}_\tau|\cos\theta$ , where  $|\vec{p}_\pi| = \sqrt{E_\pi^2 - m_\pi^2}$  and  $|\vec{p}_\tau| = \sqrt{E_\tau^2 - m_\tau^2}$ . Then, the decay distribution in the  $(s, \cos\theta)$  variables in the framework of the most general

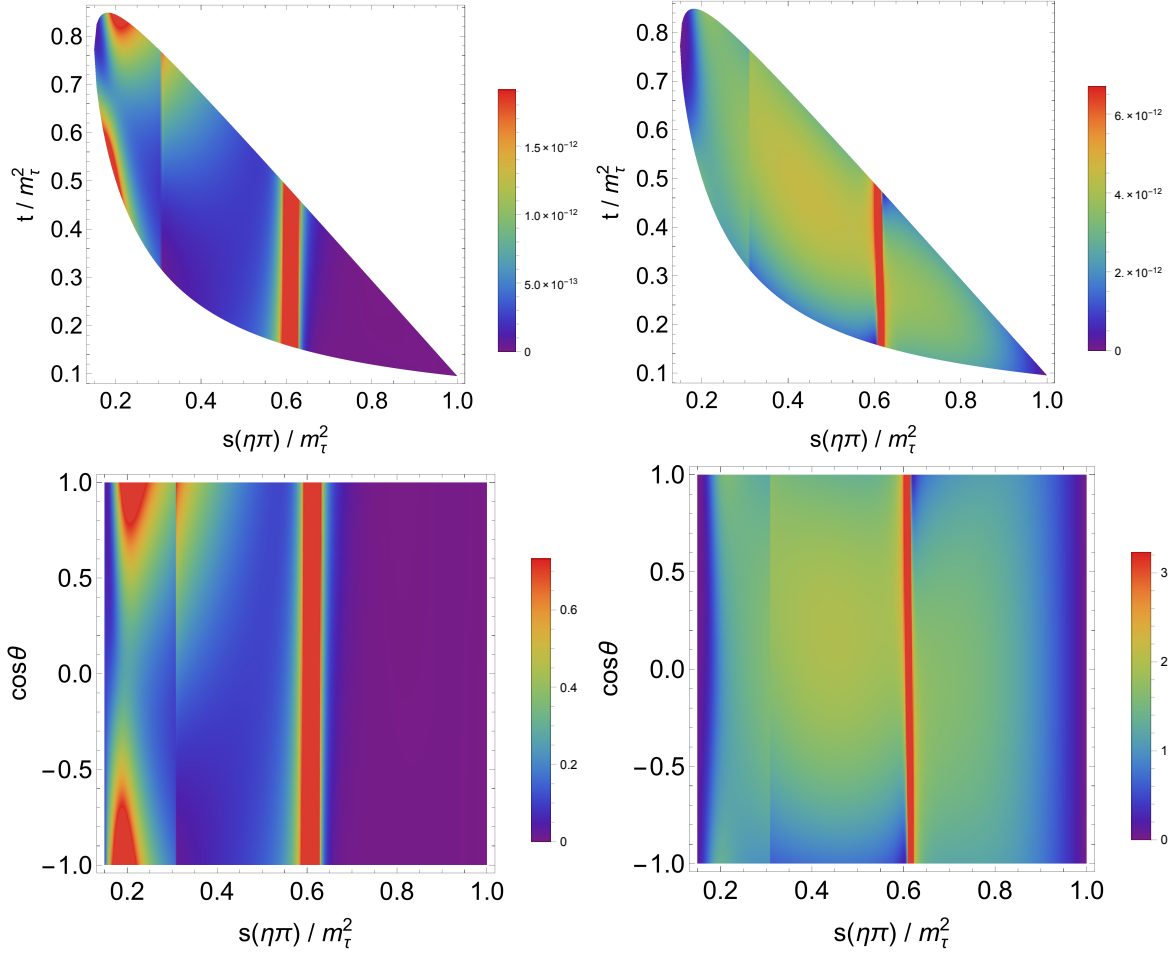


Figure 7.4: Dalitz plot distribution for  $\tau^- \rightarrow \pi^- \eta \nu_\tau$  decays: left-hand side corresponds to  $(\hat{\epsilon}_S = 0.002, \hat{\epsilon}_T = 0)$ , while the figures in the right-hand side are obtained with the choice  $(\hat{\epsilon}_S = 0, \hat{\epsilon}_T = 0.3)$ . The figures in the first row correspond to eq. (7.13). Figures in the lower row corresponding to eq. (7.15), are normalized to  $\Gamma_\tau$ . The Mandelstam variables,  $s$  and  $t$ , are normalized to  $M_\tau^2$ .

effective interactions is given by

$$\begin{aligned}
 \frac{d^2\Gamma}{d\sqrt{s}d\cos\theta} = & \frac{G_F^2 |V_{ud}|^2 S_{EW}}{128\pi^3 m_\tau} (1 + \epsilon_L + \epsilon_R)^2 \left( \frac{m_\tau^2}{s} - 1 \right)^2 |\vec{p}_\pi| \left\{ (c_S \Delta_{K^0 K^+}^{\text{QCD}})^2 |F_0^{\pi^- \eta}(s)|^2 \right. \\
 & \times \left( 1 + \frac{s \hat{\epsilon}_S}{m_\tau(m_d - m_u)} \right)^2 + 16 |\vec{p}_\pi|^2 s^2 \left| \frac{c_V}{2m_\tau} F_+^{\pi^- \eta}(s) - \hat{\epsilon}_T F_T \right|^2 \\
 & + 4 |\vec{p}_\pi|^2 s \left( 1 - \frac{s}{m_\tau^2} \right) \left[ c_V^2 |F_+^{\pi^- \eta}(s)|^2 + 4 \hat{\epsilon}_T F_T^2 \right] \cos^2 \theta + 4 c_S \Delta_{K^0 K^+}^{\text{QCD}} |\vec{p}_\pi| \sqrt{s} \cos \theta \\
 & \left. \times \left( 1 + \frac{s \hat{\epsilon}_S}{m_\tau(m_d - m_u)} \right) \left[ c_V \text{Re}[F_0(s) F_+^*(s)] - 2 \frac{s}{m_\tau} \hat{\epsilon}_T F_T \text{Re}[F_0(s)] \right] \right\}. \quad (7.15)
 \end{aligned}$$

The usual SM expressions for this observable [148] are recovered when  $\widehat{\epsilon}_S$  and  $\widehat{\epsilon}_T$  are equal to zero. Results obtained using eq.(7.15) are plotted in the right side of figure 7.3.

The squared matrix element  $|\overline{\mathcal{M}}|^2$ , for two representative values of the set of  $(\widehat{\epsilon}_S, \widehat{\epsilon}_T)$ , is shown in the first row of figure 7.4. The values of  $(\widehat{\epsilon}_S, \widehat{\epsilon}_T)$  are consistent with current upper limits on the  $\text{BR}(\tau^- \rightarrow \pi^- \eta \nu_\tau)$ . In the second row,  $(s, \cos \theta)$  distributions are plotted. A comparison of the plots in figure 7.3 and figures 7.4 show that the Dalitz plot distribution is sensitive to the effects of tensor interactions but rather insensitive to the scalar interactions.

### 7.2.3 Decay rates

Using finiteness of the matrix element at the origin and the fact that the form factors are normalized at the origin [139], it is shown that

$$F_+^{\pi^- \eta}(0) = -\frac{c_{\pi^- \eta}^S}{c_{\pi^- \eta}^V} \frac{\Delta_{K^0 K^+}^{\text{QCD}}}{\Delta_{\pi^- \eta}} F_0^{\pi^- \eta}(0), \quad (7.16)$$

and

$$\widetilde{F}_{+,0}^{\pi^- \eta}(s) = \frac{F_{+,0}^{\pi^- \eta}(s)}{F_{+,0}^{\pi^- \eta}(0)}. \quad (7.17)$$

Then, integration upon the  $t$  variable in eq. (7.11) gives the hadronic invariant mass distributions

$$\begin{aligned} \frac{d\Gamma}{ds} = & \frac{G_F^2 S_{EW} m_\tau^3 |V_{ud} F_+^{\pi^- \eta}(0)|^2}{384 \pi^3 s} (1 + \epsilon_L + \epsilon_R)^2 \left(1 - \frac{s}{m_\tau^2}\right)^2 \lambda^{1/2}(s, m_\eta^2, m_\pi^2) \\ & \times [X_{VA} + \widehat{\epsilon}_S X_S + \widehat{\epsilon}_T X_T + \widehat{\epsilon}_S^2 X_{S^2} + \widehat{\epsilon}_T^2 X_{T^2}], \end{aligned} \quad (7.18)$$

where

$$\begin{aligned}
X_{VA} &= \frac{1}{s^2} \left[ 3 |\tilde{F}_0^{\pi^- \eta}(s)|^2 \Delta_{\pi^- \eta}^2 + |\tilde{F}_+^{\pi^- \eta}(s)|^2 \lambda(s, m_\eta^2, m_\pi^2) \left( 1 + \frac{2s}{m_\tau^2} \right) \right], \\
X_S &= \frac{6}{s m_\tau} |\tilde{F}_0^{\pi^- \eta}(s)|^2 \frac{\Delta_{\pi^- \eta}^2}{m_d - m_u}, \\
X_T &= \frac{-6\sqrt{2} \operatorname{Re}[F_+(s)] F_T}{s m_\tau |F_+^{\pi^- \eta}(0)|^2} \lambda(s, m_\eta^2, m_\pi^2), \\
X_{S^2} &= \frac{3}{m_\tau^2} |\tilde{F}_0^{\pi^- \eta}(s)|^2 \frac{\Delta_{\pi^- \eta}^2}{(m_d - m_u)^2}, \\
X_{T^2} &= \frac{4}{s} \frac{|F_T|^2}{|F_+(0)|^2} \left( 1 + \frac{s}{2m_\tau^2} \right) \lambda(s, m_\eta^2, m_\pi^2).
\end{aligned} \tag{7.19}$$

When  $\varepsilon_L = \varepsilon_R = \varepsilon_S = \varepsilon_T = 0$  the SM result from [139] is recovered. Figure 7.5 shows the invariant mass distribution of the hadronic system for  $\tau^- \rightarrow \pi^- \eta \nu_\tau$  decays. Noticeable differences respect to the SM result are observed outside the resonance peak region  $M_S \sim 1.39$  GeV.

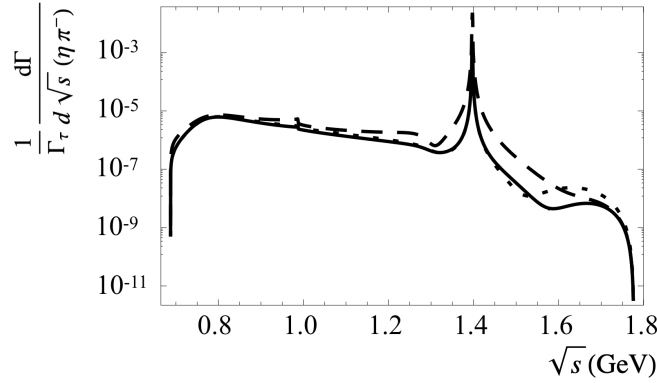


Figure 7.5:  $\eta \pi^-$  hadronic invariant mass distribution for the SM (solid line) and  $\hat{\varepsilon}_S = 0.004, \hat{\varepsilon}_T = 0$  (dashed line),  $\hat{\varepsilon}_S = 0, \hat{\varepsilon}_T = 0.6$  (dotted line) [38]. Units in axis are given in powers of GeV and the decay distributions are normalized to the tau decay width.

The total decay rate of the  $\tau \rightarrow \eta \pi \nu_\tau$  decay can be obtained integrating equation (7.18). This will depend on several effective couplings, inducing scalar and tensor interactions, and

new physics effects can be constrained measuring the branching ratio. The decay rate  $\Gamma$  can be compared with  $\Gamma_0$ , being the last one the decay rate neglecting  $\hat{\epsilon}_S$  and  $\hat{\epsilon}_T$  couplings

$$\Delta \equiv \frac{\Gamma - \Gamma_0}{\Gamma_0} = \alpha \hat{\epsilon}_S + \beta \hat{\epsilon}_T + \gamma \hat{\epsilon}_S^2 + \delta \hat{\epsilon}_T^2. \quad (7.20)$$

It is clear  $\Delta = 0$  corresponds to the SM case, with genuine vector interaction and induced scalar interaction only. The numerical values of the coefficients are:  $\alpha \sim 7 \cdot 10^2$ ,  $\beta \sim 1.1$ ,  $\gamma \sim 1.6 \cdot 10^5$  and  $\delta \sim 21$  [38]. Equation (7.20) is a quadratic function of the effective scalar and tensor couplings, in consequence it can be used to explore the sensitivity of  $\tau^- \rightarrow \pi^- \eta \nu_\tau$  decays to the effects of new physics. Figure 7.6 shows experimental upper limits on  $\Delta$ , represented as horizontal lines, and equation (7.20) plotted as function of  $\hat{\epsilon}_S$  and  $\hat{\epsilon}_T$  couplings. We get the constraint  $-0.008 \leq \hat{\epsilon}_S \leq 0.004$  which corresponds to the BaBar's upper limit on the branching fraction assuming  $\hat{\epsilon}_T = 0$ . Constraints on tensor interactions are weaker:  $|\hat{\epsilon}_T| \leq 0.4$ , assuming  $\hat{\epsilon}_S = 0$  and BaBar's upper limit. Systematic theory errors are neglected in this study.

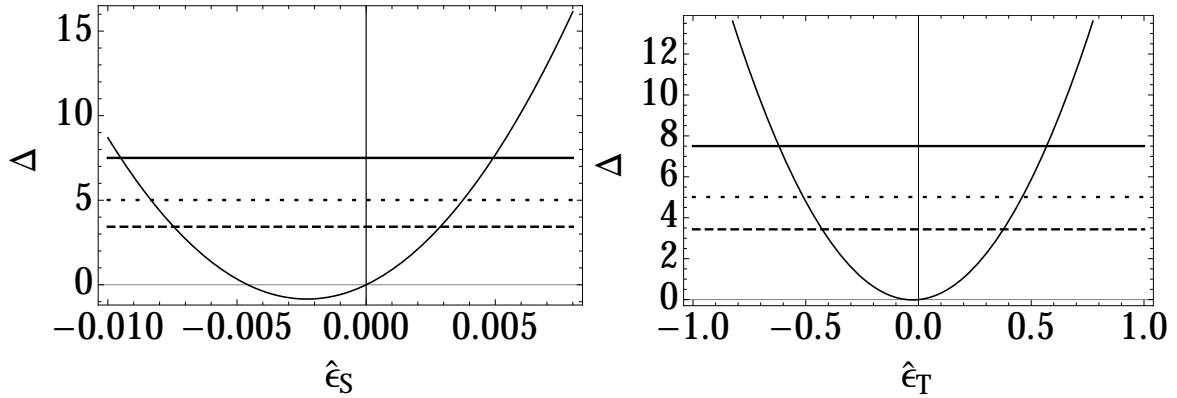


Figure 7.6:  $\Delta$  as a function of  $\hat{\epsilon}_S$  (for  $\hat{\epsilon}_T = 0$ ) and  $\hat{\epsilon}_T$  (for  $\hat{\epsilon}_S = 0$ ) for  $\tau^- \rightarrow \pi^- \eta \nu_\tau$  decays [38]. Horizontal lines represent current values of  $\Delta$  according to the upper limits on the branching fraction obtained by Babar (dotted line),  $< 9.9 \times 10^{-5}$ , 95% CL [140], Belle (dashed line),  $< 7.3 \times 10^{-5}$ , 90% CL [141] and CLEO (solid line),  $< 1.4 \times 10^{-4}$ , 95% CL [142].

Constraints on scalar and tensor interactions can be set simultaneously from a comparison of experimental upper limits and equation (7.20), as shown in figure 7.7. These constraints



can be improved at Belle II, where we compare the limits that can be set on the  $(\hat{\epsilon}_S, \hat{\epsilon}_T)$  plane by assuming that the branching ratio of  $\tau^- \rightarrow \pi^- \eta \nu_\tau$  can be measured with a 50% and 20% accuracy.

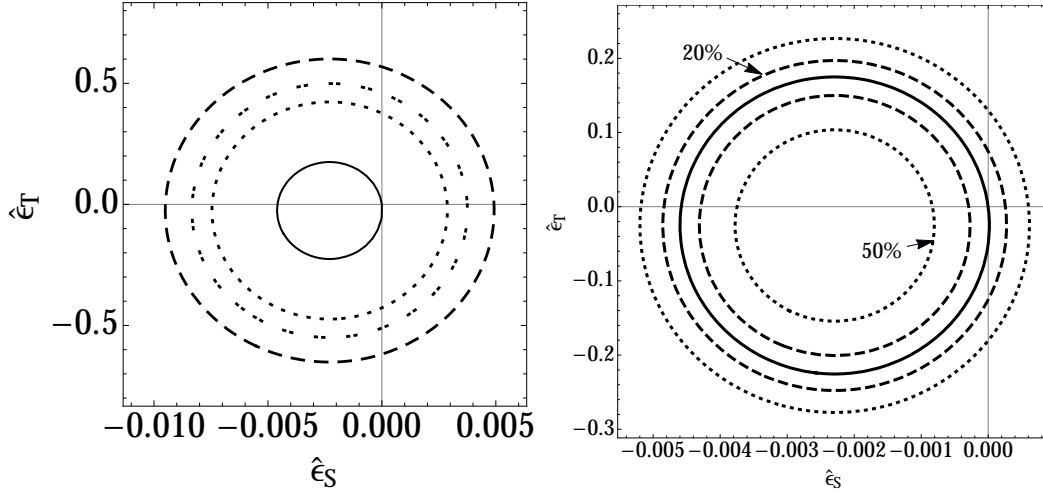


Figure 7.7: Left figure shows constraints on scalar and tensor couplings obtained from  $\Delta(\tau^- \rightarrow \eta \pi^- \nu_\tau)$  values using current experimental upper limits on branching fractions [38]. The solid line represents  $\Delta = 0$ , the dotted line is the Belle 90%CL limit, the double dotted line is the BaBar 95%CL limit and the dashed line is the CLEO 95%CL limit. In the right side, the thick solid line in the middle shows the contour for the SM Branching Ratio of  $\tau^- \rightarrow \pi^- \eta \nu_\tau$ . In the hypothetical case of this value being measured by Belle-II with 50%(band bounded with dotted lines) and 20%(band bounded with dashed lines) precision, some nonzero allowed range of values for  $\hat{\epsilon}_S, \hat{\epsilon}_T$  can be determined.

Constraints on the scalar and tensor couplings that can be derived from the current upper limits (7.1) are summarized in table 7.2. Constraints that can be obtained from measurements of the branching fraction of these decays at Belle II are also shown, assuming a 20% accuracy in the measurement.

$\Delta$	$\widehat{\epsilon}_S(\widehat{\epsilon}_T = 0)$	$\widehat{\epsilon}_T(\widehat{\epsilon}_S = 0)$	$\widehat{\epsilon}_S$	$\widehat{\epsilon}_T$
Babar	$[-8.3, 3.9] \cdot 10^{-3}$	$[-0.43, 0.39]$	$[-0.83, 0.37] \cdot 10^{-2}$	$[-0.55, 0.50]$
Belle	$[-7.7, 2.9] \cdot 10^{-3}$	$[-0.51, 0.47]$	$[-0.75, 0.29] \cdot 10^{-2}$	$[-0.48, 0.43]$
CLEO	$[-9.5, 5.0] \cdot 10^{-3}$	$[-0.62, 0.57]$	$[-0.95, 0.49] \cdot 10^{-2}$	$[-0.66, 0.60]$
Belle II	$([-4.8, 2.0] \cdot 10^{-3})$	$[-0.12, 0.08]$	$[-4.9, -4.3] \cdot 10^{-3} \cup$ $[-2.6, 3.0] \cdot 10^{-4}$	$[-0.20, -0.25] \cup$ $[0.15, 0.20]$

Table 7.2: Constraints on the scalar and tensor couplings obtained from current upper limits (7.1) and hypothetical measurements with 20% accuracy at Belle II.

### 7.3 Sensitivity study of $\tau^- \rightarrow \eta\pi^- \nu_\tau$ decays

In analogy with the sensitivity study of the channel  $\tau^- \rightarrow \eta\pi^- \pi^0 \nu_\tau$  described in the previous chapter, the strategy to follow is the simulation, reconstruction and counting of signal and background events in the distribution of  $\eta$  candidates. However, for this case,  $\eta$  is reconstructed using the channels  $\eta \rightarrow \gamma\gamma$  and  $\eta \rightarrow \pi^+ \pi^- \pi^0$ , which correspond to 1-1 prong and 3-1 prong topologies, using a leptonic decay as a tagging:

$$e^+ e^- \rightarrow (\tau_{\text{sig}}^+ \rightarrow \eta\pi^+ \nu_\tau)(\tau_{\text{tag}}^- \rightarrow \ell \bar{\nu}_\ell \nu_\tau), \quad (7.21)$$

with

$$\begin{aligned} \eta &\rightarrow \gamma\gamma && (1\text{-}1 \text{ prong}), \\ \eta &\rightarrow \pi^+ \pi^- \pi^0 && (3\text{-}1 \text{ prong}). \end{aligned} \quad (7.22)$$

Figure 7.8 shows the two ways of reconstructing the event. The sensitivity study is developed for both topologies separately.

These analyses are performed using the `release-00-07-02` of Basf2. As no decay model of  $\tau^+ \rightarrow \eta\pi^+ \nu_\tau$  has been implemented in any generator,  $4 \times 10^6$  signal events are generated and simulated using a flat phase space generation. This may introduce a sizable systematic error, which is ignored for the moment. The MC datasets used as background were generated

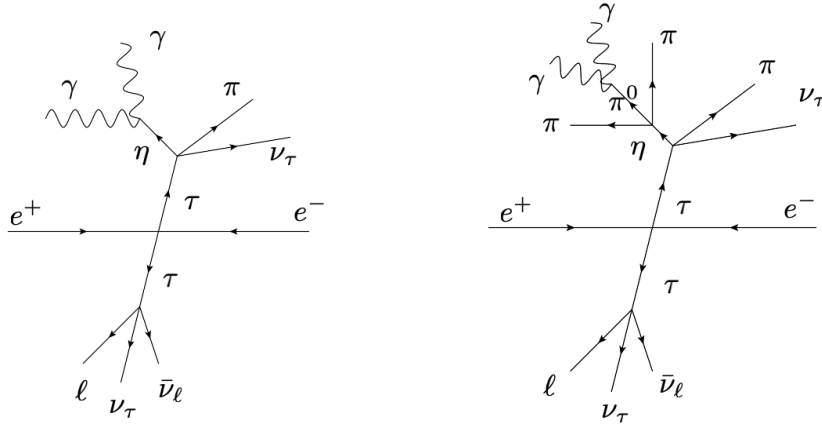


Figure 7.8: 3-1 prong (left) and 1-1 prong (right) topologies for the reconstruction of the decay channel  $\tau^- \rightarrow \eta \pi^- \nu_\tau$ , with a  $\tau$  leptonic decay as tagging.

and simulated during the 7th Belle II Monte Carlo campaign (MC7). Two simulated data samples, equivalent to  $1 \text{ ab}^{-1}$  each one, are taken for the study. They contain samples of generated  $\tau^+ \tau^-$ ,  $\bar{B}B$  and  $\bar{q}q$  pairs with beam background mixed randomly in the events. Details of MC7 can be looked at <https://confluence.desy.de/display/BI/Data+Production+MC7>.

To accept an event, it must have less than 6 charged tracks with  $|dr| < 0.5 \text{ cm}$ ,  $|dz| < 3.0 \text{ cm}$ ,  $p_t > 0.1 \text{ GeV}/c$  and  $-0.8660 < \cos(\theta) < 0.9535$ . It also must have at most 10 photons with  $E_\gamma > 50 \text{ MeV}$  and  $-0.8660 < \cos(\theta_\gamma) < 0.9535$ . The event is split in two using a plane defined by the thrust axis. In the tagging side, a single leptonic track is required. The signal side must contain two photons and 1 or 3 charged tracks for the 1-1 and 3-1 prong topologies, respectively. In the 1-prong case, a  $\pi^0$ -veto is applied in the reconstruction of  $\eta \rightarrow \gamma\gamma$  candidates. Figure 7.9 shows the invariant mass distribution for  $\eta$  candidates from reconstructed signal events using a 1-prong and 3-prong topologies.

As expected, the number of background events is high and covers completely the  $\eta$  region for both topologies (see Fig. 7.10). For this reason, a boosted decision tree (BDT) is trained to discriminate between signal and background events. The MC samples are split in two, using the first half for the BDT training stage and the second for the sensitivity analysis. Details of the training and optimization of the BDT are detailed in Appendix C.

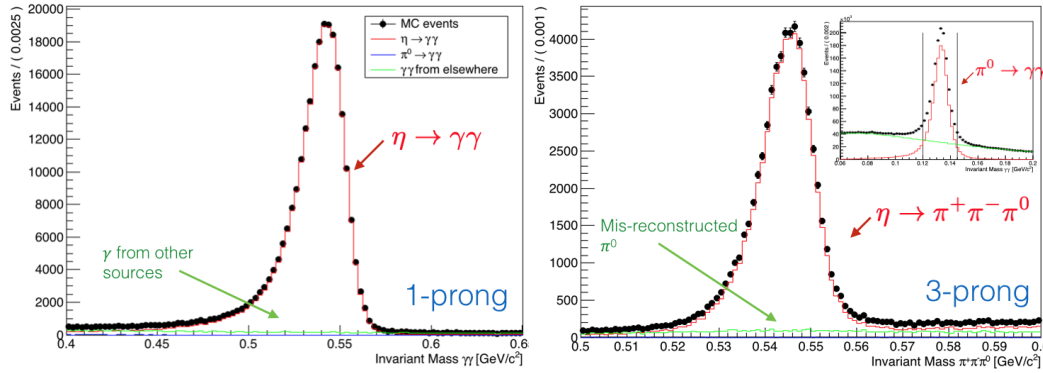


Figure 7.9: Invariant mass distribution of reconstructed  $\eta$  candidates for generated signal events using 1-prong and 3-prong topologies. Efficiency of reconstruction is 13.56% for 1-prong and 3.7% for 3-prong reconstruction. Combinatorial background sources are also indicated in green and blue histograms.

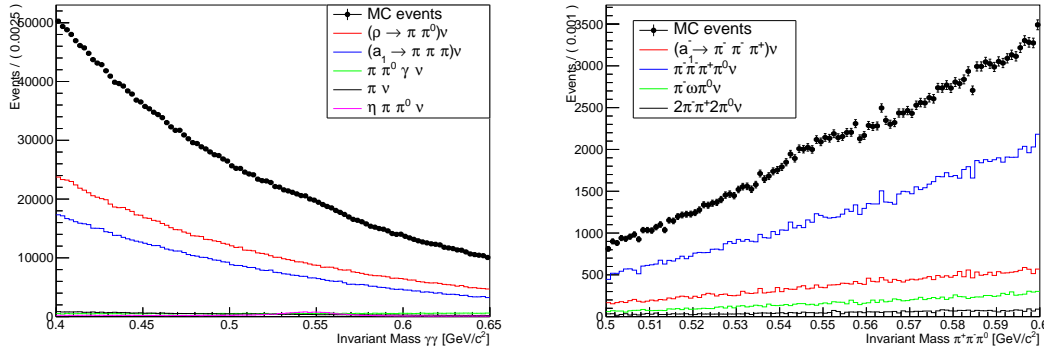


Figure 7.10: Invariant mass distribution of reconstructed  $\eta$  candidates for 1-prong (left) and 3-prong (right) MC background samples.

After optimal BDT cuts are applied, the efficiencies for signal reconstruction are 7.88% and 1.82% for the 1-prong and 3-prong topologies, respectively. In order to count the number of background events above the signal, a fit is performed in the invariant mass distribution of the reconstructed  $\eta$  candidates. Figure 7.11 shows the fits performed using a Crystal-Ball shape p.d.f. [128] for the signal and a first-order polynomial p.d.f. for the combinatorial background. A mass window of  $\mu \pm 3\sigma$  is defined to count the number of background events

below the peak. Figure 7.10 shows the result of counting background events in the  $\mu \pm 3\sigma$  mass window, getting an expected number of background events of 98,146 for the 1-prong topology and 12,120 events for the 3-prong reconstruction.

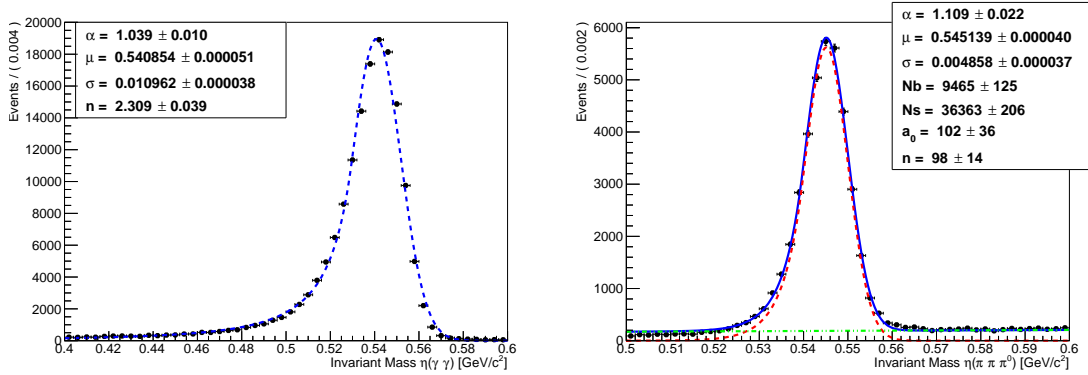


Figure 7.11: Fits performed in invariant-mass distribution of  $\eta$  candidates reconstructed from 1-prong (left) and 3-prong (right) signal events, using a Crystal-Ball shape p.d.f. [128] for the signal and a first-order polynomial p.d.f. for the combinatorial background.

Assuming a linear behavior in the number of background events with respect to the integrated luminosity and no changes in the signal efficiency, it is possible to estimate the confidence intervals for the number of signal events expected for the decay  $\tau^- \rightarrow \eta\pi^- \nu_\tau$  using the Feldman-Cousins method [129]. If the upper limit in the expected number of events is known, it is possible to obtain an upper limit in the branching ratio, in analogy with equation (6.5):

$$\text{BR}(\tau^- \rightarrow \eta\pi^- \nu_\tau) \leq \frac{N_{\max}}{2\Lambda \cdot \mathcal{L}_{\text{int}}}, \quad (7.23)$$

where  $N_{\max} = N_{\max}(N_{\text{sig}}, N_{\text{bkg}})$ ,

$$\Lambda = \sigma(e^+e^- \rightarrow \tau^+\tau^-) \cdot \text{BR}(\eta \rightarrow \gamma\gamma) \cdot \epsilon_{1\text{-prong}}, \quad (7.24)$$

for the 1-prong case and

$$\Lambda = \sigma(e^+e^- \rightarrow \tau^+\tau^-) \cdot \text{BR}(\eta \rightarrow \pi^+\pi^-\pi^0) \cdot \epsilon_{3\text{-prong}}, \quad (7.25)$$

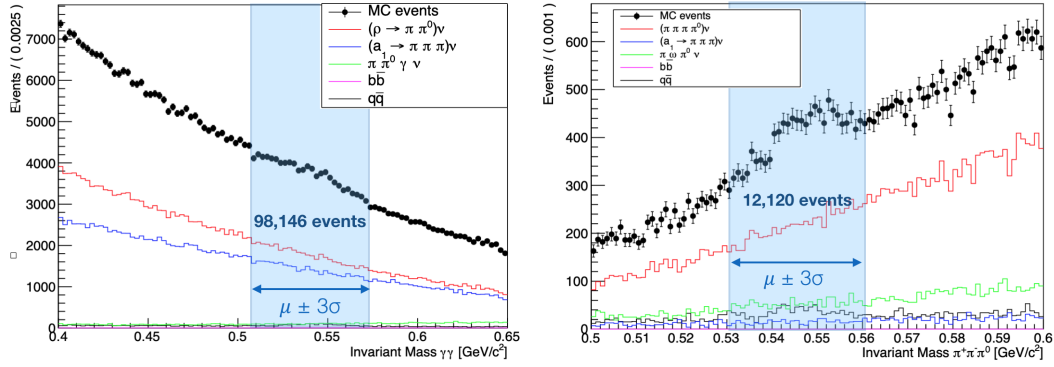


Figure 7.12: Invariant-mass distribution of  $\eta$  candidates reconstructed from 1-prong (left) and 3-prong (right) background events after BDT optimized cuts are applied.

for the 3-prong topology, being  $\varepsilon_{n\text{-prong}}$  the efficiency for the  $n$ -prong case.  $N_{\max}$  depends on the number of expected signal events and given the lack of knowledge in the branching ratio of the decay, it is not possible to estimate  $N_{\text{sig}}$ . For this reason, a weighed average is considered in the estimation of the upper limit, with all the possible values of  $N_{\text{sig}}$ :

$$\text{BR}(\tau^- \rightarrow \eta \pi^- \nu_\tau) \leq \sum_{N_{\text{sig}}} \frac{N_{\max}(N_{\text{sig}}, N_{\text{bkg}})}{2\Lambda \cdot \mathcal{L}_{\text{int}}} \cdot P(N_{\text{sig}} | N_{\text{bkg}}), \quad (7.26)$$

where  $P(N_{\text{sig}} | N_{\text{bkg}})$  is the Poisson probability, given by

$$P(n | \lambda) = \frac{\lambda^n e^{-\lambda}}{n!}. \quad (7.27)$$

Figures 7.13 shows the 95% C.L. branching ratio upper limits estimated for the 1-prong and 3-prong reconstructions. The error bands in the upper limit corresponds to the uncertainty which comes from the Poisson-weighted standard deviation of the possible values of  $N_{\text{sig}}$ . Using the comparison defined in equation (7.20), the upper limits estimated in figure 7.13 can be translated into sensitivity of constrains on the non-standard scalar interactions, in function of the integrated luminosity accumulated by Belle II. Figure 7.14 shows the estimated constrains with reconstructed 1-prong and 3-prong topologies.

## 7.4 Concluding Remarks

The decays  $\tau^- \rightarrow \eta \pi^- \nu_\tau$ , suppressed by  $G$ -parity in the Standard Model, can receive relevant contributions of BSM interactions. Our sensitivity study shows that as soon as Belle II collects an integrated luminosity of  $1 \text{ ab}^{-1}$  of data, the current upper limit on the branching fraction for  $\tau^- \rightarrow \eta \pi^- \nu_\tau$  decays will be improved. From  $2 \text{ ab}^{-1}$  of data, SM predictions for the branching ratio may be tested and constraints in non-standard scalar interactions can be improved, providing limits that are very competitive with other low-energy processes [149].

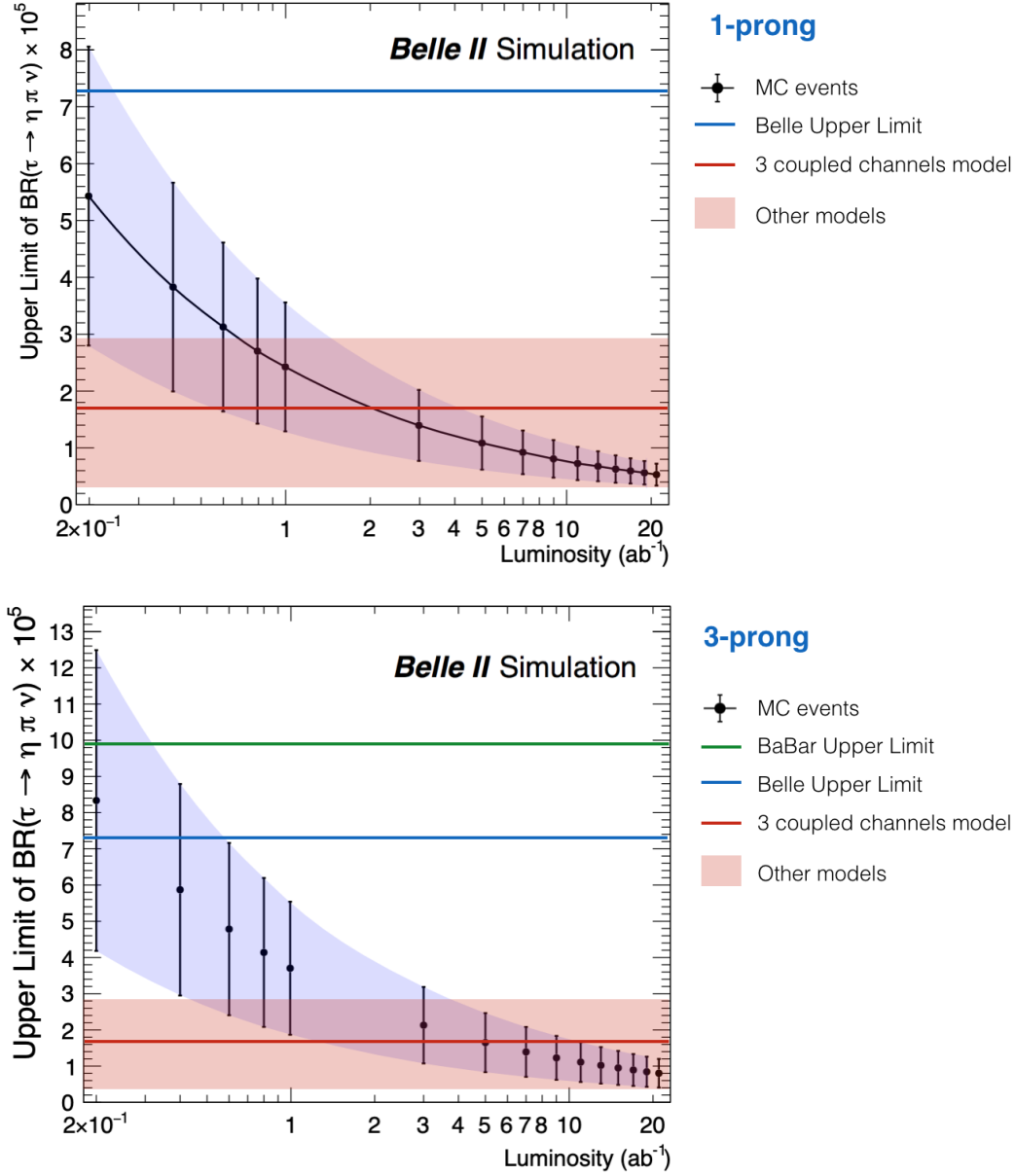


Figure 7.13: 95% C.L. upper limits estimation for the branching ratios of the  $\tau \rightarrow \eta \pi \nu_\tau$  decay, in function of the integrated luminosity and reconstructed by the 1-prong and 3-prong topologies. The blue line corresponds to the upper limit reported by Belle [141], the green to the upper limit reported by BaBar [140] and the red band contains the SM predictions for the branching ratio described in table 7.1. The most recent estimation, developed with 3 coupled channels as a model for the scalar contribution [139] is represented with a red line.



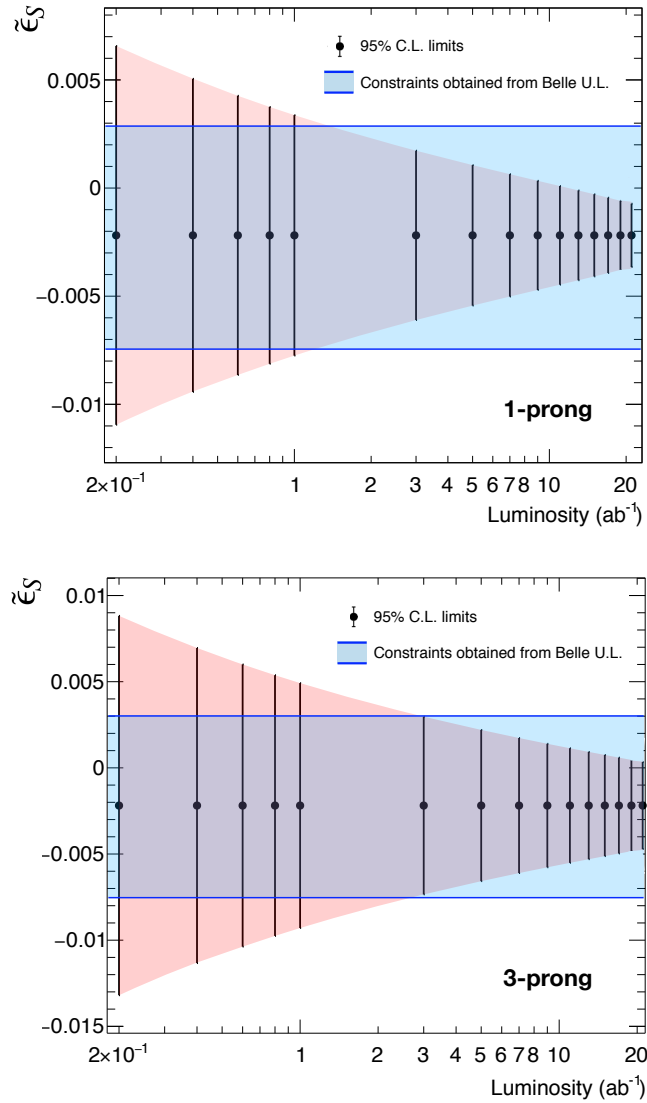


Figure 7.14: Constrains on non-standard scalar interactions estimated from the 95% C.L. upper limits for the branching ratios of the  $\tau^- \rightarrow \eta\pi^- \nu_\tau$  decays at Belle II, as a function of the integrated luminosity and reconstructed by the 1-prong and 3-prong topologies. Blue bands correspond to the constrains imposed from the current upper limit reported by Belle [141].



## Chapter 8

---

### Conclusions and Perspectives

The hypothesis behind the studies performed in this thesis is that precise measurements of the properties of heavy flavors can be very useful to search for potential effects of particles or interactions not contained in the Standard Model. In this thesis, we report our results on measurements, sensitivity and phenomenological studies of the decay properties of the  $B_s^0$  meson and  $\tau$  lepton, which may be useful in the search for New Physics.

The lifetime of the CP-odd decay channel  $B_s^0 \rightarrow J/\psi f_0(980)$  has been measured successfully, obtaining an independent result which, at the moment in which the result was published, confirmed the consistency in the measurements performed by other experiments, as shown in figure 8.1. Our measurement also contributed to the global average of the width of the heavy mass eigenstate of  $B_s^0$ ,  $\Gamma_H$ . Neglecting CP violation in this decay, the measurement can be translated into  $\Gamma_H = 1/\tau$ . From equation (2.17):

$$\Gamma_H = 0.59 \pm 0.05 \text{ (stat)} \pm 0.02 \text{ (syst)} \text{ ps}^{-1}. \quad (8.1)$$

Currently, the CMS collaboration has achieved the most precise lifetime measurement for this channel [51]. Depending on the performance of the accelerator, SuperKEKB could increase the energy at the next resonance  $\Upsilon(5S)$ , allowing the production of  $B_s^0$  mesons at the Belle II experiment. Given the high luminosity expected in such collisions and the good performance of Belle II in the identification of pions and muons [33], the channel  $B_s^0 \rightarrow$

$J/\psi f_0(980)$  may be analyzed at Belle II in the coming years, providing a high-precision  $\Gamma_H$  measurement, useful in the search of leptoquarks and BSM particles contributions in the  $B_s^0 - \bar{B}_s^0$  mixing process [43].

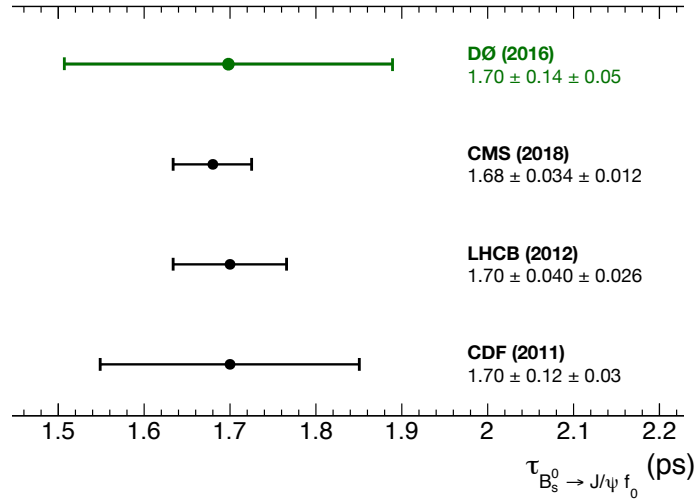


Figure 8.1: Our result of the measurement of the  $B_s$  lifetime in the  $J/\psi f_0(980)$  state in green [55], and comparison with the measurement performed by CDF, LHCb and CMS [48, 50, 51].

The Phase II in the commissioning of Belle II provided highly valuable results for the collaboration. The measurement and characterization of background coming from the beam will be critical for the improvement of the simulations with beam background conditions active. In particular, the early data allowed us to test the analysis techniques and the software developed for the  $\tau$  pair events reconstruction. With the first collisions to be obtained in Phase III, the comparison between data and MC simulations will be an important step. Also, improvements in the skimming dedicated for  $\tau$  analysis and triggers have to be performed.

In this thesis the first measurement of the  $\tau$  lepton mass at Belle II is reported [34], obtaining

$$m_\tau = (1776.4 \pm 4.8(\text{stat}))\text{MeV}/c^2, \quad (8.2)$$

consistent with measurements reported in previous experiments, as shown in figure 8.2. This result verifies that Belle II hardware subsystems, simulations, and software are working prop-

erly and, in particular, it shows the capacities of  $\tau$  lepton analysis at the experiment with just a few inverse picobarns accumulated. If we are capable of reducing the systematic uncertainties in the  $\tau$  mass measurement, a high luminosity result will improve uncertainties in tests such as leptonic universality.

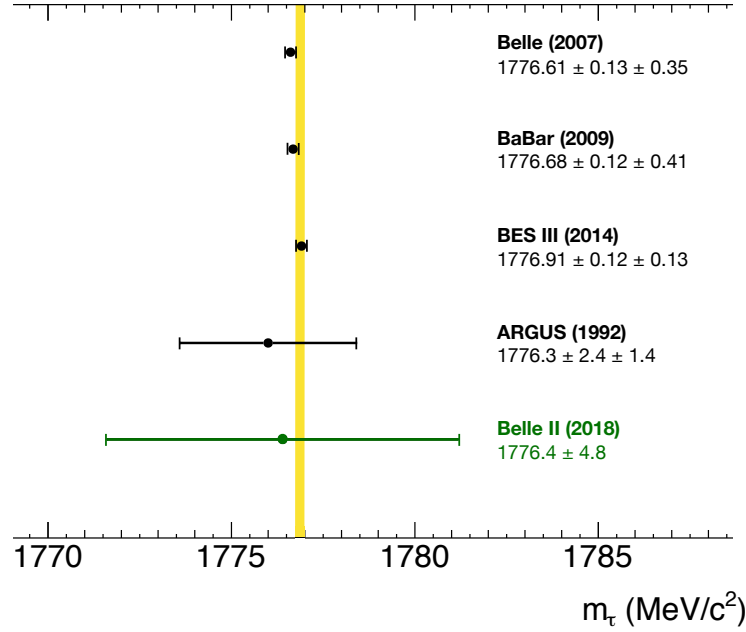


Figure 8.2: Comparison between the  $\tau$  lepton mass measurement performed by Belle II and the values obtained for previous experiments.  $\tau$  lepton mass average reported by the PDG [35] is represented by the yellow line.

Figure 6.7 shows the current capacity of the Belle II experiment in the reconstruction of the decay channel  $\tau^- \rightarrow \eta \pi^- \pi^0 \nu_\tau$ , using single cuts in kinematic variables to increase the purity of the sample. Around  $1 \text{ ab}^{-1}$ , Belle II will improve the uncertainty in the measurement of the branching ratio. This will be critical to confirm or discard the tension between the  $\tau$  decay measurements and the  $e^+e^-$  hadronic production using CVC, which cannot be explained by breaking of SU(2) isospin symmetry. Furthermore, improved measurements of the invariant mass distributions of the hadronic system  $\eta \pi^\pm \pi^0$  will allow a direct test with the

cross section of  $e^+e^- \rightarrow \eta\pi^+\pi^-$ . This will contribute with a clue in order to solve the puzzle of inconsistency between the  $\tau$  decays and  $e^+e^-$  hadronic production data [123], which takes relevance if  $\tau$  decays are required as high-precision input for the SM estimation of  $(g_\mu - 2)$ .

Our aim at the Belle II experiment is the first observation of the decay channel  $\tau^- \rightarrow \eta\pi^- \nu_\tau$  or, in case of a negative result, improvement of upper limit in the branching ratio. Figure 7.13 shows Belle II will have the capability of testing SM predictions for the branching ratio of the decay once the integrated luminosity reaches  $2 \text{ ab}^{-1}$ . It is important to point out that signal events were simulated using a flat phase space generation and the implementation of a decay model will be relevant in a more detailed study of kinematic distributions. Additionally, the current simulations use generated beam background effects, which not necessarily reproduce the real conditions of radiation coming from the beam [84, 150]. It will be important the reprocessing of the sensitivity study using simulations with realistic beam background effects, mainly for the 1-1 prong topology reconstruction, which is the most sensitive to fake  $\eta \rightarrow \gamma\gamma$  candidates. Recently, it has been shown that  $\tau^- \rightarrow \eta\pi^- \nu_\tau \gamma$  decays, not suppressed by G-parity and acting as background for the SCC searches, have a branching ratio of the same order as the non-radiative  $\tau^- \rightarrow \eta\pi^- \nu_\tau$  signal [151]<sup>1</sup>. The number of background events can increase with this additional contribution and the implementation of it in the generation models will be a critical step in the future. When needed,  $\tau^- \rightarrow (a_1 \rightarrow \pi^- \pi^+ \pi^-) \nu_\tau$  background can be improved using reference [153], which supersedes [154] included in [155]. The  $\tau^- \rightarrow \pi^- \pi^+ \pi^- \pi^0 \nu_\tau$  background is more problematic, as [156] and [157] are not precise enough and a dedicated study is needed.

The decay  $\tau^- \rightarrow \eta\pi^- \nu_\tau$  provides the best mechanism for the study of charged scalar currents at tree level, closely related to the search of an intermediate charged Higgs in the decay. Given the limits imposed in the effective scalar coupling as shown in figure 7.7 and table 7.2, the energy scale of the particle associated with the scalar interactions must be larger than 3 TeV, consistent with current constraints in models which involve extra Higgs doublets [24]. Collecting more than  $1 \text{ ab}^{-1}$  of data, a measurement of the branching ratio

---

<sup>1</sup>Loop-level processes, induced by the  $\eta\gamma\gamma$  transition form factor, are negligible [152].

and kinematic distributions of  $\tau^- \rightarrow \eta\pi^- \nu_\tau$  at Belle II will impose the strongest limits in the non-standard scalar coupling value, as shown in figure 7.14.

In summary, the full physics program of the Belle II collaboration will start in 2019 and by the end of the experiment, in 2025, Belle II is expected to collect  $50 \text{ ab}^{-1}$  of data. The  $\tau$  lepton physics program will take advantage of the largely integrated luminosity expected, allowing the study of several topics. Limits in branching ratio of LFV decays, CP violation asymmetries and Michel parameters will be improved by two orders of magnitude. This thesis shows the potential of precision measurements in the decay channel  $\tau^- \rightarrow \eta\pi^- \pi^0 \nu_\tau$ , second-class currents discovery and constraints in non-standard scalar interactions through the decay channel  $\tau^- \rightarrow \eta\pi^- \nu_\tau$ . As soon as the Belle II experiment collects the integrated luminosity required, constraints in SM and non-standard parameters will be improved, providing limits that will be very competitive with the currently available results.





## Appendix A

---

# Systematic Uncertainties in the $B_s^0$ Lifetime Measurement

For the systematic uncertainties on the lifetime measurement, the following sources have been considered:

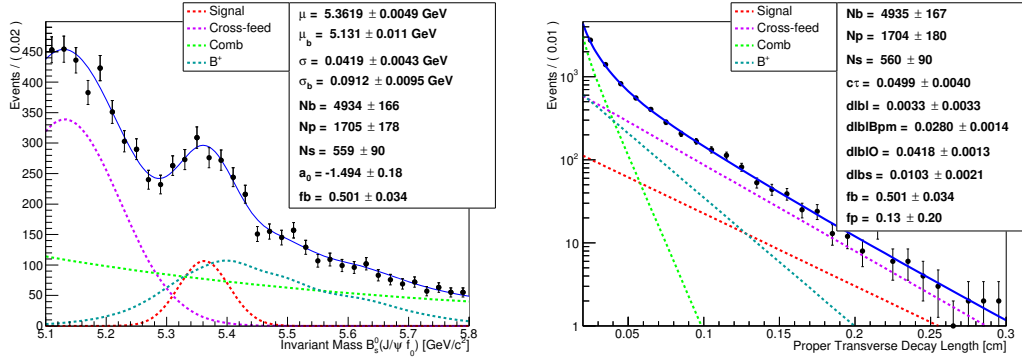
- Detector alignment.
- Possible contaminations in the  $\pi^+\pi^-$  mass window.
- Bias due to the likelihood fit on low statistics.
- Distribution models.

Detector alignment effects has been previously estimated [158] to be  $5.4 \mu m$ . The systematic uncertainties on the lifetime measurement due to the other mentioned sources are described in this appendix.

### A.1 $f_0(980)$ Mass Window

The  $\pm 100 \text{ MeV}/c^2$   $\pi^+\pi^-$  mass window around the  $f_0(980)$  could include some contamination from similar hadronic states. The size of the  $\pi^+\pi^-$  mass window is changed from  $\pm 80$

$\pi^+\pi^-$ mass window (MeV)	Lifetime ( $\mu\text{m}$ )	Variation w.r.t. nominal ( $\mu\text{m}$ )
120	$498.6 \pm 39.8$	5.4
110	$499.6 \pm 40.7$	4.4
100 (nominal)	$504.0 \pm 42.4$	-
90	$502.4 \pm 40.7$	1.6
80	$488.0 \pm 40.0$	16.0

Table A.1: Lifetime fit with the variation in the  $\pi^+\pi^-$  mass window around the  $f_0(980)$ .Figure A.1: Likelihood fit result of  $\tau = (498.6 \pm 39.8) \mu\text{s}$  for invariant mass (left) and proper transverse decay length (right) distributions. Selected invariant mass window of the  $f_0(980)$  is  $120 \text{ MeV}/c^2$  around the signal peak.

$\text{MeV}/c^2$  to  $\pm 120 \text{ MeV}/c^2$  to vary any possible contamination inside the mass window. The lifetime fit is repeated for each of the new  $\pi^+\pi^-$  mass windows. The largest deviation observed is  $16.0 \mu\text{s}$  and 1/2 of this deviation is considered as a systematic uncertainty due to this source. Table A.1 summarizes the results and figures A.1 - A.4 show some of the fit results superimposed to the data.

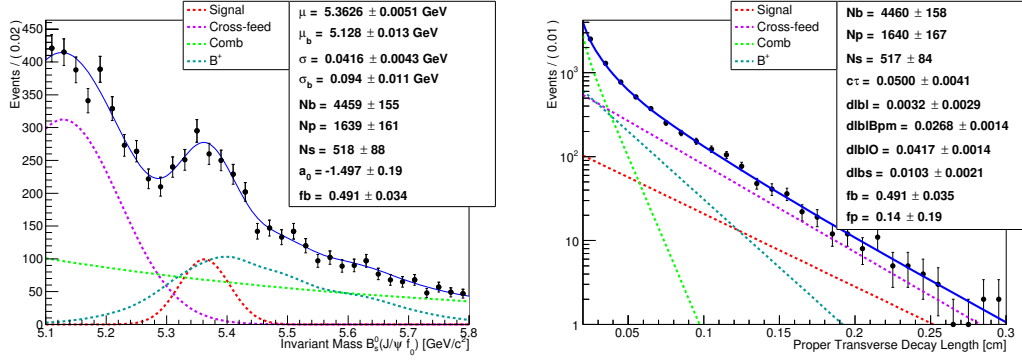


Figure A.2: Likelihood fit result of  $c\tau = (499.6 \pm 40.7)\mu\text{m}$  for invariant mass (left) and proper transverse decay length (right) distributions. Selected invariant mass window of the  $f_0(980)$  is  $110 \text{ MeV}/c^2$  around the signal peak.

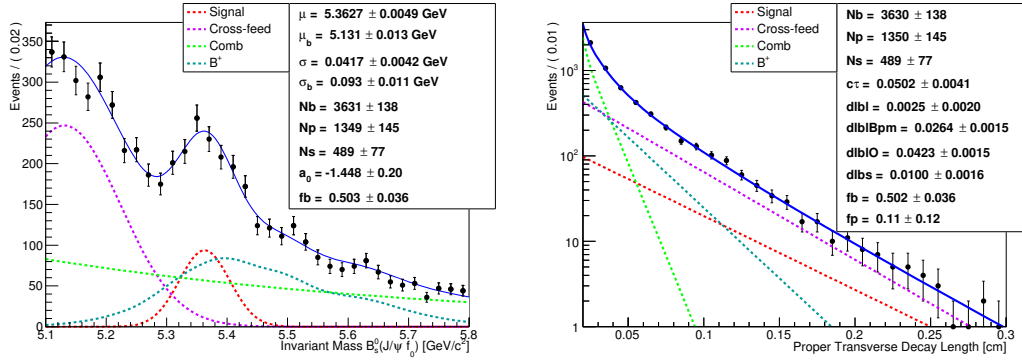


Figure A.3: Likelihood fit result of  $c\tau = (502.4 \pm 40.7)\mu\text{m}$  for invariant mass (left) and proper transverse decay length (right) distributions. Selected invariant mass window of the  $f_0(980)$  is  $90 \text{ MeV}/c^2$  around the signal peak.

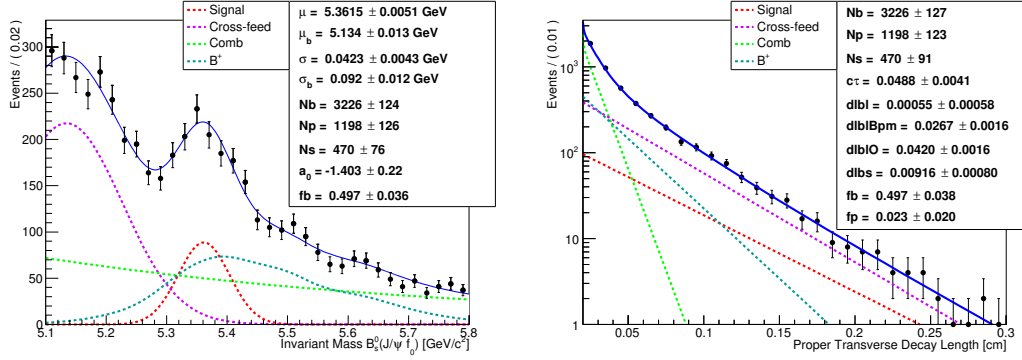


Figure A.4: Likelihood fit result of  $c\tau = (488.0 \pm 41.0)\mu m$  for invariant mass (left) and proper transverse decay length (right) distributions. Selected invariant mass window of the  $f_0(980)$  is  $80 \text{ MeV}/c^2$  around the signal peak.

## A.2 Fit Bias

Fits to pseudo-experiments are performed, following the models as used for the measurement, in order to explore any bias introduced by the fit method. The statistics of the pseudo-experiments are set to what is observed in data. From 10K pseudo-experiments with the lifetime input set to the value measured in data, a bias in the lifetime fit estimate of around  $-4.4 \mu m$  with respect to the input value is observed. This value is subtracted from the nominal measurement to correct the bias. This exercise is repeated for different input lifetime values and for different statistics. Figure A.5 shows the result of this study. To estimate a systematic uncertainty, the observed deviation is averaged from the input lifetime value for lifetimes in the range of  $300 - 800 \mu m$ . The average deviation is estimated to be  $-4.4 \mu m$ . This is assigned as a systematic uncertainty.

## A.3 Distribution Models

We estimate the systematic uncertainty due to the models for the  $\lambda$  and mass distributions by varying the parameterizations of the different components: (i) the cross-feed contamination

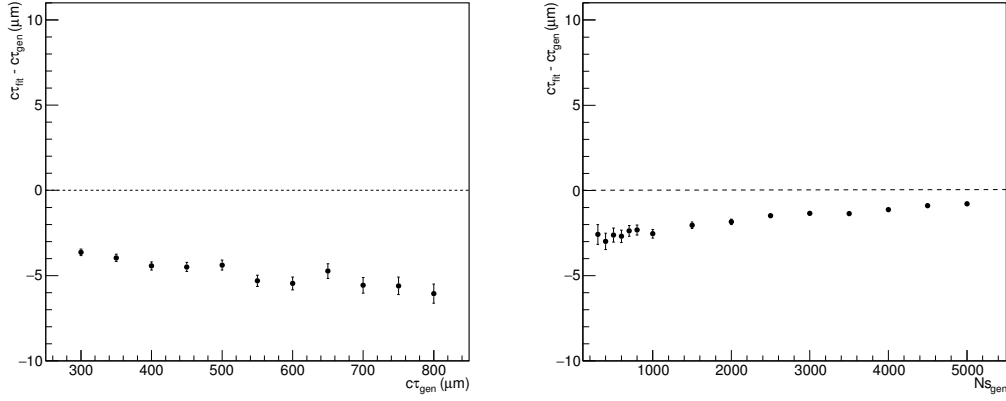


Figure A.5: Deviation on the fitted lifetime as function of the input lifetime (left) and as function of the number of signal events (right) in toy MC generation. Each point represents the lifetime mean value from an ensemble of ten thousand fitted MC samples.

is modeled by two Gaussian functions instead of one, (ii) the exponential function in the combinatorial background model are replaced by a first order polynomial, (iii) the smoothing of the non-parametric function that models the  $B^+$  contamination is varied, and (iv) the decays describing the background components in  $\lambda$  are convoluted with the resolution. To take into account correlations between the effects of the different models, a fit that combines all different model changes is performed. We quote the difference between the result of this fit and the nominal fit as the systematic uncertainty. In this case, the fit yields a lifetime of  $(491.5 \pm 53.7) \mu m$ . Figure A.6 shows the fit result with the changes in the distribution models.

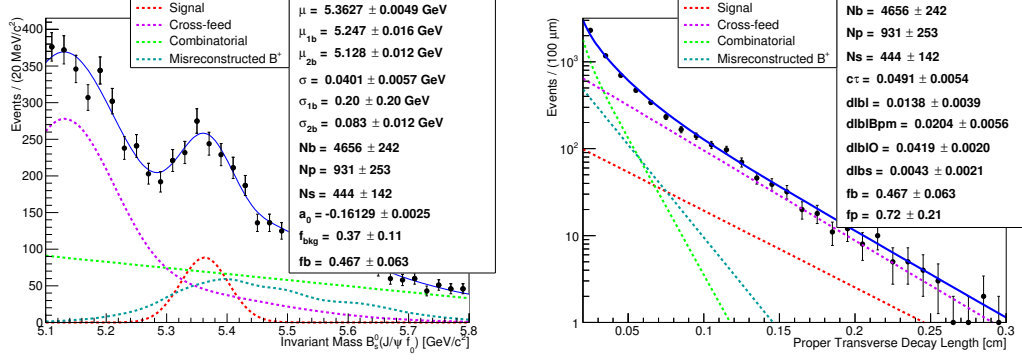


Figure A.6: Likelihood fit result of  $c\tau = (491.5 \pm 53.7)\mu\text{m}$  for invariant mass (left) and proper transverse decay length (right) distributions. The parameterizations of the different components is changed to estimate the systematic uncertainty due to the models for the  $\lambda$  and mass distributions.

# Appendix B

---

## Reconstruction and selection of $\tau^- \rightarrow \eta \pi^- \pi^0 \nu_\tau$ decays

### B.1 Basf2 analysis steering file

Steering file written for Basf2 release-02-00-02. It reconstruct events

$(\tau_{\text{sig}}^+ \rightarrow \eta \pi^+ \pi^0 \nu_\tau)(\tau_{\text{tag}}^- \rightarrow \ell^- \bar{\nu}_\ell \nu_\tau)$  and stores the information in Ntuples.

```
1  #!/usr/bin/env python3
2  # -*- coding: utf-8 -*-
3  from basf2 import *
4  from modularAnalysis import *
5  from variables import variables
6  from stdCharged import *
7  from stdPhotons import *
8  from stdPi0s import *
9  import sys
10 # Name of the output Ntuple
11 if '--ntuple' in sys.argv:
12     outputNtuple = sys.argv[sys.argv.index('--ntuple') + 1]
13 else:
14     outputNtuple = 'tau_BGx0'
15 ##### Input #####
16 inputFiles = []
17 #KEKCC signal, overwritten with -i flag
```

```

18 inputFiles.append('/Belle2/tau_etapi0nu/Ntuples/tau_etaPiPi0_skim.udst.root')
19 inputMdstList('default', inputFiles)
20 use_central_database("GT_gen_prod_004.10_release-01-00-00")
21
22 ##### 1-1 prong selection #####
23 mcTruth = True
24 # Default cuts of EventShape
25 trackCuts = 'pt > 0.1'
26 trackCuts += ' and -0.8660 < cosTheta < 0.9535'
27 trackCuts += ' and -3.0 < dz < 3.0'
28 trackCuts += ' and -0.5 < dr < 0.5'
29 variables.addAlias('nGoodTracksForTau', 'nClearedTracks(%s)' % trackCuts)
30 # Looking for two tracks and 4 gammas.
31 eventCuts = '1 < nClearedTracks(%s) < 3' % trackCuts
32 applyEventCuts(eventCuts)
33 buildEventShape()
34 stdPi('95eff')
35 stdMu('95eff')
36 stdE('95eff')
37 applyCuts('pi+:95eff', trackCuts)
38 applyCuts('mu+:95eff', trackCuts)
39 applyCuts('e+:95eff', trackCuts)
40 stdPhotons('tight')
41 stdPi0s('eff40')
42 variables.addAlias('nGoodGammasForTau', 'countInList(gamma:tight)')
43 variables.addAlias('goodPhotonsEnergy', 'totalEnergyOfParticlesInList(gamma:tight)')
44 # Pi0 veto (pi0eff40)
45 variables.addAlias('pi0veto', 'veto(gamma:tight, 0.124 < M < 0.140)')
46 variables.addAlias('nGoodGammasForEta', 'countInList(gamma:tight, pi0veto != 1)')
47 applyCuts('gamma:tight', 'veto(gamma:tight, 0.124 < M < 0.140) != 1')
48 reconstructDecay('eta:gg -> gamma:tight gamma:tight', '0.4 < M < 0.65')
49 # Signal and leptonic tag reconstruction
50 reconstructDecay('tau+:signal -> eta:gg pi0:eff40 pi+:95eff', '0 < M < 1.8')
51 # Mix tag
52 reconstructDecay('tau-:muon -> mu-:95eff', '0 < M < 1.8')
53 reconstructDecay('tau-:electron -> e-:95eff', '0 < M < 1.8')
54 copyLists('tau+:tag', ['tau+:muon', 'tau+:electron'])
55 tagParticle = 'mu'
56 # eta and pi0 in signal side
57 variables.addAlias('prodCosEtaPi0', 'formula(daughter(0, cosToEvtThrust)*daughter(1, cosToEvtThrust))')
58 # eta and pi in signal side
59 variables.addAlias('prodCosEtaPi', 'formula(daughter(0, cosToEvtThrust)*daughter(2, cosToEvtThrust))')

```



```

60 applyCuts('tau:signal', 'prodCosEtaPi0 > 0 ')
61 applyCuts('tau:signal', 'prodCosEtaPi > 0 ')
62 if mcTruth:
63     labelTauPairMC()
64     matchMCTruth('tau:signal')
65     matchMCTruth('tau:tag')
66     reconstructDecay('Z0:taupair -> tau:signal tau:tag', '')
67     # Muon and pion in opposite side
68     variables.addAlias('prodPiMuCosTh', 'formula(daughter(0, daughter(2, cosToEvtThrust)) * \
69     daughter(1, daughter(0, cosToEvtThrust)))')
70     applyCuts('Z0:taupair', 'prodPiMuCosTh < 0')
71     toolsZ0 = ['EventMetaData', '^Z0']
72     toolsZ0 += ['RecoStats', '^Z0']
73     toolsZ0 += ['EventShape', 'Z0 -> [^tau+ -> [^eta -> ^gamma ^gamma] ^pi0 ^pi+] ^tau-']
74     toolsZ0 += ['InvMass', 'Z0 -> [^tau+ -> ^eta ^pi0 pi+] tau-']
75     toolsZ0 += ['CustomFloats[charge]', 'Z0 -> ^tau+ ^tau-']
76     toolsZ0 += ['Kinematics',
77     'Z0 -> [^tau+ -> [^eta -> ^gamma ^gamma] [^pi0 -> ^gamma ^gamma] ^pi+] ^tau-']
78     if mcTruth:
79         toolsZ0 += ['MCTruth', 'Z0 -> [^tau+ -> ^eta ^pi0 ^pi+] ^tau-']
80         toolsZ0 += ['MCKinematics', 'Z0 -> [^tau+ -> ^eta ^pi0 ^pi+] ^tau-']
81         toolsZ0 += ['CustomFloats[isSignalAcceptMissingNeutrino]', 'Z0 -> ^tau+ ^tau-']
82         toolsZ0 += ['CustomFloats[tauPlusMCMODE]', '^Z0']
83         toolsZ0 += ['CustomFloats[tauMinusMCMODE]', '^Z0']
84     ntupleFile('Ntuples/tau_etaPiPi0_%s_lepTag.root' % outputNtuple)
85     ntupleTree('Z0', 'Z0:taupair', toolsZ0)
86     process(analysis_main)
87     print(statistics)

```

## B.2 Kinematic distributions and selection cuts

The search of  $\tau^- \rightarrow \eta \pi^- \pi^0 \nu_\tau$  decays is performed reconstructing  $\tau$  pair candidates in 1-1 prong events (See Fig. 6.5). After reconstruction, selection cuts in kinematic variables are applied in order to increase the signal purity. The list of cuts applied, in sequential order, are:

**Cut 1** (Fig. B.1): All photons coming from  $\eta \rightarrow \gamma\gamma$  candidates should have an energy  $E_\gamma > 100\text{MeV}$ . If  $-0.7 < \cos(\theta_\gamma) < 0.8$ , photons must satisfy  $E_\gamma > 300\text{MeV}$ .

**Cut 2** (Fig. B.2): All photons coming from  $\pi^0 \rightarrow \gamma\gamma$  candidates must satisfy  $E_\gamma >$

60 MeV. If  $\cos(\theta_\gamma) < -0.7$ ,  $E_\gamma > 200 \text{ MeV}$  is required.

**Cut 3** (Fig. B.3): If the polar angle of the missing momentum doesn't satisfy  $|\cos(\theta_{\text{miss}})| < 0.95$ , the event is rejected. The missing momentum magnitude should have  $P_{\text{miss}} > 100 \text{ MeV}$ . If  $\cos(\theta_{\text{miss}}) < -0.8$  or  $\cos(\theta_{\text{miss}}) > 0.6$ ,  $P_{\text{miss}} > 200 \text{ MeV}$  must be satisfied.

**Cut 4** (Fig. B.4): If  $\theta_{(\text{miss}, \text{thr})}$  is the angle between the missing momentum and thrust axis, this must satisfy  $|\cos \theta_{(\text{miss}, \text{thr})}| > 0.7$ . Otherwise, the event is rejected.

**Cut 5** (Fig. B.5): The angle between  $\gamma$ 's from  $\eta \rightarrow \gamma\gamma$  candidates should be lower than 1.5 rad. If not, the candidate is discarded.

**Cut 6** (Fig. B.6): If the asymmetry between the  $\gamma$ 's from  $\eta \rightarrow \gamma\gamma$  candidates, defined as  $A_\eta = |E_{\gamma_1} - E_{\gamma_2}| / (E_{\gamma_1} + E_{\gamma_2})$ , is larger than 0.7, the event is rejected.

**Cut 7** (Fig. B.7): The transverse momentum of  $\pi^0$  and  $\eta$  candidates should be larger than 0.7 GeV/c and 1.2 GeV, respectively.

**Cut 8** (Fig. B.8): The number of photons in the event should be at most 6. If the event contains more, it is discarded.

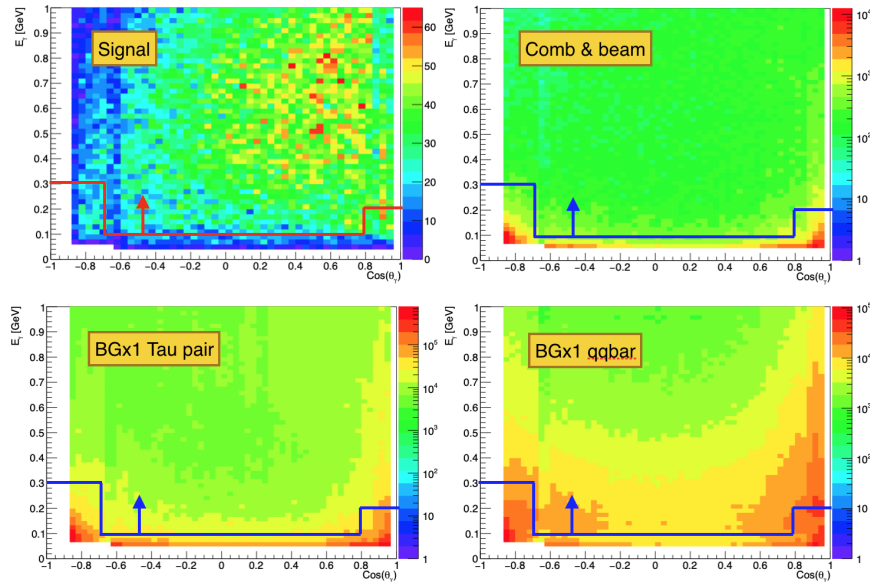


Figure B.1: Distributions of  $E_\gamma$  vs  $\theta_\gamma$  of  $\gamma$ 's from  $\eta \rightarrow \gamma\gamma$  candidates for MC signal and background samples after 1-1 prong preselection.

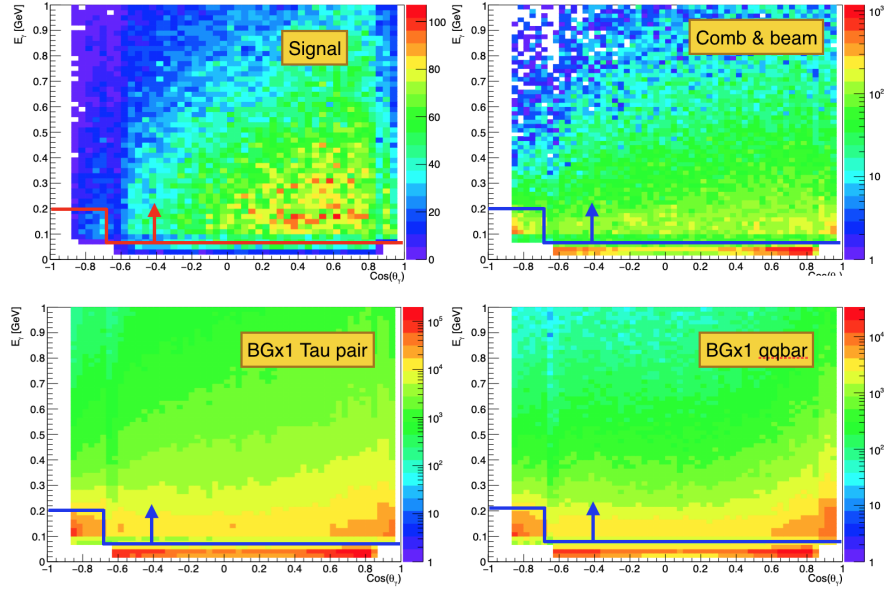


Figure B.2: Distributions of  $E_\gamma$  vs  $\theta_\gamma$  of  $\gamma$ 's from  $\pi^0 \rightarrow \gamma\gamma$  candidates for MC signal and background samples after cut 1 is applied.

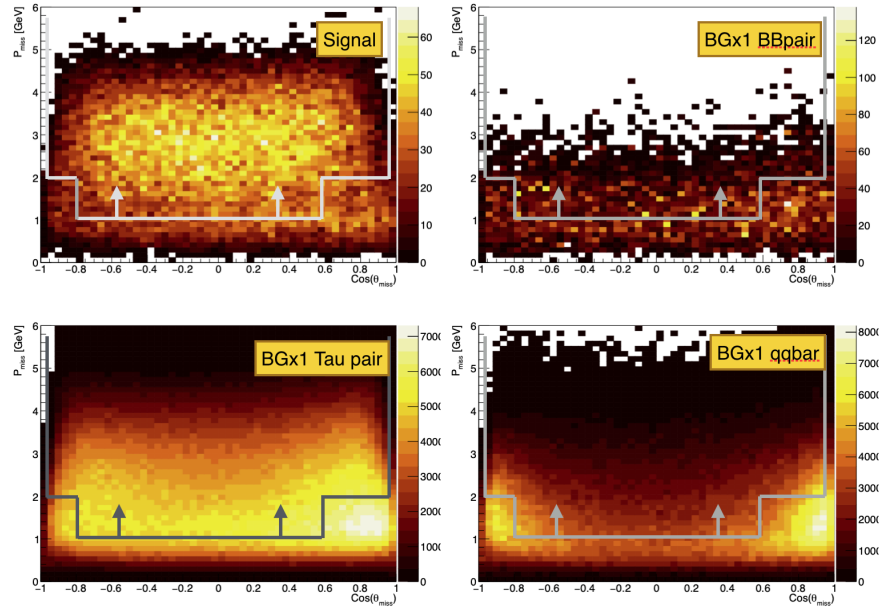


Figure B.3: Distributions of  $P_{\text{miss}}$  vs  $\theta_{\text{miss}}$  of events from MC signal and background samples after cut 2 is applied.

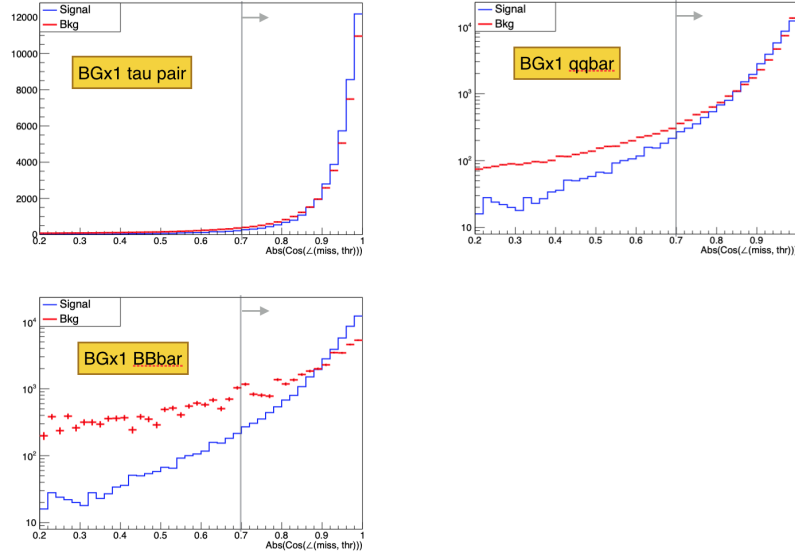


Figure B.4: Distributions of cosine of angle between the missing momentum and thrust axis from MC signal and background samples after cut 3 is applied.

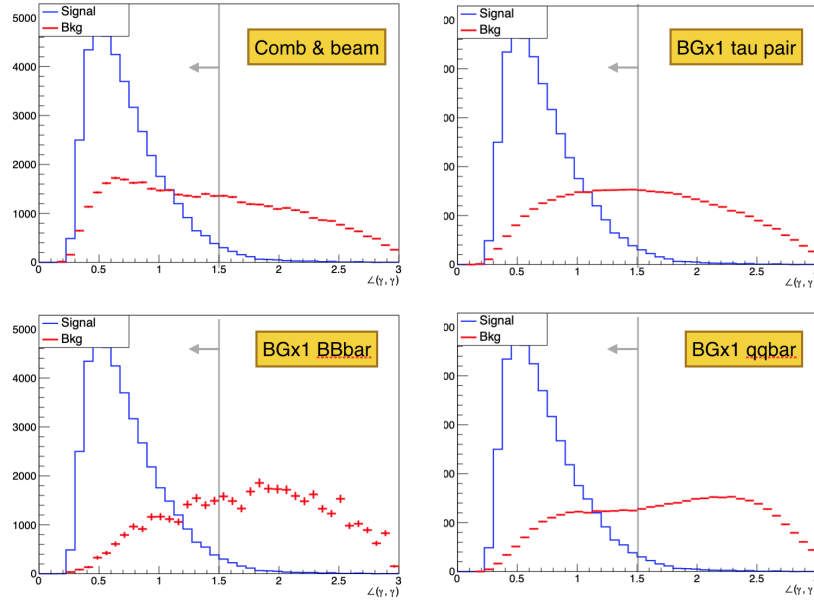


Figure B.5: Distribution of angle between  $\gamma$ 's from  $\eta \rightarrow \gamma\gamma$  candidates from MC signal and background samples after cut 4 is applied.

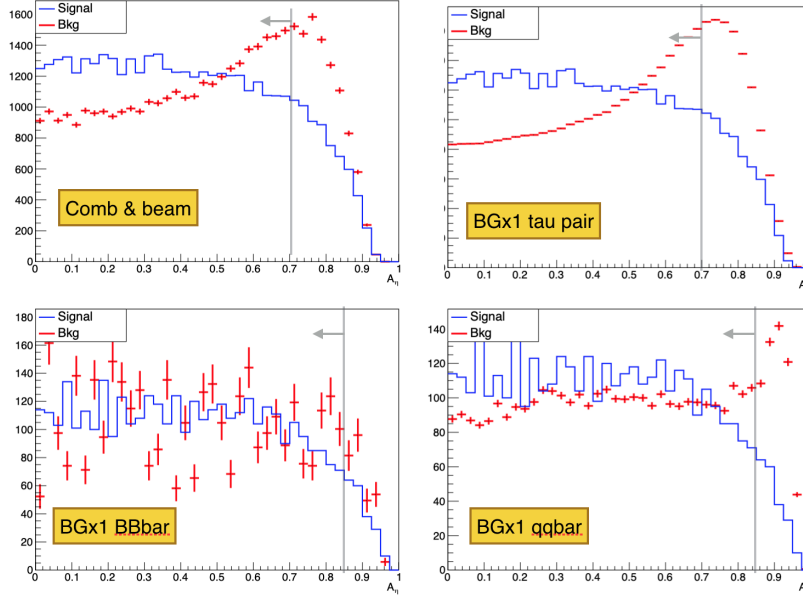


Figure B.6: Distribution of asymmetry between the  $\gamma$ 's from  $\eta \rightarrow \gamma\gamma$  candidates, defined as  $A_\eta = |E_{\gamma_1} - E_{\gamma_2}| / (E_{\gamma_1} + E_{\gamma_2})$ , from MC signal and background samples after cut 5 is applied.

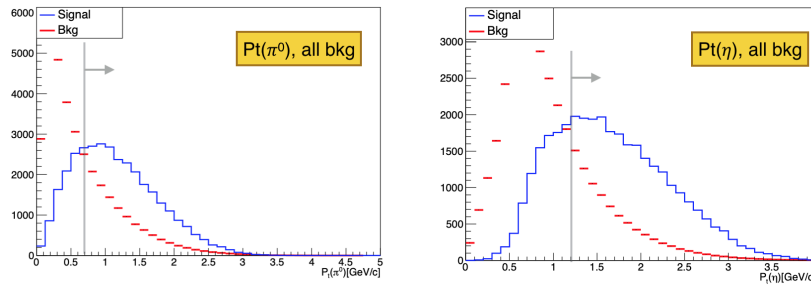


Figure B.7: Distributions of transverse momentum of  $\pi^0$  and  $\eta$  candidates after cut 6 is applied. MC signal events are represented by the blue histogram, meanwhile background events, containing  $B\bar{B}$ ,  $q\bar{q}$  and  $\tau$  pair samples, are represented with the red histogram.

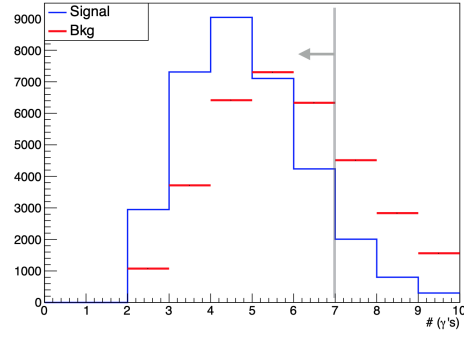


Figure B.8: Distribution of number of photons in signal and background events after cut 7 is applied.

# Appendix C

## $\tau^- \rightarrow \eta \pi^- \nu_\tau$ reconstruction, BDT training and optimization

### C.1 Generation

Since the process  $\tau^- \rightarrow \eta \pi^- \nu_\tau$  is not included in the decay tables of the generators TAUOLA / KKMC, it is not simulated during the official Monte Carlo campaigns of Belle II. Then is necessary to make our own simulations. For this study, 4 million of events were generated using the generator KKMC for the signal and the leptonic decays implemented in TAUOLA as tagging.

The decay table, called `a0mmu_muTag.dat`, following the PYTHIA6 style [159] and used as input for KKMC in the steering file is:

```
1      15 tau-      tau+      -3 0 1      1.77700      0.00000      0.00000 8.72000E-02 0
   ↪ 1
2 3 2101 0.500000 -12 11 16 0 0 ! e- nu nu (PDG2006)
3 3 2102 0.500000 -14 13 16 0 0 ! mu- nu nu
4 2 41 1.000000 16 -9000211 0 0 0 ! a0- nu
5 9000211 a0+ a0- 3 0 1 0.98510 0.10000 1.00000 0.00000E+00 0 1
6 1 0 1.000000 211 221 0 0 0
```

The steering file has been written to work with Basf2 release-00-07-02:

```

1  #!/usr/bin/env python3
2  # -*- coding: utf-8 -*-
3  from basf2 import *
4  from ROOT import Belle2
5  from beamparameters import add_beamparameters
6  from simulation import add_simulation
7  from reconstruction import add_reconstruction
8  from reconstruction import add_mdst_output
9  import os, sys
10 set_log_level(LogLevel.INFO)
11 outpath = './'
12 decpath = './'
13 if not os.path.isfile(decpath + 'a0mnu_muTag.dat'):
14     print("[ERROR] Decay table 'a0mnu_muTag.dat' not found. Check the path.")
15     sys.exit()
16 # main path
17 main = create_path()
18 # event info setter
19 main.add_module("EventInfoSetter", expList=1, runList=1, evtNumList=1000)
20 # beam parameters
21 beamparameters = add_beamparameters(main, "Y4S")
22 # to run the framework the used modules need to be registered
23 kkgeninput = register_module('KKGenInput')
24 kkgeninput.param('tauinputFile', Belle2.FileSystem.findFile('data/generators/kkmc/tau.input.dat'))
25 kkgeninput.param('KKdefaultFile', Belle2.FileSystem.findFile('data/generators/kkmc/KK2f_defaults.dat'))
26 # Decay table for tau --> (a0 --> eta pi) nu
27 kkgeninput.param('taudecaytableFile', decpath + '/a0mnu_muTag.dat')
28 # run
29 main.add_module("Progress")
30 main.add_module(kkgeninput)
31 main.add_module("PrintMCParticles", logLevel=LogLevel.INFO, onlyPrimaries=False)
32 # detector simulation (No beam background)
33 bg = None
34 add_simulation(main, bkgfiles=bg)
35 # reconstruction
36 add_reconstruction(main)
37 # output
38 add_mdst_output(main, True, outpath + 'tau_a0mnul.mdst.root')
39 # generate events
40 process(main)
41 # show call statistics
42 print(statistics)

```



## C.2 Reconstruction

At the moment of the sensitivity study of the decay  $\tau^- \rightarrow \eta \pi^- \nu_\tau$ , the analysis tools for  $\tau$  pairs reconstruction were not included in Basf2 (release-00-07-02). For this reason, an independent-framework reconstruction was developed, using a tdst format (deprecated) from mdst files. More information about the tdst can be found at <https://kds.kek.jp/indico/event/19103/session/11/contribution/52/material/slides/0.pdf>.

As background samples, samples of  $\tau$  pair,  $B\bar{B}$  and  $q\bar{q}$  from the 7th Monte Carlo campaign (MC7) were used.

## C.3 Boosted Decision Trees

Given the high amount of background expected, a boosted decision tree (BDT) is used to discriminate events between signal and background. It consists in extending a simple cut-based analysis into a multivariate technique [160]. A consecutive set of questions are made, with only two possible answers. Each question depends of the formerly given answers and final verdict is reached after a given maximum number of questions (See Fig. C.1). The usage of a BDT includes tree stages: training, testing and evaluation. For the first two stages half of the data samples are used. The second half of data is used for the evaluation stage. The BDT is implemented using the class TVMA of ROOT version 6.11 [161, 162].

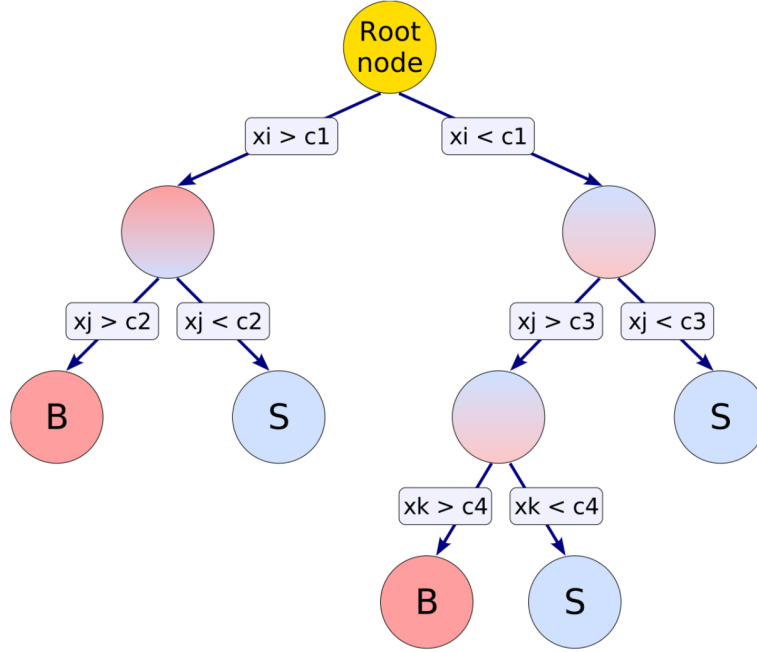


Figure C.1: Schematic view of a BDT. A consecutive set of questions with two possible answers and final states, which discriminate if an entry is signal or background.

The variables selected for the 1-prong analysis are:

- $\angle(\eta, \pi)$ : The angle between the  $\eta$  and  $\pi$  momentum.
- $\angle(p_{\text{miss}}, \hat{n}_{\text{thr}})$ : The angle between the missing momentum and the thrust axis.
- $M_{\text{miss}}$ : Missing invariant mass, defined as  $\sqrt{E_{\text{miss}}^2 - P_{\text{miss}}^2}$ .
- $P_t(\pi)$ : Transverse momentum of pion.
- $\eta(\eta)$ : Pseudorapidity of the  $\eta$  meson.
- $\angle(\gamma, \gamma)_\eta$ : Angle between photons coming from  $\eta$  candidate.
- $\cos(\theta_{\text{miss}})$ : Cosine of the missing polar angle.
- $\text{PID}_e(\pi)$ : Probability of identification as an electron of the charged track.

- $PID_\mu(\pi)$ : Probability of identification as a muon of the charged track.
- $PID_K(\pi)$ : Probability of identification as a kaon of the charged track.
- $E(\gamma)$ : Energy of photons in the event.

A good selection of variables requires they are not correlated. Figure C.2 shows the correlation between the variables listed above. The observed correlation between them is low.

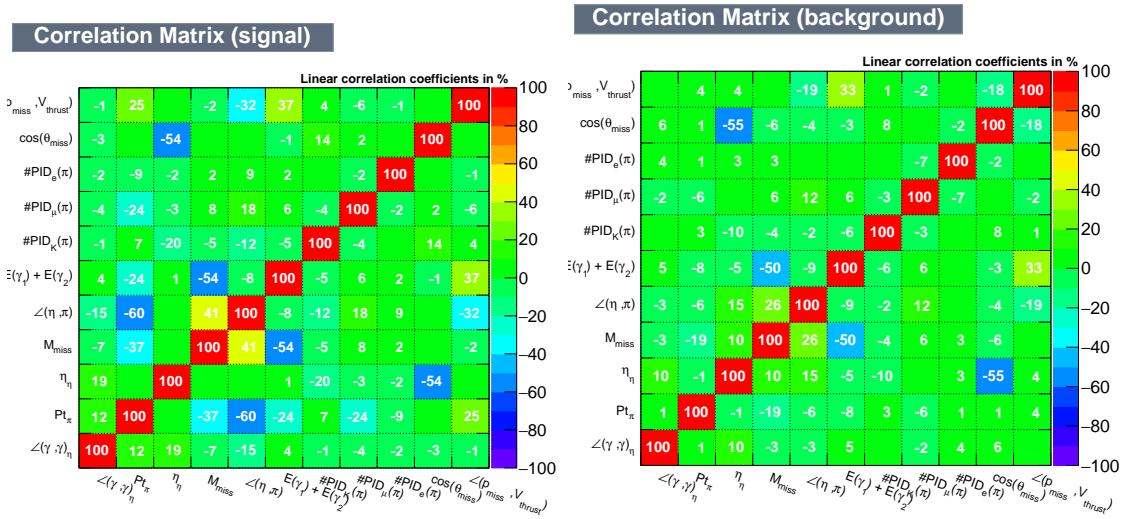


Figure C.2: Correlation between variables chosen for the 1-prong sensitivity study, evaluated in signal (left) and background (right).

For the 3-prong topology scenario, with  $\eta$  reconstructed as  $\eta \rightarrow \pi^+ \pi^- \pi^0$ , the variables used are:

- $\angle(\eta, \pi)$ : Angle between the momentum of  $\eta$  and  $\pi$  coming from the  $\tau$  lepton.
- $\angle(p_{miss}, \hat{n}_{thr})$ : The angle between the missing momentum and the thrust axis.
- $\angle(\pi, \pi^0)_\eta$ : Angle between the  $\pi$  and  $\pi^0$  momentum coming from eta.
- $\angle(\gamma, \gamma)_{\pi^0}$ : Angle between the photons coming from the  $\pi^0$ .
- $M_{miss}$ : Missing invariant mass, defined as  $\sqrt{E_{miss}^2 - P_{miss}^2}$ .

- $P_t(\pi)$ : Transverse momentum of pion coming from the  $\tau$  lepton.
- $P_t(\eta)$ : Transverse momentum of  $\eta$  meson.
- $P_t(\pi^0)$ : Transverse momentum of the  $\pi^0$  coming from the  $\eta$ .
- $\eta(\pi^0)$ : Pseudorapidity of  $\pi^0$  coming from  $\eta$ .
- $E(\gamma)$ : Energy of the photons in the event.

Figure C.2 shows the correlation between the variables listed above. Again, the correlation is low, helping to improve the BDT performance.

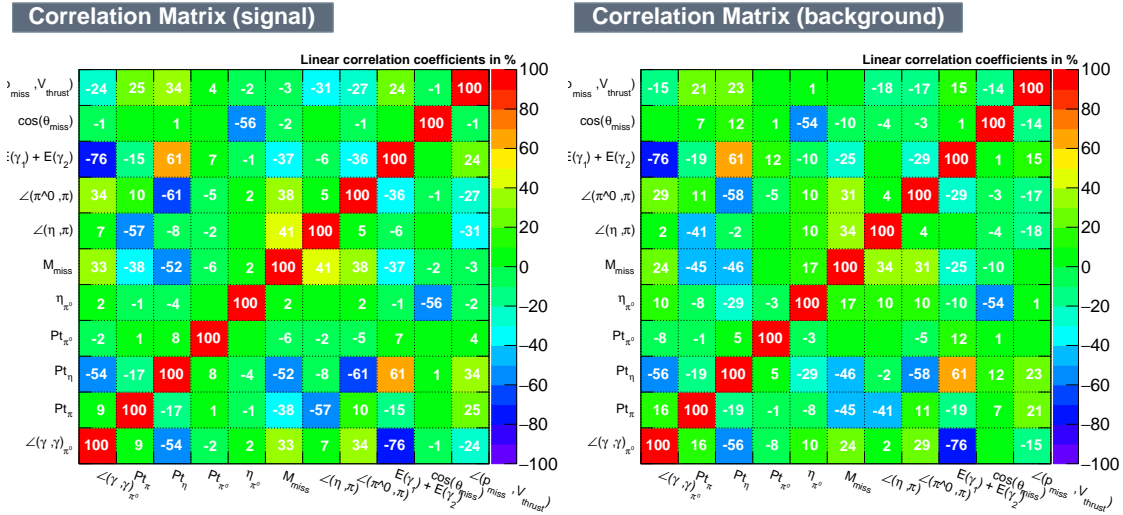


Figure C.3: Correlation between variables chosen for the 3-prong sensitivity study, evaluated in signal (left) and background (right).

The BDTs for both topologies are trained using a sample of 1M events as signal, and samples containing  $\tau$  pair,  $B\bar{B}$  and  $q\bar{q}$  decays equivalent to  $500 \text{ fb}^{-1}$  as background. Once the training stage finishes, an independent sample with the same amount of events is used to test the BDTs. Figure C.4 shows the response of the 1-prong and 3-prong trained BDTs to signal and testing samples. Kolmogorov-Smirnov tests are also performed to compare the responses, showing a good performance of both BDTs.

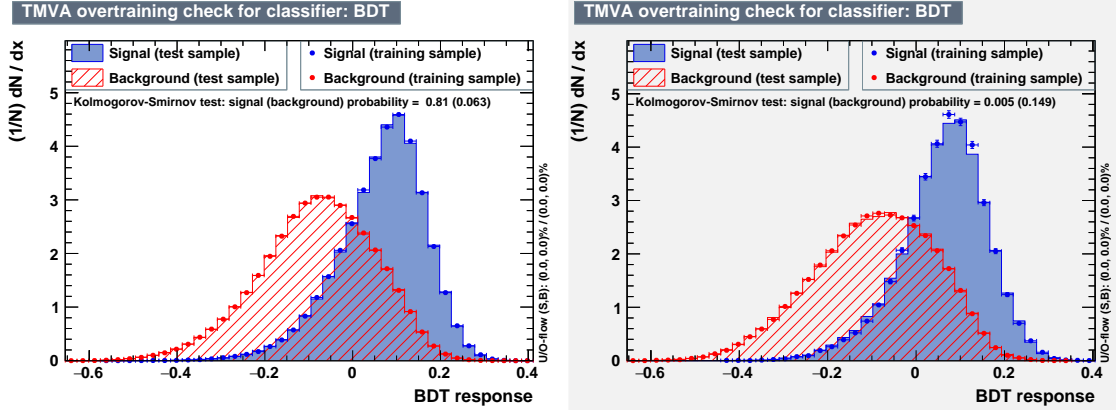


Figure C.4: Tests of over-training for 1-prong (left) and 3-prong (right) topologies. BDT response to training and testing samples are indicated with dots and solid histograms, respectively. Result of Kolmogorov-Smirnov tests are also indicated.

Several BDTs configurations were tested, using different methods implemented in TVMA. Figure C.5 shows background rejection versus signal efficiency plots using five different MVA methods. The better ratio between background rejection and signal efficiency is a BDT using an adaptive boost, AdaBoost, with 850 trees and max depth of 3 nodes. The separation type is GiniIndex and the number of cuts is 20. Details about the configuration of the BDT are described at [162].

In order to select an optimal cut in the BDTs response, the optimization proposed by G. Punzi is implemented [163]. It consists in taking a cut in the BDT response such that

$$\frac{\varepsilon}{a/2 + \sqrt{B}} \quad (\text{C.1})$$

is maximized. Figure C.6 shows the number of background events and efficiency of signal as function of the cut in the BDT response. It also shows the value of the figure of merit (C.1). The cut in the BDT response is chosen in the maximum of the figure of merit, being the optimal cuts 0.053 and 0.044 for the 1-prong and 3-prong topologies respectively. These cuts are applied in the sensitivity study described in section 7.3.

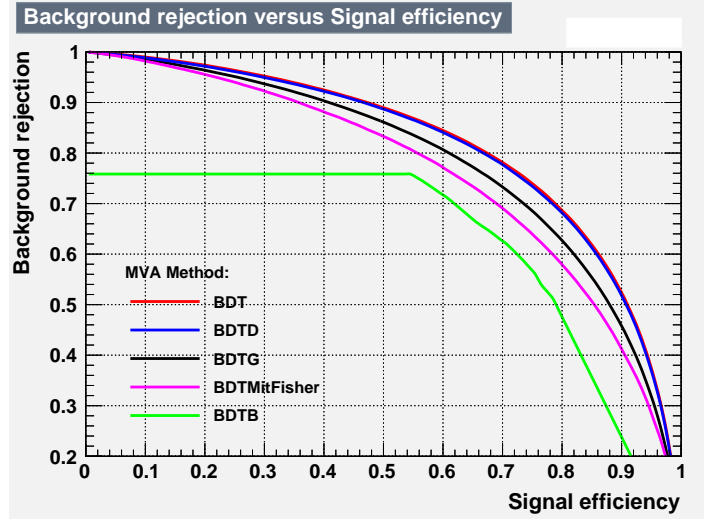


Figure C.5: Background rejection versus signal efficiency plots using different MVA methods.

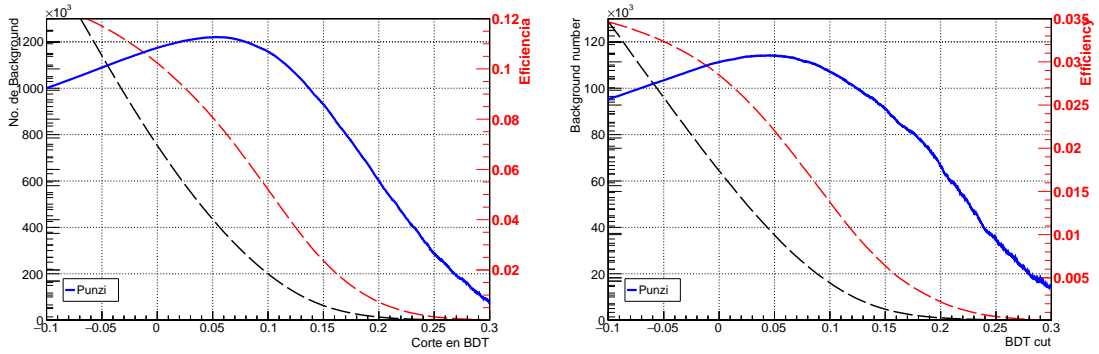


Figure C.6: Number of background events in black and efficiency of signal in red, as function of the cut in the BDT response, for the 1-prong (left) and 3-prong (right) BDTs. The value of figure of merit (C.1) is displayed in blue.

## Appendix D

---

# Publications, Conference Proceedings and Internal Notes

The following articles have been published:

- V. Abazov,..., M. Hernández Villanueva, et. al. (DØ Collaboration),  *$B_s^0$  lifetime measurement in the CP-odd decay channel  $B_s^0 \rightarrow J/\psi f_0(980)$* , **Phys. Rev. D 94 (2016) 012001**.
- E.A. Garcés, M. Hernández Villanueva, G. López Castro, P. Roig, *Effective-field theory analysis of the  $\tau^- \rightarrow \eta^{(\prime)} \pi^- \nu_\tau$  decays*, **JHEP 1712 (2017) 027**.

Communications in conferences:

- M. Hernández Villanueva et. al., *Measurement of the  $B_s^0$  lifetime in the CP-odd decay channel  $B_s^0 \rightarrow J/\psi f_0(980)$  in the D0 experiment*, 38th International Conference on High Energy Physics (ICHEP 2016), 03-10 Aug 2016. Chicago, IL, USA.  
Proceedings: **PoS ICHEP2016 (2016) 1218**.

- M. Hernández Villanueva *Sensitivity studies of  $\tau$  lepton decays with an  $\eta$  meson at the Belle II experiment*, 31th Annual Meeting of the Division of Particles and Fields of the Mexican Physical Society, 24 -26 May 2017. Mexico City, Mexico.
- M. Hernández Villanueva, *Prospects for  $\tau$  lepton physics at Belle II*, 15th International Workshop on Tau Lepton Physics (TAU 2018), 24-28 Sep 2018. Amsterdam, Netherlands.  
Proceedings: **arXiv:1812.04225**. To be published in SciPost Physics Proceedings.

Internal notes:

- E. de la Cruz-Burelo, A. de Yta-Hernández, I. Heredia de la Cruz, M. Hernández Villanueva et. al.,  *$e^+e^- \rightarrow \tau^+\tau^-$  production and the  $\tau$  lepton mass measurement at Belle II*,  
**BELLE2-NOTE-PH-2018-029**, 23 Aug 2018.
- M. Hernández Villanueva, E. de la Cruz-Burelo et. al.,  *$B_s^0$  lifetime measurement in the CP-odd decay channel  $B_s^0 \rightarrow J/\psi f_0(980)$  in the D0 experiment*,  
**DØ Analysis note 6466**, 9 Feb 2016.



---

## References

- [1] S. L. Glashow. Partial Symmetries of Weak Interactions. *Nucl. Phys.*, 22:579–588, 1961.
- [2] S. Weinberg. A Model of Leptons. *Phys. Rev. Lett.*, 19:1264–1266, 1967.
- [3] A. Salam. Weak and Electromagnetic Interactions. *Conf. Proc.*, C680519:367–377, 1968.
- [4] S. L. Glashow. The Standard Model. *Inference*, 4(1), 2018.
- [5] P. Higgs. Broken Symmetries and the Masses of Gauge Bosons. *Phys. Rev. Lett.*, 13:508–509, 1964.
- [6] F. Englert and R. Brout. Broken Symmetry and the Mass of Gauge Vector Mesons. *Phys. Rev. Lett.*, 13:321–323, 1964.
- [7] G. Aad et al. Combined search for the Standard Model Higgs boson using up to 4.9 fb<sup>-1</sup> of  $pp$  collision data at  $\sqrt{s} = 7$  TeV with the ATLAS detector at the LHC. *Phys. Lett. B*, 710:49–66, 2012.
- [8] S. Chatrchyan et al. Combined results of searches for the standard model Higgs boson in  $pp$  collisions at  $\sqrt{s} = 7$  TeV. *Phys. Lett. B*, 710:26–48, 2012.
- [9] N. Cabibbo. Unitary Symmetry and Leptonic Decays. *Phys. Rev. Lett.*, 10:531–533, 1963.

- 
- [10] M. Kobayashi and T. Maskawa. CP Violation in the Renormalizable Theory of Weak Interaction. *Prog. Theor. Phys.*, 49:652–657, 1973.
- [11] S. Bilenky and B. Pontecorvo. Lepton Mixing and Neutrino Oscillations. *Phys. Rept.*, 41:225–261, 1978.
- [12] Wikimedia Commons. Standard model of elementary particles, 2018. File: Standard Model of Elementary Particles.svg.
- [13] Z. Maki, M. Nakagawa, and S. Sakata. Remarks on the unified model of elementary particles. *Prog. Theor. Phys.*, 28:870–880, 1962.
- [14] P. F. de Salas, D. V. Forero, C. A. Ternes, M. Tortola, and J. W. F. Valle. Status of neutrino oscillations 2018:  $3\sigma$  hint for normal mass ordering and improved CP sensitivity. *Phys. Lett. B*, 782:633–640, 2018.
- [15] P. A. R. Ade et al. Planck 2015 results. XIII. Cosmological parameters. *Astron. Astrophys.*, 594:A13, 2016.
- [16] A. D. Sakharov. Violation of CP Invariance, C asymmetry, and baryon asymmetry of the universe. *Pisma Zh. Eksp. Teor. Fiz.*, 5:32–35, 1967.
- [17] P. Huet. Electroweak baryogenesis and the standard model. In *Phenomenology of Unification from Present to Future: Proceedings of the 1st International Conference, March 23-26, 1994, Rome*, pages 77–91, 1994.
- [18] S. Bifani, S. Descotes-Genon, A. Romero Vidal, and M. Schune. Review of Lepton Universality tests in  $B$  decays. *arXiv preprint arXiv:1809.06229[hep-ex]*, 2018.
- [19] J. P. Lees et al. Measurement of an Excess of  $\bar{B} \rightarrow D^{(*)} \tau^- \bar{\nu}_\tau$  Decays and Implications for Charged Higgs Bosons. *Phys. Rev. D*, 88:072012, 2013.
- [20] S. Hirose et al. Measurement of the  $\tau$  lepton polarization and  $R(D^*)$  in the decay  $\bar{B} \rightarrow D^* \tau^- \bar{\nu}_\tau$ . *Phys. Rev. Lett.*, 118(21):211801, 2017.

- 
- [21] G. W. Bennett et al. Final Report of the Muon E821 Anomalous Magnetic Moment Measurement at BNL. *Phys. Rev. D*, 73:072003, 2006.
- [22] H. Cheng and I. Low. TeV symmetry and the little hierarchy problem. *JHEP*, 09:051, 2003.
- [23] G.C. Branco, P. M. Ferreira, L. Lavoura, et al. Theory and phenomenology of two-higgs-doublet models. *Physics Reports*, 516(1):1 – 102, 2012.
- [24] E. Hanson, W. Klemm, et al. Charged Higgs Bosons in Naturally Aligned Two Higgs Doublet Models at the LHC. *arXiv preprint arXiv:1812.04713[hep-ph]*, 2018.
- [25] J. C. Pati and A. Salam. Unified lepton-hadron symmetry and a gauge theory of the basic interactions. *Phys. Rev. D*, 8:1240–1251, 1973.
- [26] J. C. Pati and A. Salam. Lepton number as the fourth "color". *Phys. Rev. D*, 10:275–289, 1974.
- [27] N. Assad, B. Fornal, and B. Grinstein. Baryon Number and Lepton Universality Violation in Leptoquark and Diquark Models. *Phys. Lett. B*, 777:324–331, 2018.
- [28] L. Di Luzio, A. Greljo, and M. Nardecchia. Gauge leptoquark as the origin of  $B$ -physics anomalies. *Phys. Rev. D*, 96(11):115011, 2017.
- [29] L. Calibbi, A. Crivellin, and T. Li. Model of vector leptoquarks in view of the  $B$ -physics anomalies. *Phys. Rev. D*, 98(11):115002, 2018.
- [30] L. J. Hall and L. Randall. CP Violation From Scalar Leptoquarks. *Nucl. Phys. B*, 274:157–170, 1986.
- [31] I. Doršner, S. Fajfer, A. Greljo, J. F. Kamenik, and N. Košnik. Physics of leptoquarks in precision experiments and at particle colliders. *Phys. Rept.*, 641:1–68, 2016.

- 
- [32] G. C. Branco, L. Lavoura, and J. P. Silva. CP Violation. *Int. Ser. Monogr. Phys.*, 103:1–536, 1999.
  - [33] E. Kou, P. Urquijo, et al. The Belle II Physics book. *arXiv preprint arXiv:1808.10567 [hep-ex]*, 2018. To be published in PTEP.
  - [34] M. Hernández Villanueva. Prospects for  $\tau$  lepton physics at Belle II. *arXiv preprint arXiv:1812.04225[hep-ex]*.
  - [35] M. Tanabashi et al. Review of Particle Physics. *Phys. Rev. D*, 98(3):030001, 2018.
  - [36] Y. Tsai. Decay Correlations of Heavy Leptons in  $e^+ e^- \rightarrow \text{Lepton}^+ \text{Lepton}^-$ . *Phys. Rev. D*, 4:2821, 1971. [Erratum: *Phys. Rev. D* 13,771(1976)].
  - [37] S. Descotes-Genon and B. Moussallam. Analyticity of  $\eta\pi$  isospin-violating form factors and the  $\tau \rightarrow \eta\pi\nu$  second-class decay. *Eur. Phys. J.*, C74:2946, 2014.
  - [38] E. A. Garcés, M. Hernández Villanueva, G. López Castro, and P. Roig. Effective-field theory analysis of the  $\tau^- \rightarrow \eta^{(\prime)}\pi^- \nu_\tau$  decays. *JHEP*, 12:027, 2017.
  - [39] G. López Castro. Non-standard interactions in  $\tau^- \rightarrow (\pi^-\eta, \pi^-\pi^0)\nu_\tau$  decays.
  - [40] H. R. Quinn. Heavy flavor physics. In *2002 European School of high-energy physics, Pylos, Greece, 25 Aug-7 Sep 2002: Proceedings*, pages 35–64, 2002.
  - [41] A. J. Bevan et al. The Physics of the B Factories. *Eur. Phys. J.*, C74:3026, 2014.
  - [42] A. Lenz.  $B_s - \bar{B}_s$  mixing and lifetimes. *PoS, Beauty* 2014:002, 2014.
  - [43] C. Bobeth and U. Haisch. New Physics in  $\Gamma_{12}^s$ :  $(\bar{s}b)(\bar{\tau}\tau)$  Operators. *Acta Phys. Polon. B*, 44:127–176, 2013.
  - [44] V. M. Abazov et al. Measurement of the  $B_s^0$  lifetime in the exclusive decay channel  $B_s^0 \rightarrow J/\psi\phi$ . *Phys. Rev. Lett.*, 94:042001, 2005.

- 
- [45] S. Stone and L. Zhang. S-waves and the measurement of  $cp$  violating phases in  $B_s$  decays. *Phys. Rev. D*, 79:074024, Apr 2009.
- [46] R. Aaij et al. First observation of  $B_s^0 \rightarrow J/\psi f_0(980)$  decays. *Phys. Lett. B*, 698:115–122, 2011.
- [47] J. Li et al. Observation of  $B_s^0 \rightarrow J/\psi f_0(980)$  and Evidence for  $B_s^0 \rightarrow J/\psi f_0(1370)$ . *Phys. Rev. Lett.*, 106:121802, 2011.
- [48] T. Aaltonen et al. Measurement of branching ratio and  $B_s^0$  lifetime in the decay  $B_s^0 \rightarrow J/\psi f_0(980)$  at CDF. *Phys. Rev. D*, 84:052012, 2011.
- [49] V. M. Abazov et al. Measurement of the relative branching ratio of  $B_s^0 \rightarrow J/\psi f_0(980)$  to  $B_s^0 \rightarrow J/\psi \phi$ . *Phys. Rev. D*, 85:011103, 2012.
- [50] R. Aaij et al. Measurement of the  $B_s$  effective lifetime in the  $J/\psi f_0(980)$  final state. *Phys. Rev. Lett.*, 109:152002, 2012.
- [51] A. M Sirunyan et al. Measurement of b hadron lifetimes in pp collisions at  $\sqrt{s} = 8$  TeV. *Eur. Phys. J. C*, 78(6):457, 2018. [Erratum: *Eur. Phys. J. C* 78, no.7, 561(2018)].
- [52] V. M. Abazov et al. The Upgraded D0 detector. *Nucl. Instrum. Meth. A*, 565:463–537, 2006.
- [53] K. S. Cranmer. Kernel estimation in high-energy physics. *Comput. Phys. Commun.*, 136:198–207, 2001.
- [54] S. M. Flatte. Coupled - Channel Analysis of the pi eta and K anti-K Systems Near K anti-K Threshold. *Phys. Lett.*, 63B:224–227, 1976.
- [55] V. Abazov et al.  $B_s^0$  lifetime measurement in the CP-odd decay channel  $B_s^0 \rightarrow J/\psi f_0(980)$ . *Phys. Rev. D*, 94(1):012001, 2016.

- [56] M. L. Perl et al. Evidence for anomalous lepton production in  $e^+e^-$  annihilation. *Phys. Rev. Lett.*, 35:1489–1492, 1975.
- [57] M. L. Perl et al. Properties of Anomalous e mu Events Produced in  $e^+e^-$  Annihilation. *Phys. Lett.*, 63B:466, 1976.
- [58] M. L. Perl et al. Properties of the proposed  $\tau$  charged lepton. *Physics Letters B*, 70(4):487–490, 1977.
- [59] W. Bacino et al. Measurement of the Threshold Behavior of  $\tau^+\tau^-$  Production in  $e^+e^-$  Annihilation. *Phys. Rev. Lett.*, 41:13, 1978.
- [60] M. Ablikim et al. Precision measurement of the mass of the  $\tau$  lepton. *Phys. Rev. D*, 90(1):012001, 2014.
- [61] H. Albrecht et al. A Measurement of the tau mass. *Phys. Lett. B*, 292:221–228, 1992.
- [62] K. Abe et al. Measurement of the mass of the tau-lepton and an upper limit on the mass difference between  $\tau^+$  and  $\tau^-$ . *Phys. Rev. Lett.*, 99:011801, 2007.
- [63] B. Aubert et al. Measurements of the tau mass and the mass difference of the  $\tau^+$  and  $\tau^-$  at BaBar. *Phys. Rev. D*, 80:092005, 2009.
- [64] M. Tanabashi et al. Review of particle physics. *Phys. Rev. D*, 98:030001, Aug 2018.
- [65] J. Jaros. Measurement of the  $\tau$  Lifetime. *J. Phys. Colloq.*, 43(C3):106–109, 1982.
- [66] K. Belous et al. Measurement of the  $\tau$ -lepton lifetime at Belle. *Phys. Rev. Lett.*, 112(3):031801, 2014.
- [67] Y. Amhis et al. Averages of  $b$ -hadron,  $c$ -hadron, and  $\tau$ -lepton properties as of summer 2014. *arXiv preprint arXiv:1412.7515*, 2014.
- [68] B. Aubert et al. Search for the decay  $\tau^- \rightarrow 4\pi^- 3\pi^+(\pi^0)\nu_\tau$ . *Phys. Rev. D*, 72:012003, 2005.

- 
- [69] A. Sirlin. Radiative corrections in the  $SU(2)_L \times U(1)$  theory: A simple renormalization framework. *Phys. Rev. D*, 22:971–981, Aug 1980.
- [70] M. Fael, L. Mercolli, and M. Passera.  $W$ -propagator corrections to  $\mu$  and  $\tau$  leptonic decays. *Phys. Rev. D*, 88:093011, 2013.
- [71] T. Kinoshita and A. Sirlin. Radiative corrections to fermi interactions. *Phys. Rev.*, 113:1652–1660, Mar 1959.
- [72] W. J. Marciano and A. Sirlin. Electroweak radiative corrections to  $\tau$  decay. *Phys. Rev. Lett.*, 61:1815–1818, Oct 1988.
- [73] J. H. Kuhn and E. Mirkes. Structure functions in tau decays. *Z. Phys. C*, 56:661–672, 1992. [Erratum: *Z. Phys.C* 67,364(1995)].
- [74] A. Pich. Precision Tau Physics. *Prog. Part. Nucl. Phys.*, 75:41–85, 2014.
- [75] M. Fujikawa et al. High-statistics study of the  $\tau^- \rightarrow \pi^- \pi^0 \nu_\tau$  decay. *Phys. Rev. D*, 78:072006, 2008.
- [76] K. Ackerstaff et al. A Measurement of the hadronic decay current and the tau-neutrino helicity in  $\tau^- \rightarrow \pi^- \pi^+ \pi^- \nu_\tau$ . *Z. Phys.*, C75:593–605, 1997.
- [77] P. Abreu et al. A Study of the hadronic resonance structure in the decay  $\tau \rightarrow 3 \pi \nu_\tau$ . *Phys. Lett. B*, 426:411–427, 1998.
- [78] E. Gámiz, M. Jamin, A. Pich, J. Prades, and F. Schwab.  $V_{us}$  and  $m_s$  from hadronic  $\tau$  decays. *Phys. Rev. Lett.*, 94:011803, 2005.
- [79] E. Gamiz, M. Jamin, A. Pich, J. Prades, and F. Schwab. Theoretical progress on the  $V_{us}$  determination from tau decays. *PoS, KAON:008*, 2008.
- [80] K. Maltman. A Critical look at  $V_{us}$  determinations from hadronic  $\tau$  decay data. *Nucl. Phys. Proc. Suppl.*, 218:146–151, 2011.

- 
- [81] Y. Amhis et al. Averages of  $b$ -hadron,  $c$ -hadron, and  $\tau$ -lepton properties as of summer 2016. *Eur. Phys. J.*, C77(12):895, 2017.
- [82] C. Patrignani et al. Review of Particle Physics. *Chin. Phys. C*, 40(10):100001, 2016.
- [83] A. Pich. Tau-decay determination of the strong coupling. *arXiv preprint arXiv:1811.10067[hep-ex]*.
- [84] P. M. Lewis et al. First Measurements of Beam Backgrounds at SuperKEKB. *Nucl. Instrum. Meth. A*, 914:69–144, 2019.
- [85] T. Abe et al. Belle II technical design report. *arXiv preprint arXiv:1011.0352*, 2010.
- [86] P Fischer et al. Progress towards a large area, thin DEPFET detector module. *Nucl. Instrum. Meth. A*, 582(3):843–848, 2007.
- [87] M. Starič, K. Inami, P. Križan, and T. Iijima. Likelihood analysis of patterns in a time-of-propagation (TOP) counter. *Nucl. Instrum. Meth. A*, 595(1):252–255, 2008.
- [88] T. Iijima, S. Korpar, , et al. A novel type of proximity focusing RICH counter with multiple refractive index aerogel radiator. *Nucl. Instrum. Meth. A*, 548(3):383–390, 2005.
- [89] T. Kuhr, C. Pulvermacher, M. Ritter, T. Hauth, and N. Braun. The Belle II core software. *arXiv preprint arXiv:1809.04299*, 2018.
- [90] D. J. Lange. The EvtGen particle decay simulation package. *Nucl. Instrum. Meth. A*, 462(1):152–155, 2001.
- [91] T. Sjöstrand et al. An Introduction to PYTHIA 8.2. *Comput. Phys. Commun.*, 191:159–177, 2015.
- [92] S. Jadach, B. F. L. Ward, and Z. Was. The Precision Monte Carlo event generator K K for two fermion final states in  $e^+ e^-$  collisions. *Comput. Phys. Commun.*, 130:260–325, 2000.



- 
- [93] S. Jadach, J. H. Kuhn, and Z. Was. TAUOLA: A Library of Monte Carlo programs to simulate decays of polarized tau leptons. *Comput. Phys. Commun.*, 64:275–299, 1990.
- [94] C. M. Carloni Calame, G. Montagna, O. Nicrosini, and F. Piccinini. The BABAYAGA event generator. *Nucl. Phys. Proc. Suppl.*, 131:48–55, 2004.
- [95] S. Actis et al. Quest for precision in hadronic cross sections at low energy: Monte Carlo tools vs. experimental data. *Eur. Phys. J.*, C66:585–686, 2010.
- [96] S Agostinelli, John Allison, K al Amako, J Apostolakis, H Araujo, P Arce, M Asai, D Axen, S Banerjee, G Barrand, et al. GEANT4 — a simulation toolkit. *Nucl. Instrum. Meth. A*, 506(3):250–303, 2003.
- [97] H. Albrecht et al. A Measurement of the tau mass. *Phys. Lett. B*, 292:221–228, 1992.
- [98] A. Lusiani. Status and progress of the HFLAV-Tau group activities. *arXiv preprint arXiv:1804.08436*, 2018.
- [99] S. T. Petcov. The Processes  $\mu \rightarrow e\gamma$ ,  $\mu \rightarrow ee\bar{e}$ ,  $\nu' \rightarrow \nu\gamma$  in the Weinberg-Salam Model with Neutrino Mixing. *Sov. J. Nucl. Phys.*, 25:340, 1977. [Erratum: *Yad. Fiz.*25,1336(1977)].
- [100] G. Hernández-Tomé, G. López Castro, and P. Roig. Flavor violating leptonic decays of  $\tau$  and  $\mu$  leptons in the Standard Model with massive neutrinos. *arXiv preprint arXiv:1807.06050*, 2018.
- [101] A. Celis, V. Cirigliano, and E. Passemar. Model-discriminating power of lepton flavor violating  $\tau$  decays. *Phys. Rev. D*, 89:095014, May 2014.
- [102] J. Hisano. Lepton flavor violating decay of tau lepton in the supersymmetric seesaw model. In *Higher luminosity B factories. Proceedings, 3rd Workshop, Shonan Village, Japan, August 6-7*, pages 166–174, 2002.

- 
- [103] E. Arganda and M. J. Herrero. Testing supersymmetry with lepton flavor violating tau and mu decays. *Phys. Rev. D*, 73:055003, 2006.
  - [104] Y. Grossman and Y. Nir. CP violation in  $\tau \rightarrow \nu\pi K_S$  and  $D \rightarrow \pi K_S$ : The importance of  $K_S - K_L$  interference. *JHEP*, 04:002, 2012.
  - [105] I. I. Bigi and A. I. Sanda. A 'Known' CP asymmetry in tau decays. *Phys. Lett. B*, 625:47–52, 2005.
  - [106] J. P. Lees et al. Search for CP Violation in the Decay  $\tau^- \rightarrow \pi^- K_S^0 (>= 0\pi^0)\nu_\tau$ . *Phys. Rev. D*, 85:031102, 2012. [Erratum: *Phys. Rev. D* 85,099904(2012)].
  - [107] V. Cirigliano, A. Crivellin, and M. Hoferichter. No-go theorem for nonstandard explanations of the  $\tau \rightarrow K_S \pi \nu_\tau$  CP asymmetry. *Phys. Rev. Lett.*, 120(14):141803, 2018.
  - [108] M. Bischofberger, H. Hayashii, et al. Search for CP violation in  $\tau^\pm \rightarrow K_S^0 \pi^\pm \nu_\tau$  decays at Belle. *Phys. Rev. Lett.*, 107:131801, 2011.
  - [109] A. Rouge. Tau lepton Michel parameters and new physics. *Eur. Phys. J.*, C18:491–496, 2001.
  - [110] L. Michel. Interaction between four half spin particles and the decay of the  $\mu$  meson. *Proc. Phys. Soc. A*, 63:514–531, 1950.
  - [111] D. A. Epifanov. Measurement of Michel parameters in leptonic  $\tau$  decays at Belle. *Nucl. Part. Phys. Proc.*, 287-288:7–10, 2017.
  - [112] N. Shimizu et al. Measurement of the tau Michel parameters  $\bar{\eta}$  and  $\xi_K$  in the radiative leptonic decay  $\tau^- \rightarrow \ell^- \nu_\tau \bar{\nu}_\ell \gamma$ . *PTEP*, 2018(2):023C01, 2018.
  - [113] D. Gómez Dumm and P. Roig. Resonance Chiral Lagrangian analysis of  $\tau^- \rightarrow \eta^{(\prime)} \pi^- \pi^0 \nu_\tau$  decays. *Phys. Rev. D*, 86:076009, 2012.

- 
- [114] M. Artuso et al. Measurement of tau decays involving eta mesons. *Phys. Rev. Lett.*, 69:3278–3281, 1992.
- [115] D. Buskulic et al. A Study of tau decays involving eta and omega mesons. *Z. Phys.*, C74:263–273, 1997.
- [116] K. Inami et al. Precise measurement of hadronic tau-decays with an eta meson. *Phys. Lett. B*, 672:209–218, 2009.
- [117] S Gershtein and Y. Zeldovich. *Sov. Phys. JETP*, 2:576, 1956.
- [118] R. P. Feynman and M. Gell-Mann. Theory of Fermi interaction. *Phys. Rev.*, 109:193–198, 1958.
- [119] Y. Tsai. Decay correlations of heavy leptons in  $e^+ + e^- \rightarrow l^+ + l^-$ . *Phys. Rev. D*, 4:2821–2837, 1971.
- [120] V. A. Cherepanov and S. I. Eidelman. tau lepton decays and CVC. In *Tau 2008, proceedings of the 10th International Workshop on Tau Lepton Physics, Novosibirsk, Russia, 22-25 September 2008*, 2009.
- [121] R. Alemany, M. Davier, and A. Hocker. Improved determination of the hadronic contribution to the muon (g-2) and to alpha (M(Z)) using new data from hadronic tau decays. *Eur. Phys. J.*, C2:123–135, 1998.
- [122] M. Davier, S. Eidelman, Andreas Hocker, and Z. Zhang. Confronting spectral functions from  $e^+ e^-$  annihilation and tau decays: Consequences for the muon magnetic moment. *Eur. Phys. J.*, C27:497–521, 2003.
- [123] M. Davier, A. Hoecker, G. López Castro, B. Malaescu, X. H. Mo, G. Toledo Sánchez, P. Wang, C. Z. Yuan, and Z. Zhang. The Discrepancy Between tau and  $e^+e^-$  Spectral Functions Revisited and the Consequences for the Muon Magnetic Anomaly. *Eur. Phys. J.*, C66:127–136, 2010.

- 
- [124] R. R. Akhmetshin et al. Study of the process  $e^+e^- \rightarrow \pi^+\pi^-\pi^+\pi^-\pi^0$  with CMD-2 detector. *Phys. Lett. B*, 489:125–130, 2000.
- [125] V. M. Aulchenko et al. Measurement of the  $e^+e^- \rightarrow \eta\pi^+\pi^-$  cross section in the center-of-mass energy range 1.22-2.00 GeV with the SND detector at the VEPP-2000 collider. *Phys. Rev.*, D91(5):052013, 2015.
- [126] B. Aubert et al. The  $e^+e^- \rightarrow 2(\pi^+\pi^-)\pi^0$ ,  $2(\pi^+\pi^-)\eta$ ,  $K^+K^-\pi^+\pi^-\pi^0$  and  $K^+K^-\pi^+\pi^-\eta$  Cross Sections Measured with Initial-State Radiation. *Phys. Rev. D*, 76:092005, 2007. [Erratum: *Phys. Rev. D* 77,119902(2008)].
- [127] J. P. Lees et al. Study of the process  $e^+e^- \rightarrow \pi^+\pi^-\eta$  using initial state radiation. *Phys. Rev. D*, 97:052007, 2018.
- [128] J. E. Gaiser. *Charmonium Spectroscopy From Radiative Decays of the  $J/\psi$  and  $\psi'$* . PhD thesis, SLAC, 1982.
- [129] G. J. Feldman and R. D. Cousins. A Unified approach to the classical statistical analysis of small signals. *Phys. Rev. D*, 57:3873–3889, 1998.
- [130] T. D. Lee and C. Yang. Charge Conjugation, a New Quantum Number  $G$ , and Selection Rules Concerning a Nucleon Anti-nucleon System. *Nuovo Cim.*, 10:749–753, 1956. [,233(1956)].
- [131] S. Weinberg. Charge symmetry of weak interactions. *Physical Review*, 112(4):1375, 1958.
- [132] N. Severijns, M. Beck, and O. Naviliat-Cuncic. Tests of the standard electroweak model in beta decay. *Rev. Mod. Phys.*, 78:991–1040, 2006.
- [133] S. Triambak et al.  $2_1^+ \rightarrow 3_1^+$  gamma width in  $^{22}\text{Na}$  and second class currents. *Phys. Rev.*, C95(3):035501, 2017. [Addendum: *Phys. Rev. C* 95, no.4, 049901(2017)].

- 
- [134] C. Leroy and J. Pestieau.  $\tau$ -decay and second-class currents. *Physics Letters B*, 72(3):398–399, 1978.
  - [135] A. Pich. ‘Anomalous’  $\eta$  Production in Tau Decay. *Phys. Lett. B*, 196:561–565, 1987.
  - [136] S. Nussinov and A. Soffer. Estimate of the branching fraction  $\tau \rightarrow \eta \pi^- \nu_\tau$ , the  $a_0(980)$ , and non-standard weak interactions. *Phys. Rev. D*, 78:033006, 2008.
  - [137] N. Paver and Riazuddin. On meson dominance in the ‘second class’  $\tau \rightarrow \eta \pi \nu_\tau$  decay. *Phys. Rev. D*, 82:057301, 2010.
  - [138] M. K. Volkov and D. G. Kostunin. The decays  $\rho^- \rightarrow \eta \pi^-$  and  $\tau^- \rightarrow \eta(\eta') \pi^- \nu$  in the NJL model. *Phys. Rev. D*, 86:013005, 2012.
  - [139] R. Escribano, S. González-Solís, and P. Roig. Predictions on the second-class current decays  $\tau^- \rightarrow \pi^- \eta^{(\prime)} \nu_\tau$ . *Phys. Rev. D*, 94(3):034008, 2016.
  - [140] P. del Amo Sánchez et al. Studies of  $\tau \rightarrow \eta K \nu_\tau$  and  $\tau \rightarrow \eta \pi \nu_\tau$  at BaBar and a search for a second-class current. *Phys. Rev. D*, 83:032002, 2011.
  - [141] K. Hayasaka. Second class current in  $\tau \rightarrow \pi \eta \nu$  analysis and measurement of  $\tau \rightarrow hh'h'' \nu_\tau$  from Belle: electroweak physics from Belle. *PoS, EPS-HEP 2009*:374, 2009.
  - [142] J. E. Bartelt et al. First observation of the decay  $\tau^- \rightarrow K^- \eta \nu_\tau$ . *Phys. Rev. Lett.*, 76:4119–4123, 1996.
  - [143] M. Jung, A. Pich, and P. Tuzon. Charged-Higgs phenomenology in the Aligned two-Higgs-doublet model. *JHEP*, 11:003, 2010.
  - [144] D. Bečirević, S. Fajfer, N. Košnik, and O. Sumensari. Leptoquark model to explain the  $B$ -physics anomalies,  $R_K$  and  $R_D$ . *Phys. Rev. D*, 94(11):115021, 2016.
  - [145] T. Bhattacharya, V. Cirigliano, et al. Probing Novel Scalar and Tensor Interactions from (Ultra)Cold Neutrons to the LHC. *Phys. Rev. D*, 85:054512, 2012.

- [146] V. Cirigliano, J. Jenkins, and M. Gonzalez-Alonso. Semileptonic decays of light quarks beyond the Standard Model. *Nucl. Phys. B*, 830:95–115, 2010.
- [147] D. Gómez Dumm and P. Roig. Dispersive representation of the pion vector form factor in  $\tau \rightarrow \pi\pi\nu_\tau$  decays. *Eur. Phys. J.*, C73(8):2528, 2013.
- [148] L. Beldjoudi and T. N. Truong.  $\tau \rightarrow \pi K$  neutrino decay and  $\pi K$  scattering. *Phys. Lett. B*, 351:357–368, 1995.
- [149] M. Gonzalez-Alonso, O. Naviliat-Cuncic, and N. Severijns. New physics searches in nuclear and neutron  $\beta$  decay. *Prog. Part. Nucl. Phys.*, 104:165–223, 2019.
- [150] S. Di Carlo, P. Bambade, et al. Early Phase 2 Results of LumiBelle2 for the SuperKEKB Electron Ring. *Proceedings, 9th International Particle Accelerator Conference (IPAC 2018): Vancouver, BC Canada*, 2018. [*J. Phys. Conf. Ser.* 1067(7):072025, 2018].
- [151] A. Guevara, G. López-Castro, and P. Roig.  $\tau^- \rightarrow \eta^{(\prime)}\pi^-\nu_\tau\gamma$  decays as backgrounds in the search for second class currents. *Phys. Rev. D*, 95(5):054015, 2017.
- [152] G. Hernández-Tomé, G. López Castro, and P. Roig. G-parity breaking in  $\tau^- \rightarrow \eta^{(\prime)}\pi^-\nu_\tau$  decays induced by the  $\eta^{(\prime)}\gamma\gamma$  form factor. *Phys. Rev. D*, 96(5):053003, 2017.
- [153] I. M. Nugent, T. Przedziński, P. Roig, O. Shekhovtsova, and Z. Wąs. Resonance chiral lagrangian currents and experimental data for  $\tau^- \rightarrow \pi^-\pi^-\pi^+\nu_\tau$ . *Phys. Rev. D*, 88:093012, 2013.
- [154] D. Gómez Dumm, P. Roig, A. Pich, and J. Portolés.  $\tau \rightarrow \pi\pi\pi\nu_\tau$  decays and the  $a_1(1260)$  off-shell width revisited. *Physics Letters B*, 685(2):158 – 164, 2010.
- [155] O. Shekhovtsova, T. Przedziński, P. Roig, and Z. Wąs. Resonance chiral lagrangian currents and  $\tau$  decay monte carlo. *Phys. Rev. D*, 86:113008, Dec 2012.

- 
- [156] G. Ecker and R. Unterdorfer. Four pion production in  $e^+e^-$  annihilation. *Eur. Phys. J.*, C24:535–545, 2002.
- [157] H. Czyz, J. H. Kuhn, and A. Wapienik. Four-pion production in tau decays and  $e^+e^-$  annihilation: An Update. *Phys. Rev. D*, 77:114005, 2008.
- [158] V. M. Abazov, , et al. Measurement of the  $\Lambda_b^0$  Lifetime in the Decay  $\Lambda_b^0 \rightarrow J/\psi \Lambda^0$  with the D0 Detector. *Phys. Rev. Lett.*, 94(10):102001, 2005.
- [159] T. Sjostrand, S. Mrenna, and P. Z. Skands. PYTHIA 6.4 Physics and Manual. *JHEP*, 05:026, 2006.
- [160] Y. Coadou. Boosted decision trees and applications. In *EPJ Web of conferences*, volume 55, page 02004. EDP Sciences, 2013.
- [161] R. Brun and F. Rademakers. ROOT: An object oriented data analysis framework. *Nucl. Instrum. Meth.*, A389:81–86, 1997.
- [162] P. Speckmayer, A. Hocker, J. Stelzer, and H. Voss. The toolkit for multivariate data analysis, TMVA 4. *J. Phys. Conf. Ser.*, 219:032057, 2010.
- [163] G. Punzi. Sensitivity of searches for new signals and its optimization. *Statistical problems in particle physics, astrophysics and cosmology. Proceedings, Conference, PHYSTAT 2003, Stanford, USA, September 8-11, 2003*, C030908:MODT002, 2003.